

1976

Study of radio frequency excited argon plasma in a cathodic sputtering system

Charlie Louis Tolliver
Iowa State University

Follow this and additional works at: <https://lib.dr.iastate.edu/rtd>

 Part of the [Electrical and Electronics Commons](#), and the [Oil, Gas, and Energy Commons](#)

Recommended Citation

Tolliver, Charlie Louis, "Study of radio frequency excited argon plasma in a cathodic sputtering system " (1976). *Retrospective Theses and Dissertations*. 5807.
<https://lib.dr.iastate.edu/rtd/5807>

This Dissertation is brought to you for free and open access by the Iowa State University Capstones, Theses and Dissertations at Iowa State University Digital Repository. It has been accepted for inclusion in Retrospective Theses and Dissertations by an authorized administrator of Iowa State University Digital Repository. For more information, please contact digirep@iastate.edu.

INFORMATION TO USERS

This material was produced from a microfilm copy of the original document. While the most advanced technological means to photograph and reproduce this document have been used, the quality is heavily dependent upon the quality of the original submitted.

The following explanation of techniques is provided to help you understand markings or patterns which may appear on this reproduction.

1. The sign or "target" for pages apparently lacking from the document photographed is "Missing Page(s)". If it was possible to obtain the missing page(s) or section, they are spliced into the film along with adjacent pages. This may have necessitated cutting thru an image and duplicating adjacent pages to insure you complete continuity.
2. When an image on the film is obliterated with a large round black mark, it is an indication that the photographer suspected that the copy may have moved during exposure and thus cause a blurred image. You will find a good image of the page in the adjacent frame.
3. When a map, drawing or chart, etc., was part of the material being photographed the photographer followed a definite method in "sectioning" the material. It is customary to begin photoing at the upper left hand corner of a large sheet and to continue photoing from left to right in equal sections with a small overlap. If necessary, sectioning is continued again — beginning below the first row and continuing on until complete.
4. The majority of users indicate that the textual content is of greatest value, however, a somewhat higher quality reproduction could be made from "photographs" if essential to the understanding of the dissertation. Silver prints of "photographs" may be ordered at additional charge by writing the Order Department, giving the catalog number, title, author and specific pages you wish reproduced.
5. PLEASE NOTE: Some pages may have indistinct print. Filmed as received.

University Microfilms International

300 North Zeeb Road
Ann Arbor, Michigan 48106 USA
St. John's Road, Tyler's Green
High Wycombe, Bucks, England HP10 9HR

77-10,344

TOLLIVER, Charlie Louis, 1935-
STUDY OF RADIO FREQUENCY EXCITED
ARGON PLASMA IN A CATHODIC SPUTTERING
SYSTEM.

Iowa State University, Ph.D., 1976
Engineering, electronics and electrical

Xerox University Microfilms, Ann Arbor, Michigan 48106

**Study of radio frequency excited argon plasma
in a cathodic sputtering system**

by

Charlie Louis Tolliver

**A Dissertation Submitted to the
Graduate Faculty in Partial Fulfillment of
The Requirements for the Degree of
DOCTOR OF PHILOSOPHY**

Major: Electrical Engineering

Approved:

Signature was redacted for privacy.

In Charge of Major Work

Signature was redacted for privacy.

For the Major Department

Signature was redacted for privacy.

For the Graduate College

**Iowa State University
Ames, Iowa**

1976

TABLE OF CONTENTS

	Page
I. INTRODUCTION	1
A. Historical Background on Gaseous Plasma Research	2
B. Cathodic Sputtering System	6
C. Statement of the Problem	14
II. EXPERIMENTAL MEASUREMENTS AND OBSERVATIONS	17
A. Description of the Sputtering Equipment	17
1. Argon plasma production by rf current loop	20
2. Helmholtz coils	20
3. Center-rod cathode and the grounded anode	22
B. Plasma Diagnostics and the Langmuir Probe	22
1. Theory of the Langmuir probe	24
a. Static probe theory	24
b. Ion current data	26
2. Design and construction of the Langmuir probe	28
3. Instrumentation for measurement of current voltage characteristics of the Langmuir probe	32
4. Illustrations of I-V characteristics obtained	38
5. Information derived from experimental measurements	73
C. Measurement of rf Power Supplied to the Sputtering System	78
D. Some Remarks on the Measurement Techniques and Sources of Error	81

	Page
III. THEORETICAL ANALYSIS	85
A. Basic Equations Governing the Interaction of Electromagnetic Fields with Plasma	85
B. Basic Assumptions Made in the Analysis	91
1. Assumption 1	91
2. Assumption 2	92
3. Assumption 3	93
4. Assumption 4	94
5. Assumption 5	95
6. Assumption 6	96
C. Radio-frequency Power Supplied to the Plasma	98
1. The conductivity tensor of magneto- plasma	98
2. The distribution of excited electro- magnetic fields	102
3. The power density	110
4. Estimation of the self-inductance of the rf excitation loop	118
5. A method for determining the current in the rf excitation loop and the equivalent load impedance	120
6. Electric scalar potential and charge distribution	125
IV. NUMERICAL ILLUSTRATIONS	129
A. Plasma Parameter Variations	129
1. Electron collision frequency and mobility	129
2. Components of the conductivity tensor	132
B. Circuit Parameter Variations	152
1. The self-inductance of the rf excitation loop	152
2. The current in the rf excitation loop and equivalent load impedance	155
C. Estimation of Time-Varying Electromagnetic Field Strength and Time-average Power Density	158

	Page
V. DISCUSSION OF RESULTS	162
VI. CONCLUDING REMARKS	172
A. Suggestions for Future Studies	175
VII. REFERENCES	177
VIII. ACKNOWLEDGMENTS	185
IX. APPENDIX A: DERIVATION OF EQUATION 3.39, THE EXPRESSION FOR THE TIME-VARYING MAGNETIC FIELD INTENSITY PRODUCED BY THE CURRENT IN AN rf LOOP	187
X. APPENDIX B: DERIVATION OF EQUATION 3.73, EXPRESSION FOR THE SELF-INDUCTION OF rf EXCITATION LOOP	192
XI. APPENDIX C: DERIVATION OF EQUATIONS 3.60, 3.61, 3.62 AND 3.63, THE EXPRESSIONS FOR THE REAL AND IMAGINARY PARTS OF THE COMPLEX POWER DENSITY	198

LIST OF TABLES

Table	Page
1. The values of electron temperature, T_e , the electron number density, n_e , electron mean velocity \bar{v}_e and the degree of ionization, α , interpreted from the Langmuir probe measurement for the case I, at various probe tip positions	76
2. The values of electron temperature, T_e , the electron number density, n_e , electron mean velocity \bar{v}_e and the degree of ionization, α , interpreted from the Langmuir probe measurement for the case III (biased cathode) at various probe tip positions	77
3. Radio frequency power flow measurements	82

LIST OF FIGURES

Figure	Page
2.1. Block diagram representing the sputtering system	18
2.2a. Top view and front view of the sputtering chamber	19
2.2b. Sputtering system magnetic field calibration curve	21
2.3. A typical Langmuir probe characteristic curve	27
2.4a. Probe construction (cutting of vycor tubes)	31
2.4b. Probe construction (L-shaped probe unit)	31
2.5a. The relative position of rf loop, cathode, and the probe units	34
2.5b. Structure of sputtering unit including the Helmholtz coils	36
2.6a. Schematical diagram of electrical network for measurement of Langmuir probe characteristics, include a rf filter circuit	37
2.6b. Photograph showing the instrumentation for the measurement of Langmuir probe I-V characteristics	40
2.7. Sputtering unit electrodes configuration	41
2.8a. Langmuir probe characteristics for the case I (with the floating cathode) with the probe tip located at $x = 1.17$ cm, $y = -0.48$ cm and $z = 1.27$ cm	42
2.8b. Langmuir probe characteristics for the case I (with the floating cathode) with the probe tip located at $x = 4.45$ cm, $y = 0$ and $z = 1.27$ cm	44
2.8c. Langmuir probe characteristics for the case I (with the floating cathode) with the probe tip located at $x = 10.52$ cm, $y = -2.44$ cm and $z = 1.27$ cm	47

Figure	Page
2.8d. Langmuir probe characteristics for the case I (with the floating cathode) with the probe tip located at $x = 4.45$ cm, $y = 0.0$ and $z = 11.43$ cm	49
2.9a. Langmuir probe characteristics for the case II (with the grounded cathode) with the probe tip located at $x = 1.17$ cm, $y = -0.48$ cm and $z = 1.27$ cm	52
2.9b. Langmuir probe characteristics for the case II (with the grounded cathode) with the probe tip located at $x = 4.45$ cm, $y = 0.0$, and $z = 1.27$ cm	54
2.9c. Langmuir probe characteristics for the case II (with the grounded cathode) with the probe tip located at $x = 10.52$ cm, $y = -2.44$ cm and $z = 1.27$ cm	56
2.9d. Langmuir probe characteristics for the case II (with the grounded cathode) with the probe tip located at $x = 4.45$ cm, $y = 0.0$, and $z = 11.43$ cm	58
2.10a. Langmuir probe characteristics for the case III (with the biased cathode in sputtering condition) with the probe tip located at $x = 1.17$ cm, $y = -0.48$ cm and $z = 1.27$ cm	60
2.10b. Langmuir probe characteristics for the case III (with the biased cathode, in sputtering condition) with the probe tip located at $x = 4.45$ cm, $y = 0$ and $z = 1.27$ cm	62
2.10c. Langmuir probe characteristics for the case III (with the biased cathode, in sputtering condition) with the probe tip located at $x = 1.17$ cm, $y = -0.48$ cm and $z = 11.43$ cm	64
2.10d. Langmuir probe characteristics for the case III (with the biased cathode in sputtering condition) with the probe tip located at $x = 4.45$ cm, $y = 0$ and $z = 11.43$ cm	66

Figure		Page
2.11a.	Plasma glow pattern under the sputtering condition for $V_{AG} = -400, V$ (dc)	72
2.11b.	Plasma glow pattern under the sputtering condition for $V_{AG} = -500, V$ (dc)	72
2.12a.	Schematical diagram showing electrical network for rf power measurement for the case when rf power meter is located near the rf loop	79
2.12b.	Schematical diagram showing electrical network for rf power measurement for the case when rf power meter is placed away from the rf loop	80
3.1.	Equivalent circuit for the electrical network under study. z_g = internal impedance of the voltage source, z_0 = characteristic impedance of transmission line	117
4.1.	Variation of electron collision frequency and mobility with electron thermal energy	131
4.2a.	Variation of the real parts of various components of the conductivity tensor with electron mobility, μ , for case $B_0 = 19 G$, and $n_e = 6 \times 10^9 \text{ cm}^{-3}$, with different values of frequency, f	135
4.2b.	Variation of the imaginary part of various components of the conductivity tensor with electron mobility, μ , for case $B_0 = 19 G$, and $n_e = 6 \times 10^9 \text{ cm}^{-3}$ with different values of frequency, f	137
4.3a.	Variation of various components of conductivity tensor with static magnetic flux density, B_0 for case, $f = 27 \text{ MHz}$, $n_e = 6 \times 10^9 \text{ cm}^{-3}$, and $\mu = 2.7 \times 10^5 \text{ m}^2\text{v}^{-1}\text{sec}^{-1}$ (or $KT_e = 4 \text{ eV}$)	139
4.3b.	Variation of various components of conductivity tensor with static magnetic flux density, B_0 for case $f = 27 \text{ MHz}$, $n_e = 6 \times 10^9 \text{ cm}^{-3}$, and $\mu = 8.5 \times 10^4 \text{ m}^2\text{v}^{-1}\text{sec}^{-1}$ (or $KT_e = 8 \text{ eV}$)	141

Figure	Page
4.3c. Variation of various components of conductivity tensor with static magnetic flux density, B_0 , for case $f = 27$ MHz, $n_e = 6 \times 10^9 \text{ cm}^{-3}$ and $\mu = 8.5 \times 10^4 \text{ m}^2\text{v}^{-1}\text{sec}^{-1}$ (or $KT_e = 12 \text{ eV}$)	143
4.4a. Variation of $\sigma_{1r} = \text{Re}(\tilde{\sigma}_1)$ with static magnetic flux density, B_0 for case $n_e = 6 \times 10^9 \text{ cm}^{-3}$ and $f = 27$ MHz with thermal energy as a parameter	145
4.4b. Variation of $\sigma_{1i} = \text{Im}(\tilde{\sigma}_1)$, with static magnetic flux density, B_0 , for case $n_e = 6 \times 10^9 \text{ cm}^{-3}$ and $f = 27$ MHz with thermal energy as a parameter	147
4.4c. Variation of $\sigma_{2r} = \text{Re}(\tilde{\sigma}_2)$ with static magnetic flux density B_0 for case $n_e = 6 \times 10^9 \text{ cm}^{-3}$ and $f = 27$ MHz with thermal energy as a parameter	149
4.4d. Variation of $\sigma_{2i} = \text{Im}(\tilde{\sigma}_2)$ with static magnetic flux density, B_0 for case $n_e = 6 \times 10^9 \text{ cm}^{-3}$ and $f = 27$ MHz with thermal energy as a parameter	151
4.5. Variation of the self-inductance, $L(a, \alpha)$ with the length of horizontal arm of rf loop, a , with $\alpha = (\frac{b}{2a})$ as parameter	154
A.1. The coordinate system and the configuration of u-shaped current filament	188
B.1. Magnetic flux linkage through the rf excitation loop	193

I. INTRODUCTION

The electric gas discharge is a phenomena which is observed when a gas or vapour becomes electrically conducting. Under these conditions free electric charges are present and can move through the gas, usually under the influence of an electric field.

When an atom or a molecule of gas, by absorbing enough energy, loses one electron, it becomes a positively charged particle and is said to be ionized. The products of ionization are thus one electron and a positively charged ion. The positive ion may lose another electron or electrons, and hence become multiply ionized. The process of liberating an electron from a gas particle with either the simultaneous production of a positive ion or the increase of positive ion charge is called ionization. The process of liberating an electron from a solid is usually known as electron emission and is of paramount importance in the study of gaseous conduction in spite of the fact that it occurs only at the discharge boundaries, usually called the electrodes. Electron emission contributes a great deal to the production of charged particles and has a great influence both on the gaseous conductivity and the behavior of a plasma.

There are several ways of creating the various charged particles both by ionization and electron emission.

Ionization can be due to chemical and nuclear processes, excited atoms, thermal ionization, radiation, positive-ion collision or electron collision. The ionization of gas particles by electron collision and by absorption of radiation, also known as photoionization, are the most important ionization processes to be encountered in the study of gaseous conduction and plasma electronics.

Electron emission, on the other hand, can be due to chemical and nuclear processes, field emission, electron impact, positive-ion bombardment, radiation (photoemission) or thermionic emission.

A. Historical Background on Gaseous Plasma Research

The study of the physics of ionized gases has had a long and complicated history.

Between 1831 and 1835 Faraday (1), working at the Royal Institution in England, took up research on gas discharges at low gas pressure. He discovered what he called a glow discharge, which consisted of a series of alternate luminous and dark zones which varied in length and color. These phenomena were observed in tubes filled with air to a few millimeters Hg of pressure while the discharge was maintained by a source of potential of about 1000 V. In addition, Faraday seems to have been the first to observe

that current can pass through a discharge tube filled with a gas at low pressure without showing any luminosity at all. This phenomenon he called a dark discharge.

Subsequently, discharge physics was mainly concerned with research into the various kinds of rays produced by an electric discharge. In 1858 Plücker (2) discovered that a glow discharge working at a pressure of the order of 1/100 mm Hg emits cathode rays. The beam which originates from the cathode colors the gas along its path, and when it impinges on the glass wall of the discharge tube a green fluorescent spot is produced.

It was first thought that mechanism of the transport of electricity through gases was similar to the transport of charges through conducting liquids. However, Crookes, who at that time investigated discharges at low pressure, visualized charge carriers quite different from those assumed to exist in electrolytes. It was probably at the congress in Sheffield in 1874 that he first put forward hypotheses that cathode rays are most likely to be fundamental particles of the atom.

In 1879, Crookes (3) was sufficiently impressed by the novel phenomena observed to conclude that the matter in his discharge tubes existed in a new state - the fourth state of matter. Langmuir (4), in 1928, used the word "plasma" to describe the inner region of an electrical

discharge which was not dominated by wall and electrode effects. The word means a mold or form and is also used for the liquid part of blood in which the corpuscles are suspended. In the present usage it means a state of matter containing electrically charged particles. The definition does not require that every particle be ionized; Crooke's discharges, for example, consisted of gases that were only partially ionized.

It should be pointed out that Langmuir restricted the term "plasma" to that part of the discharge remote from the boundaries. The physical significance of this is that particles within the plasma region are not influenced by the boundaries of the discharge. Between the plasma proper and the potential surface which the boundary represents, there exists a transition region called the "plasma sheath." The sheath region has properties that differ from those of the plasma, and the motions of the charged particles within the sheath are influenced by the potential of the boundary. The sheath particles form an electrical screen between the plasma and the boundary.

A criterion that will qualify a partially ionized gas as a plasma can be stated as follows: a partially ionized gas must have a volume larger than that of a sphere with a radius equal to the screening distance, which is a function of the density and temperature of the charged

particles.

A commonly accepted broader definition of plasma can be given as "any collection of charged particles sufficiently dense that the space-charge effect can result in strongly coherent behavior." For example, an ionized gas can be called a "plasma" only if its dimensions (ℓ) are much larger than a Debye length (5) λ_D , where $\lambda_D = [KT/(4\pi e^2 N)]^{1/2}$, in which N denotes the particle number density, in particles/cm³, e denotes the electronic charge, and (KT) denotes the energy of random motion in eV.

It should be noted that in a plasma with a low density of charged particles, the presence of neutral particles lessens the effect of the interaction between charged particles. Although there are enough charged particles to satisfy the plasma definition they are still too sparse in the gas, compared with the much larger number of neutral particles, to interact strongly with each other. The collision between particles is governed by the laws of force between the interacting particles.

Collision between charged particles obeys the Coulomb force law and depends upon the inverse of the square of the separation distance. Collisions involving at least one neutral particle, however, are governed by forces that are significant only in close proximity to the atom or molecule involved. The dependence upon separation, for example, may

be with the inverse fifth power, therefore, as the degree of ionization of the gas increases, the collision behavior of the plasma changes, and Coulomb interaction becomes increasingly important. The plasma state is characterized by a mean particle energy high enough to maintain a charged particle density that satisfies the plasma criterion (the screening distance criterion). In general, the mechanism that maintains the plasma is the ionization of the neutral particles by impact with other particles. When the energy source maintaining the plasma is an applied electric field, the electron plays a dominant role in impact ionization. Other phenomena in which electrons may play a dominant role are the electrical conductivity of the plasma and its interaction with electromagnetic fields.

B. Cathodic Sputtering System

It should be noted that the works of Langmuir (4, 6, 7, 8, 9) and his coworkers on gaseous discharges have served as the foundation for many practical electronic devices used for the generation, rectification, and control of electrical energy. The plasma phenomena have been applied in various areas of scientific and engineering endeavor. One of these is the area of the thin-film deposition by the sputtering method. Cathodic sputtering has had a long and complex history that began in 1852 with

the original observation by Grove (10) of the formation of an electrically conducting deposit in his experiments on the electrochemical polarity of gases.

In 1858, Plücker (2) noted that an electrical discharge in an evacuated tube with two electrodes was accompanied by a loss of material from the cathode. The matter lost by the cathode deposited itself on the neighboring surfaces and could even redeposit itself on the cathode. This phenomenon has been named "cathode sputtering."

Cathode sputtering is well known to scientists who used the old method of x-ray production by ionization of air in a vacuum tube. The positive ions produced by the discharges concentrate at the cathode. A hole begins to appear in the latter, and its materials begin to evaporate. It was not until 1906 that Kohlschutter and Müller (11) explained this loss of material as a consequence of the impact of positive ions from the plasma on the cathode.

The early history of sputtering was primarily involved with establishing a mechanism for this phenomena (12). With the development of the gas diode, however, sputtering was studied as a problem to be eliminated (13).

Sputtering for the purpose of film preparation can be said to date from the original observation by Grove but was primarily used for ornamental application until about 1928. However, as early as 1925 sputtered nickel films

were investigated for their magnetic properties (14), and by 1928 Western Electric Company was employing sputtering for an electronic application (15), i.e., the manufacture of phonograph records and contacts on microphone transmitters. By 1959, sputtering was employed for the newly conceived microminaturization by tantalum thin film (16, 17). The refractory metal could be used for interconnections, resistors, and capacitors. By 1962, sputtering had gone automatic; it was then used for the gold termination of resistors (18) and, in 1964, for the deposition of tantalum (19).

Sputtering techniques and associated phenomena have been reviewed by Wehner (20), Maissel (21), and Moore (22). Sputtering of compounds intact from a single source has been reported by Froeml (23). The important new techniques for deposition are radio-frequency (rf) (24), rf plus dc (25), asymmetric (26), bias (27), getter (28), and reactive sputtering (29).

Undoubtedly, one of the most significant technological advances has been rf sputtering, which has enabled workers to sputter a wide range of substances at sufficiently low pressure to give a high deposition rate. It is surprising that the wide application of rf sputtering was so long delayed. In 1931, Banerji and Grangoli (30) reported material deposits occurring in an rf discharge, and wall

sputtering was certainly observed from the glass envelopes used for electrodeless discharges by early workers. Holland (31) has reviewed early and contemporary work on rf sputtering up to 1970.

It should be pointed out, however, that until the last decade or so the majority of thin-film deposition has been done by thermal evaporation from resistance heated sources or from electron beam heated sources. With the advent of modern sputtering techniques, the application of sputtering for thin-film deposition has been given widespread attention. The major reasons that sputtering is chosen over other competitive processes are the ability to deposit uniformly on nonconducting surfaces, the ability to deposit different materials such as refractory metals like tantalum at a reasonable rate, and the capability for compound and alloy deposition.

The idealized technique for cathodic sputtering is quite simple as only four or five main components are necessary. They are the cathode or source of material, the anode or means of electrical conductivity, the plasma or energy source, and the substrate or deposition site. The items are contained in a partially evacuated sputtering chamber filled to a low pressure with an inert gas, usually argon. A high potential is applied to the electrodes to attract positive ions from the plasma, which are accelerated

to the surface of the cathode. Atoms of the cathode are dislodged from the cathode surface by momentum transfer from the ions, acquire kinetic energy, and leave the cathode as sputtered atoms. Approximately 1% of the atoms are charged; the remainder are neutrals (32).

The operation of a sputtering system is normally carried out at a gas pressure of from 5 to 500 mTorr in the chamber. A dc voltage of from 500 to 10,000 V is applied between the cathode and the anode to generate the plasma and induce sputtering. Variants of this technique include the application of additional electrostatic or magnetic fields, the use of an electron or ion beam, and the use of rf energy to enhance the sputtering processes.

The plasma used in the system has received considerable attention from a large number of workers (32, 33, 34). Earlier investigators who worked on the cathode sputtering problem did not obtain important results, primarily because the cathode or the target was introduced directly into the plasma. In addition, the ions forming the plasma were distributed isotropically with poorly defined energies, and the chemical composition of the plasma was not known. The experiments started yielding interesting results when the investigators were able to use ionic sources that yielded well defined beams of ions with uniform energy (35, 36).

This research opened new avenues in the study of the

effects of ions on matter. The primary thing that is considered in sputtering is the sputtering yield, which depends on the nature of the ions, their energies, the nature of the target, and the angle of incidence.

Rol et al. (37) have shown that the yield increases greatly at grazing incidence. G. K. Wehner (38) has measured the yield at low energies (a few keV), and Moore (39) has shown that a maximum exists in the energy range of 6 to 12 keV. This last result is to be expected since the effective collision cross section between the ions and the target atoms decrease rapidly as the energy increases.

The sputtering rate, in general, can be increased by increasing the ion density at the surface of the target. This can be accomplished, at a given pressure and accelerating voltage, by changing the linear path of the electron flow into a helical path, thus increasing the number of ionizing collisions which occur. This is done by using an external magnetic coil to generate an axial magnetic field. Increases in sputtering rate of a factor of 2 to 5 are commonly achieved using this technique (40). Penning and Moubis (41) taught the beneficial use of a magnetic field for suppressing electrons or for increasing the plasma density.

The rf source may be used to directly excite the free electrons present in the system, producing a glow discharge

at very low pressures. The use of this technique has several advantages:

- (1) Film uniformity is very good
- (2) No thermionic source is required and the rf reactive evaporation can be used conveniently.

Various combinations of rf-induced or rf-sustained discharges with a dc sputtering system have been used (42, 43). Systems of this type usually produce a higher sputtering rate than is expected from a simple dc system since the ionizing electron collisions are increased by the oscillating rf fields.

It should be noted that there are three sources of interference from a rf sputtering system; this occurs at the power supply and connecting lines, the plasma, and the power input line (44).

The most meaningful requirement for optimum operation of a rf sputtering system is the ability to match the output of the rf supply to the load properties of the plasma, a problem which does not exist in dc sputtering. Obviously, some form of matching "transformer" is required to optimize the system. A well-designed matching network should be placed as close to the target as possible to minimize losses and should contain tunable elements to compensate for changes in load due to different power

levels, gas pressures, and the target materials. It should also be able to absorb large amounts of rf power in case of an accidental mismatch.

From the above discussion, it is not difficult to see that an understanding of cathode sputtering processes has contributed to the improvement and development of thin-film technology in recent years, and that utilization of sputtering techniques is likely to continue in the future.

Investigators (43) at Iowa State University have developed an experimental sputtering facility, similar to that described by the investigators (45) at IBM Company for amorphous film fabrication. These investigators were primarily interested in the deposition of thin films, control of film thickness, and other related fabrication problems but the sputtering rate control should be of great interest to them. It should be noted that the rate of sputtering depends not only upon the physical condition of the plasma, and the applied electric and magnetic field configurations (40), but also upon proper instrumentation for the sputtering system (44).

It appears that sufficient attention has not been given to the plasma phenomena encountered in the sputtering system used by these investigators, nor has enough consideration been given to the proper instrumentation for achieving an optimum operation of the sputtering system. It is there-

fore desirable to make a detailed study of the argon plasma used in the rf plus dc sputtering system employed by the investigators at ISU, since the effective use of sputtering as a tool will best be achieved by those who understand these basic mechanisms and the limitations of the sputtering under consideration.

C. Statement of the Problem

In the sputtering system to be studied, the argon plasma is excited separately from the sputtering ion-accelerating potentials. Its power is derived from a 27 MHz transmitter, amplifier, and matching network. The output of the latter is connected to an antenna which is a water-cooled current loop (double ended feed) situated inside the bell jar (see Figure 2.2).

In order to effectively use argon plasma in cathodic sputtering for thin-film deposition, it is necessary to know some of the basic physical parameters of the ionized argon gas (plasma), such as electron density and temperature. It is also necessary to be able to predict the behavior of the plasma under the influence of externally applied static magnetic and electric fields so that it can be controlled effectively. On the other hand, in order to utilize the rf power effectively, it is necessary to know how the rf power source sees the load, which consists of

the radiating antenna and the surrounding plasma, so that an appropriate matching network can be designed for achieving the maximum power transfer.

As has been pointed previously, for a weakly ionized gas (which is the case under study), electron behavior plays a primary role in various related phenomena. Consequently, in the present study, attention is to be focused on the electron behavior in the plasma.

The main purposes of this study are:

1. To design a diagnostic tool and measure the electron density and temperature of the argon plasma.
2. To study the effect of an externally applied static magnetic field on the conductivity tensor of the plasma.
3. To characterize the rf load impedance representing the combination of the antenna and surrounding plasma.
4. To develop a method of analysis for the rf-excited sputtering system under investigation.

The approaches taken are outlined as follows: The ionized argon gas is treated as a conducting medium which can be characterized by conductivity tensor. This conductivity tensor, in general, is a function of static magnetic flux density B_0 , charged particle density, electron-collision frequency ν , and the frequency of the rf excitation current

flowing in the rf loop. On the other hand, the collision frequency is a function of electron temperature and electron density, which are to be measured experimentally. The experimental data obtained with the aid of Langmuir probes are shown and discussed in Section II. Expressions for the conductivity tensor, (the power density absorbed by the plasma) are derived theoretically in Section III with the aid of Maxwell's field equation, the equation of momentum transfer (Langevin equation), and the continuity equation. Various numerical illustrations are shown in Section IV.

II. EXPERIMENTAL MEASUREMENTS AND OBSERVATIONS

A. Description of the Sputtering Equipment

The basic block diagram for the sputtering system is shown in Figure 2.1. The top and front view of the sputtering chamber are shown in Figure 2.2a. The sputtering system includes the high vacuum chamber, the argon gas distribution tube, the rf plasma excitation current loop, the Helmholtz coils, the target rod (cathode), and the top plate.

The high vacuum chamber is a cylindrical glass bell jar which has a 10 in. o.d. and is 12 in. high. The bell jar sits on a stainless steel plate which has a number of feed-through provisions.

The argon gas distribution tube is made of 1/4 in. copper tubing which forms an 8 in. diameter circular ring.

The "U"-shaped rf plasma excitation current loop is made of 1/4 in. o.d., and 3/16 in. i.d. copper tubing, covered with a 7/16 in. o.d., 3/8 in. i.d. vycor tubing.

The Helmholtz coils are made of 100 turns of copper wire each, and have a diameter of 25 in.

The target rod (cathode), is made of iron, and is 1/4 in. in diameter and 8 in. in length.

The top plate is made of aluminum, 3/4 in. thick and 12 in. in diameter, and has eleven feed-through provisions.

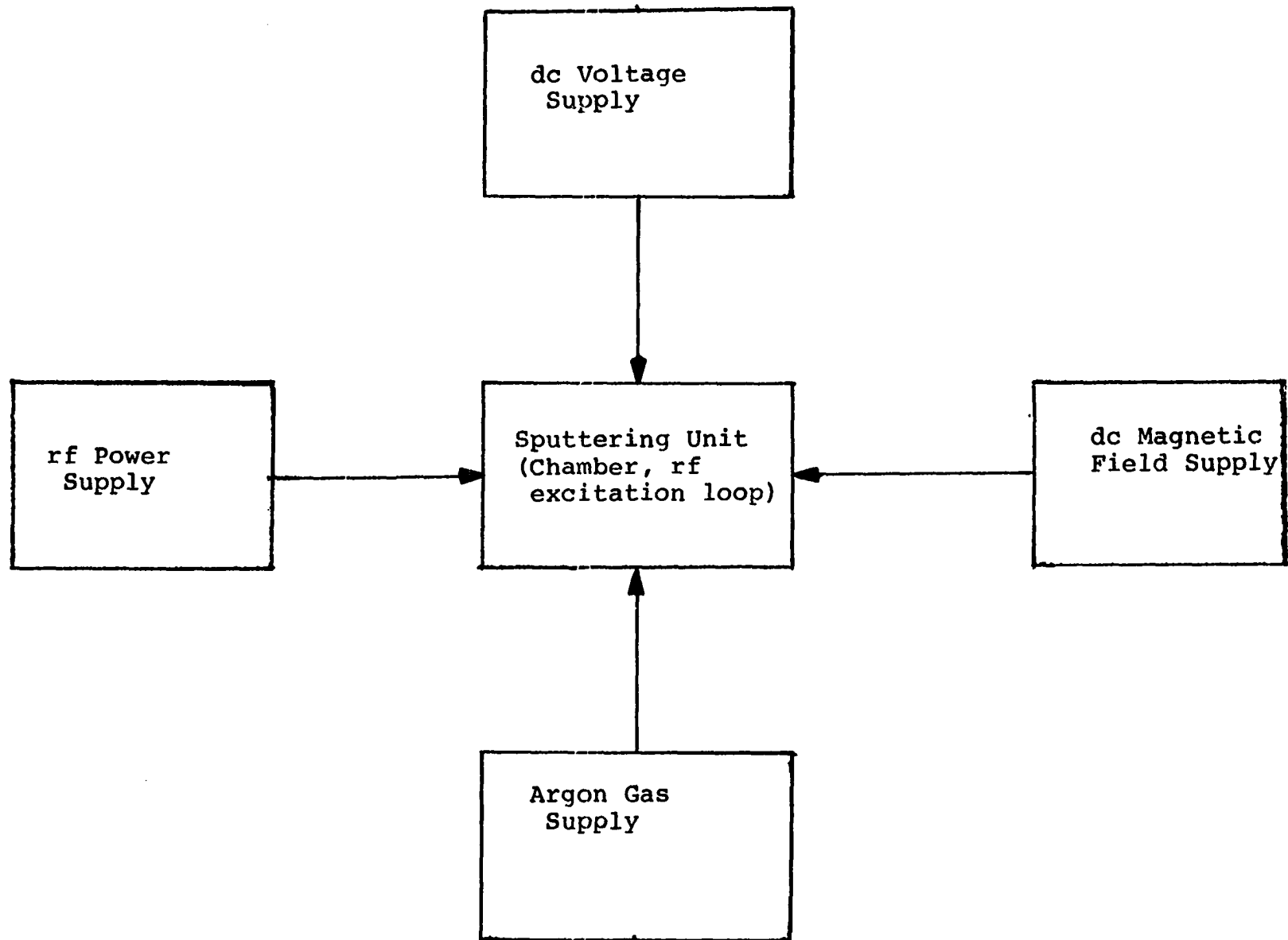


Figure 2.1. Block diagram representing the sputtering system

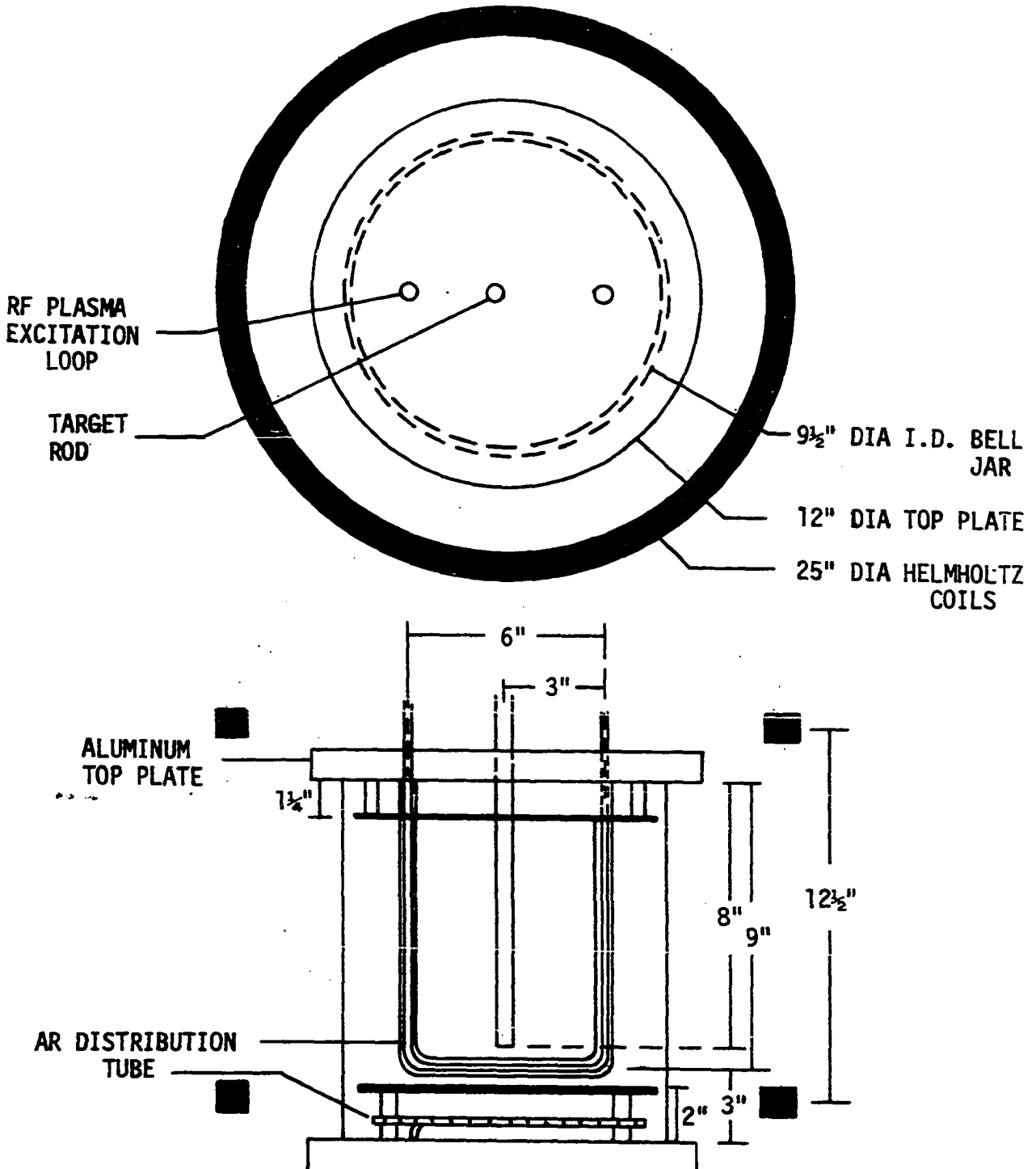


Figure 2.2a. Top view and front view of the sputtering chamber

1. Argon plasma production by rf current loop

An argon plasma in a sputtering unit is produced by the following procedure: a background pressure inside the bell jar is maintained at a pressure of 2.8×10^{-7} Torr. The argon gas is injected into the bell jar vacuum through a 1/4 in. copper tube until the pressure reaches approximately 7.5×10^{-4} Torr. The constant d.c. magnetic field is applied through application of a d.c. current in the Helmholtz coils. After the argon gas is ignited with the aid of a tesla coil, the rf power is supplied through an rf loop, imbedded in the argon gas in order to obtain an effective ionization process.

2. Helmholtz coils

The function of the Helmholtz coils is to create a uniform static magnetic field, parallel to the axes of the bell jar, which will control the charged particle motion in the azimuthal direction due to the Lorentz force seen by the charged particle. This uniform static magnetic field is maintained with the aid of a constant dc current supply. The relationship between the dc current in the Helmholtz coils and the static magnetic field strength produced in the sputtering unit can be obtained from the calibration curve provided in Figure 2.2b.

It should be noted that the trajectory of a charged

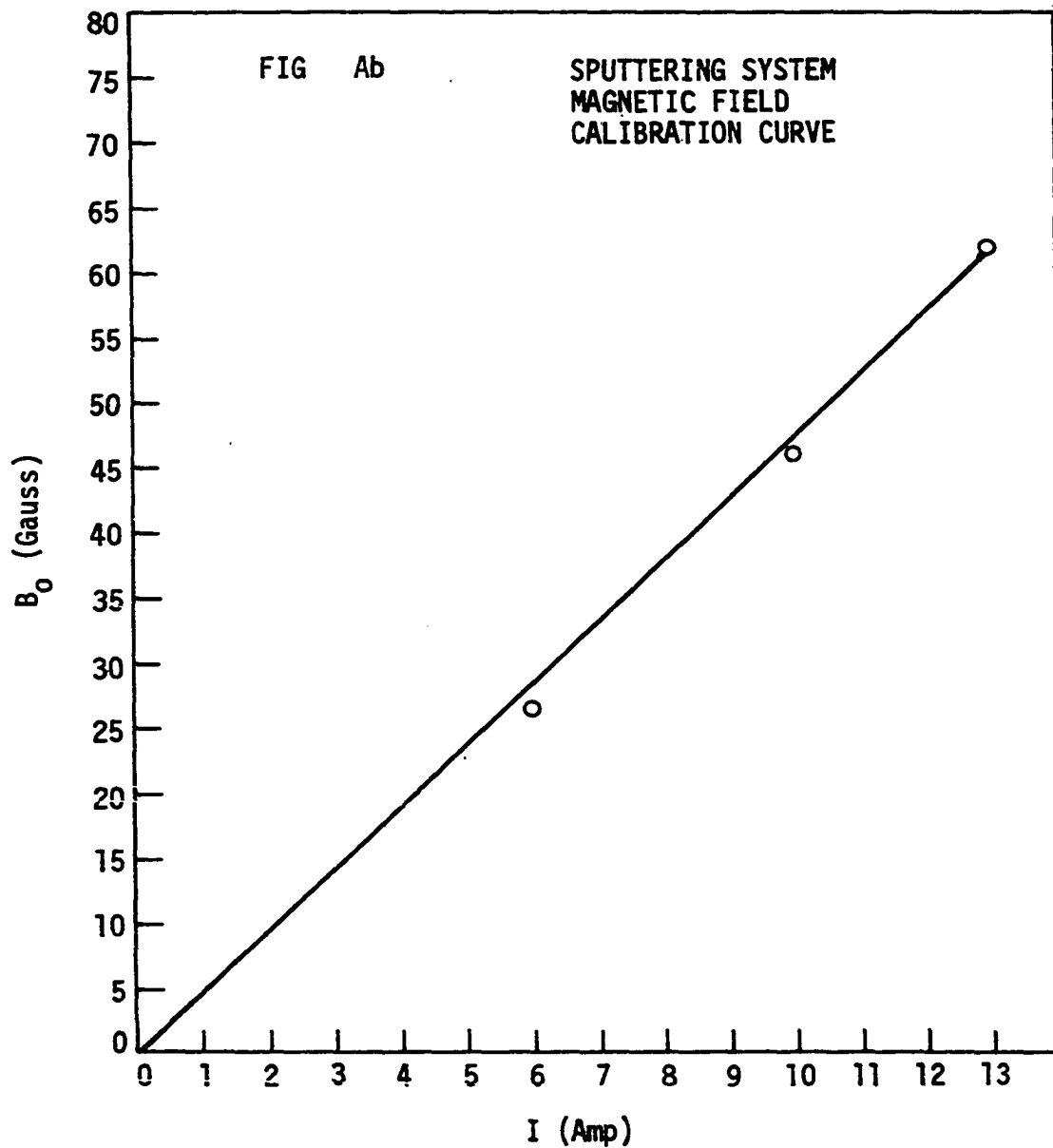


Figure 2.2b. Sputtering system magnetic field calibration curve

particle will be altered when electrostatic bias is introduced. Introducing an electrostatic field will produce a force in the radial and axial directions. That force will cause acceleration in the radial and axial directions, causing electrons to accelerate in a spiral direction.

3. Center-rod cathode and the grounded anode

The center-rod cathode is iron, a magnetic material. When a negative potential is applied to the rod, it creates a dc static electric field between the cathode and the anode. The positive ions will be accelerated by the electrostatic field, so that the bombardment of high energy ions will cause ejections of atoms from the cathode material which will be deposited upon any element in the sputtering unit.

B. Plasma Diagnostics and the Langmuir Probe

Plasma diagnostics and, in particular, the determination of electron density, play an important role in the studies of the thermonuclear power generation, radio propagation, and gas discharges. Among the various methods (46, 47, 48) which have been used, the two categories most widely used are the microwave methods and the Langmuir probe method.

Detailed analyses of the microwave methods and their

advantages as well as their limitations compared with other diagnostic techniques, have been given by Golant (49) and Heald and Wharton (50). For example, one of the advantages of the microwave technique is the use of low powers which do not disturb the plasma. However, the technique has a drawback in that it only permits determination of the average density across the plasma rather than the local density. In addition, special care in actual interpretation of results is required when using these methods. Complications arise because of the interaction of electromagnetic waves with the plasma, variations of density along the path of propagation, and the presence of glass walls which confine the plasma.

One of the most attractive tools for plasma diagnostics is the Langmuir probe, which is simple to use and can provide local measurement of electron density, temperature, energy distribution, and plasma potential. Langmuir probes, in spite of their many inherent deficiencies, play an increasingly important role in modern plasma diagnostics. Firstly, their capability for sampling the ionized gas locally makes it possible for investigators to scan a column of plasma using a movable probe. Secondly, the probe characteristics curve contains information on the energy distribution at least of the electrons, but, in principle, also of the ions at the location of the probe.

For the present investigation, it is felt that the Langmuir probe method is more suitable than the microwave method because the curvature of the cylindrical surface of the bell jar wall would make interpretation of the microwave measurements more difficult.

1. Theory of the Langmuir probe

a. Static probe theory Langmuir probes have been discussed extensively in the literature (6, 7, 51-59). A Langmuir probe consists of an uninsulated piece of metal that can be immersed in a plasma. The potential on the probe is varied, the current to the probe for deficient potentials is measured, and thus a characteristic curve is obtained. The characteristic curve supplies information about plasma parameters such as electron temperature, electron density, plasma potential, and electron energy function (60).

According to the Maxwellian energy distribution, at the plasma potential, $(n_e \bar{v}_e / 4)$ electrons and $(n_i \bar{v}_i / 4)$ ions will reach the unit area of the probe per unit time. Thus the ratio of the electron to ion current is given by

$$\left(\frac{I_{re}}{I_{ri}}\right) = \frac{\bar{v}_e}{\bar{v}_i} = \sqrt{T_e m_i / (T_i m_e)} \quad (2.1)$$

where \bar{v}_e , \bar{v}_i , T_e , T_i , and m_e , m_i are average random speeds, temperatures, and masses for electrons and ions, respective-

ly. At the plasma potential ion current is completely masked by electron current. The total current is $I = (I_i + I_e)$. In the retarding field region, if the electrons have a Maxwellian velocity distribution, the electron current I_e will be

$$I_e = eAn_e \frac{\bar{v}_e}{4} \exp \left[-\frac{eV}{KT_e} \right] \quad (2.2)$$

where $V = V_p$ (probe potential) - V_a (applied voltage), A is the area of the probe exposed to plasma, e is electronic charge, K is Boltzmann's constant, \bar{v}_e is the average random speed for electrons.

If a logarithm of the current I_e is plotted against applied voltage V_a , the plot so obtained yields the electron temperature as given by the following equation:

$$\frac{d}{dV_a} [\ln I_e] = \frac{e}{KT_e} = \frac{11.600}{T_e} \quad (2.3)$$

At the plasma potential the random electron current is

$$I_{re} = eAn \left(\frac{KT_e}{2\pi m_e} \right)^{\frac{1}{2}} = eAn(\bar{v}_e/4) \quad (2.4)$$

so that the electron density (61)

$$n = \frac{I_{re}}{eA} \left(\frac{2\pi m_e}{KT_e} \right)^{\frac{1}{2}} = \frac{4I_{re}}{eA\bar{v}_e} \quad (2.5)$$

The part of the probe curve below plasma potential is

known as the retarding field region, and the region above plasma potential where electrons are attracted to the probe is known as the electron saturation region. In the saturation region, too, there is an increase of probe current with the increase of voltage. This is due to the electron sheath formation around the probe. The growth in sheath is sufficient to maintain the rate of current increase which exists in the retarding field region. This phenomenon decreases the rate of current above plasma potential. As a result, there is a deviation from the straight line which exists in the retarding field region. The point where a deviation from a straight line on a $(\ln I_e)$ versus V_a plot occurs is an indication of the plasma potential. Since there is no discontinuity in the probe curve, a slight error in location of plasma potential may result. The use of two tangents, one below and one above the knee, determines fairly well the location of plasma potential. The idealized probe curve is shown in Figure 2.3.

b. Ion current data Using ion current data, a similar argument could be made for density determination. Since the ion current depends not on ion temperature but on electron temperature, the formula for random ion current has been shown (55) as

PROBE CHARACTERISTIC CURVE

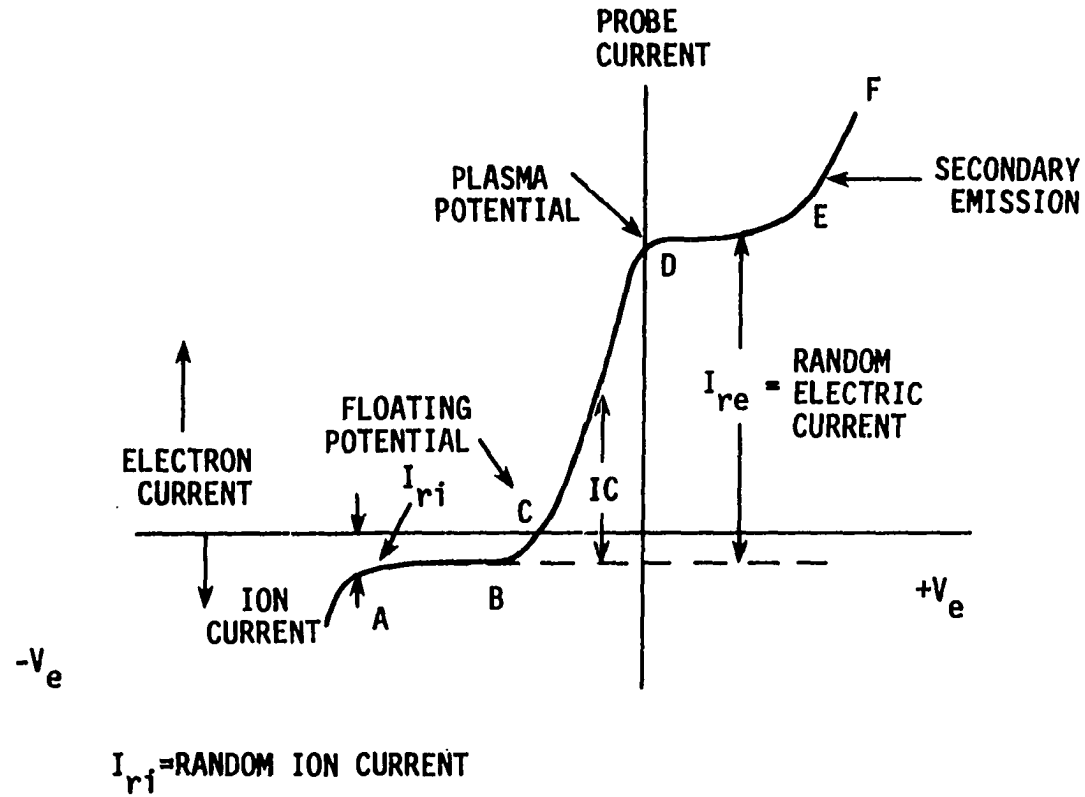


Figure 2.3. A typical Langmuir probe characteristic curve

$$I_{r_i} = 0.6 A e n_i \left(\sqrt{\frac{kT_e}{m_i}} \right)^{1/2} \quad (2.6)$$

from which n_i can be found. Here n_i is the ion density, and m_i is the ion mass. A common method for analyzing ion current data is to extrapolate the probe current curve at large negative potentials (where the ion current curve shows linearity) back to plasma potential. There are a number of factors which serve to complicate the problem, including the possibility of ions which orbit but do not strike the probe, and the necessity of including the effects of both ions and electrons on the shielding of the probe in a relatively exact manner. The existing theories all indicate that for cases where $T_e > T_i$, the ion velocity at the sheath edge is proportional to the electron temperature rather than the ion temperature. Ion current variations at plasma potential (where the no sheath model applies) cannot be verified experimentally because the ion current is completely masked by electron current.

2. Design and construction of the Langmuir probe

In order to design the Langmuir probe for the diagnostics of the argon plasma under study, two basic requirements should be considered: (a) the probe unit must be sufficiently small to avoid any serious disturbance of plasma due to the presence of probe unit; (b) the electrode areas

which will be exposed to the plasma, must be extremely small so that the excess drainage of charge carriers can be prevented.

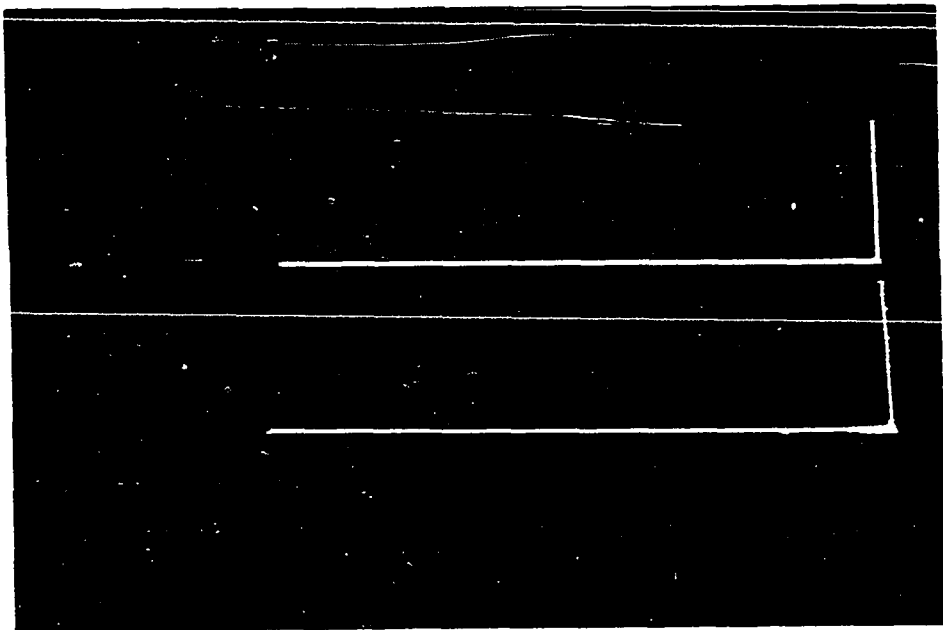
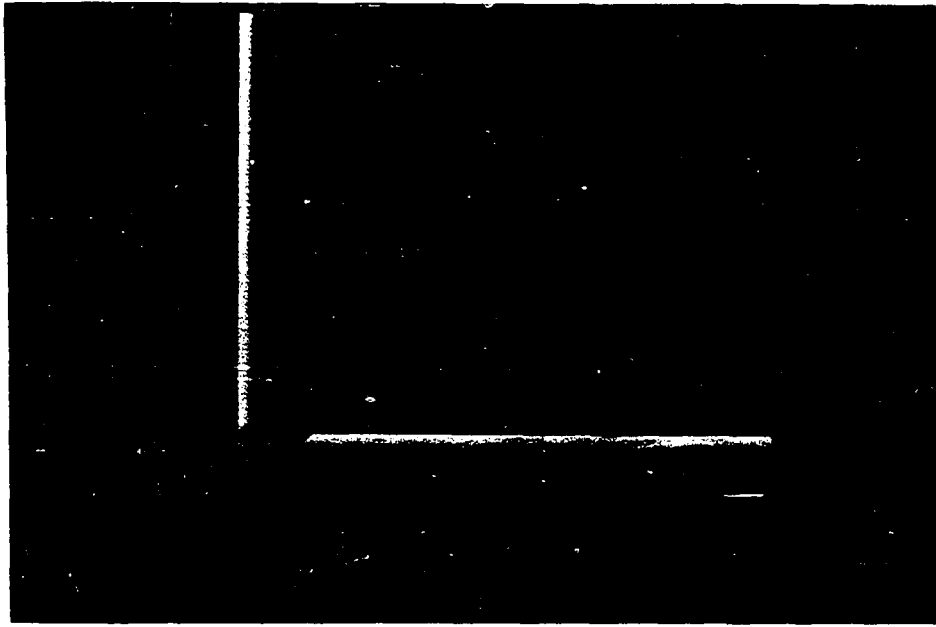
Two pieces of 96% silica glass tubes with a 6 mm o.d. and a 4.2 mm i.d. (one 4 in. long and the other 15 in. long) are jointed together with the aid of a low vapor pressure Torr seal, to form an L-shaped Langmuir probe unit, as shown in Figure 2.4a. The 96% silica glass tube is made by the Corning Glass Works Company and carries the trade name "vycor." Each probe unit contains four probes. Each probe is made of 0.007 in. diameter high temper gold wire (24 K, with 99.97% purity). The four gold wires are threaded through the four barrels of 0.5 mm diameter provided by a ceramic tube having a 3.4 mm o.d. This ceramic tube is made by the McDaniel Refractory Porcelain Company and carries the trade name "McDaniel 998 Alumina Tube." The ceramic tube, with the threaded gold wires, is then inserted into the vycor tube, and thus the gold wire probes are kept separated from each other. The tips of the four probes are spaced $3/4$ in. apart along the horizontal arm (the shorter arm) of the L-shaped probe unit (see Figure 2.4b).

All materials used in the construction of the probe unit are chosen to be able to withstand the high temperatures encountered during the sputtering process.

The relative positions of the rf excitation current

Figure 2.4a. Probe construction (cutting of vycor tubes)

Figure 2.4b. Probe construction (L-shaped probe unit)



loop, the center-rod cathode, and the probe units are shown in Figure 2.5a. The sputtering unit, the Helmholtz coils, and the probe unit inserted into the sputtering chamber are shown in Figure 2.5b.

3. Instrumentation for measurement of current voltage characteristics of the Langmuir probe

The necessary instrumentation for obtaining the current-voltage (I-V) characteristics of the Langmuir probe is schematically represented by the electrical network shown in Figure 2.6a. The experimental set up permits the probe potential with respect to the ground to be varied at will by adjusting the dc power supply setting, from -120 V to +50 V (dc), while the dc probe current in the milliamperere range is being monitored.

Although the dc I-V characteristic of the probe was desired, interference by the ac signal was encountered. Due to the fact that various measuring instruments such as the dc ammeter and dc voltmeters were located too close to the rf excitation current loop, which radiates at 27 MHz, they picked up sufficient amounts of rf energy that the needles of the meters fluctuated and thus were difficult to read; in addition, erroneous readings were introduced.

In order to eliminate the undesirable effects of rf signal interferences, the following arrangements were used

(a) A rf filter was used: An L-C series circuit was

Figure 2.5a. The relative position of rf loop, cathode,
and the probe units

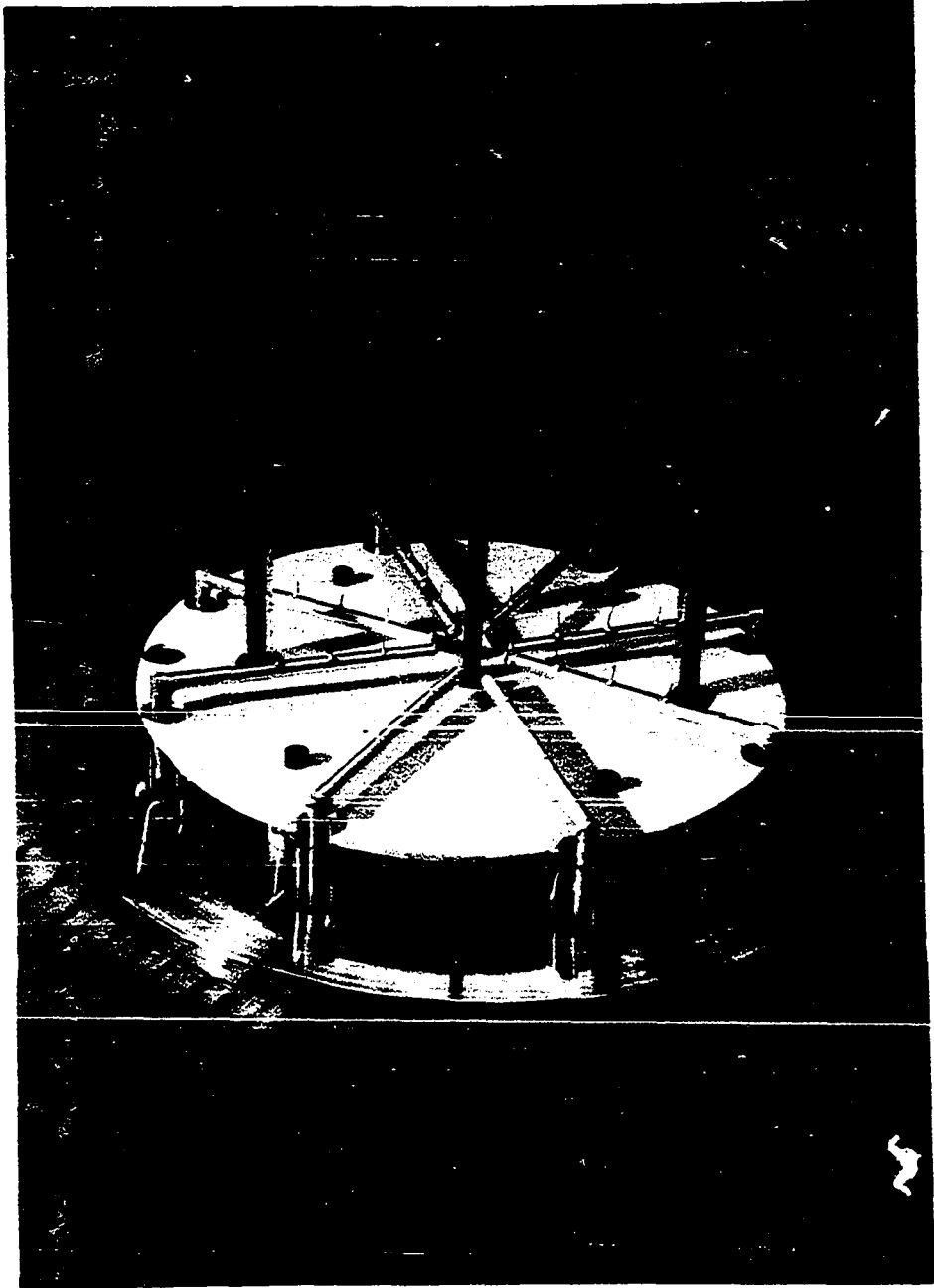
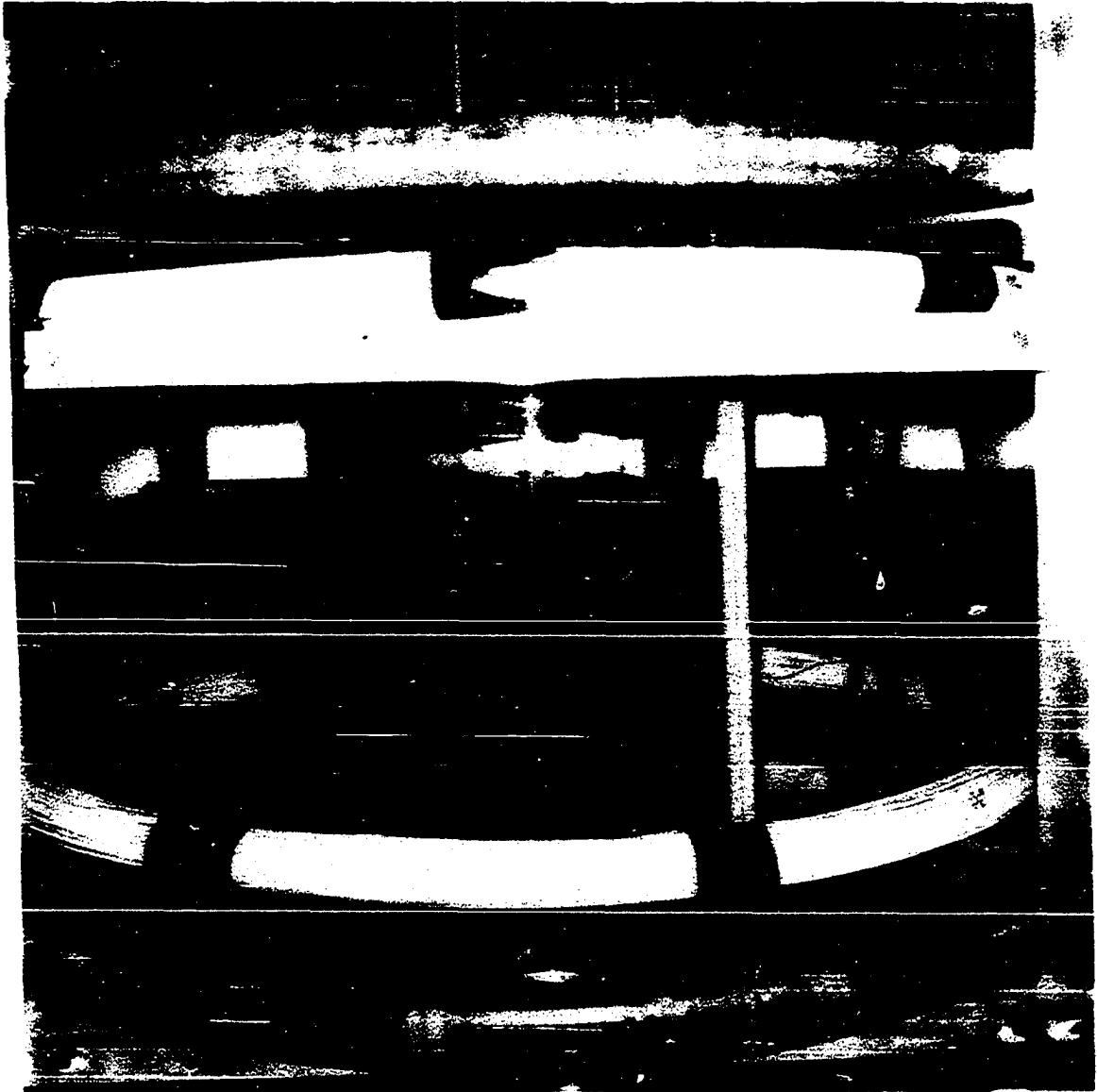


Figure 2.5b. Structure of sputtering unit including the Helmholtz coils



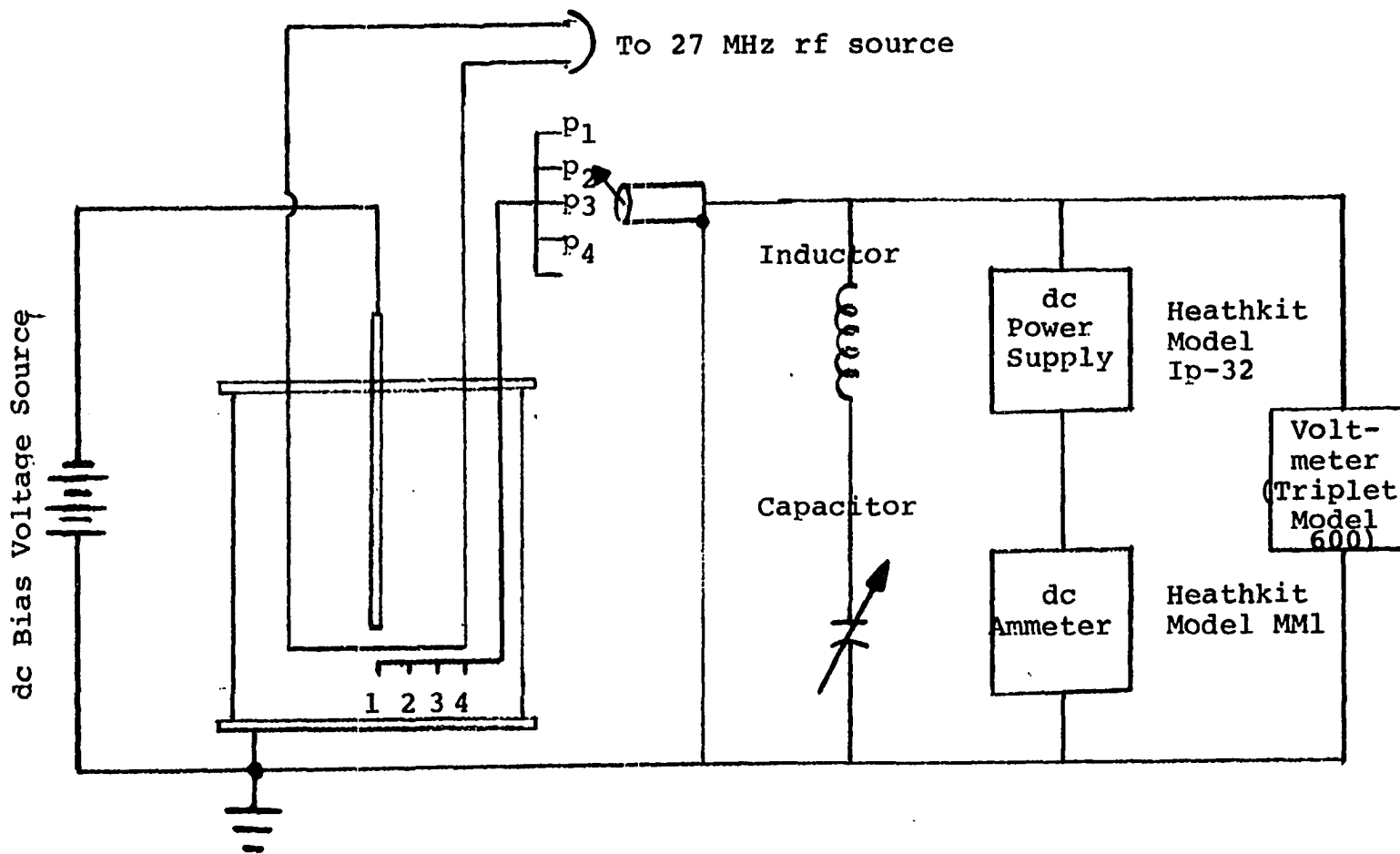


Figure 2.6a. Schematical diagram of electrical network for measurement of Langmuir probe characteristic, include a rf filter circuit

shunted across the dc power supply and the ammeter (see Figure 2.6a) to provide a proper path for the rf current. With properly chosen values of inductance and capacitance, the rf current can be shorted to the ground through this path, so that the amount of ac current flowing through the dc meter path can be minimized or eliminated. (b) Properly shielded connecting cables were used to prevent pickup of the rf signal. (c) The monitoring dc meters were placed inside a steel cabinet enclosure (see Figure 2.6b), in order to minimize the influence of the rf signal generated by the rf excitation loop.

With the above arrangement a sharp improvement was achieved so that accurate experimental data was obtained.

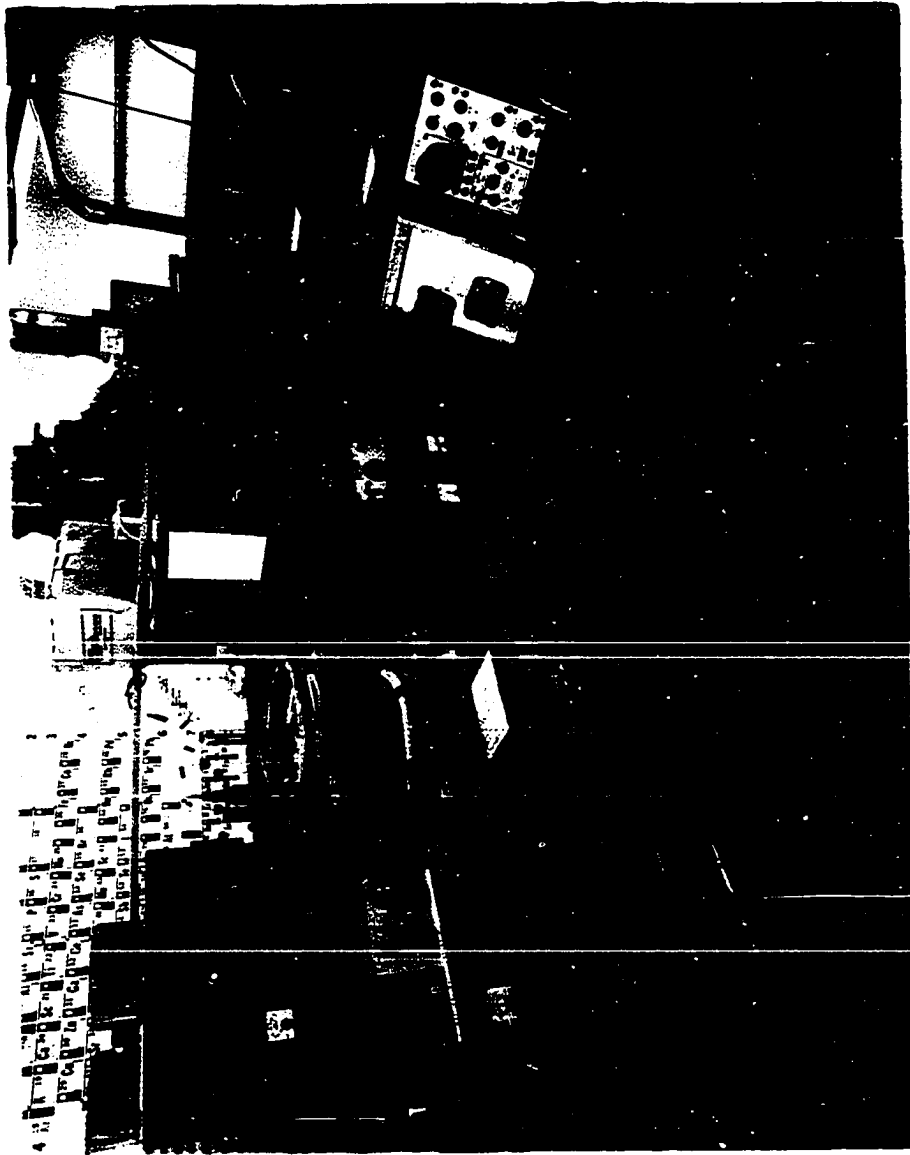
Measurement of dc electric potential with respect to the ground at various boundary surfaces of the sputtering unit, as shown in Figure 2.7, was also made.

It should be noted that a slight variation of the dc potential on the top plate of the bell jar occurred. The diffusion of the charged particles toward the boundary undoubtedly plays a role in the potential distribution on the boundary.

4. Illustrations of I-V characteristics obtained

The I-V characteristics of Langmuir probe obtained are shown in Figures 2.8a,b,c,d, for the case of a floating

Figure 2.6b. Photograph showing the instrumentation for the measurement of Langmuir probe I-V characteristics



V_{AG}	V'_{BG}	V''_{BG}	V'''_{BG}	V_{CG}
20.0V	-9.5V	-11.2V	-11.5V	0.0V

Electrical Potential at Various Boundaries
of the Sputtering Unit

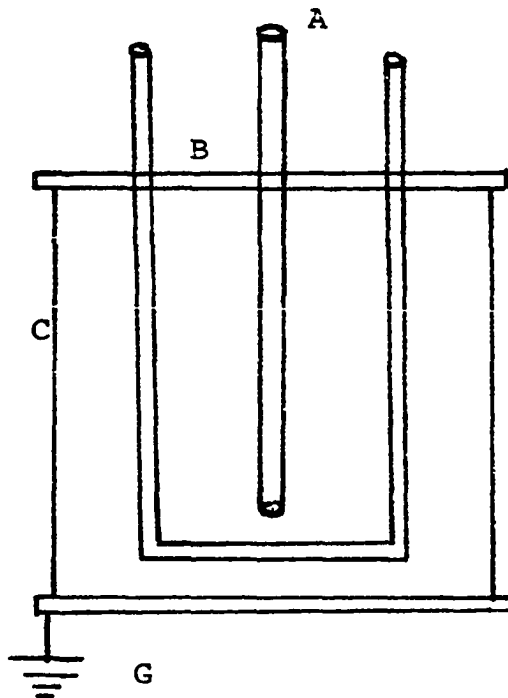


Figure 2.7. Sputtering unit electrodes configuration

Figure 2.8a. Langmuir probe characteristics for the case I (with the floating cathode) with the probe top located at $x = 1.17$ cm, $y = -0.48$ cm and $z = 1.27$ cm

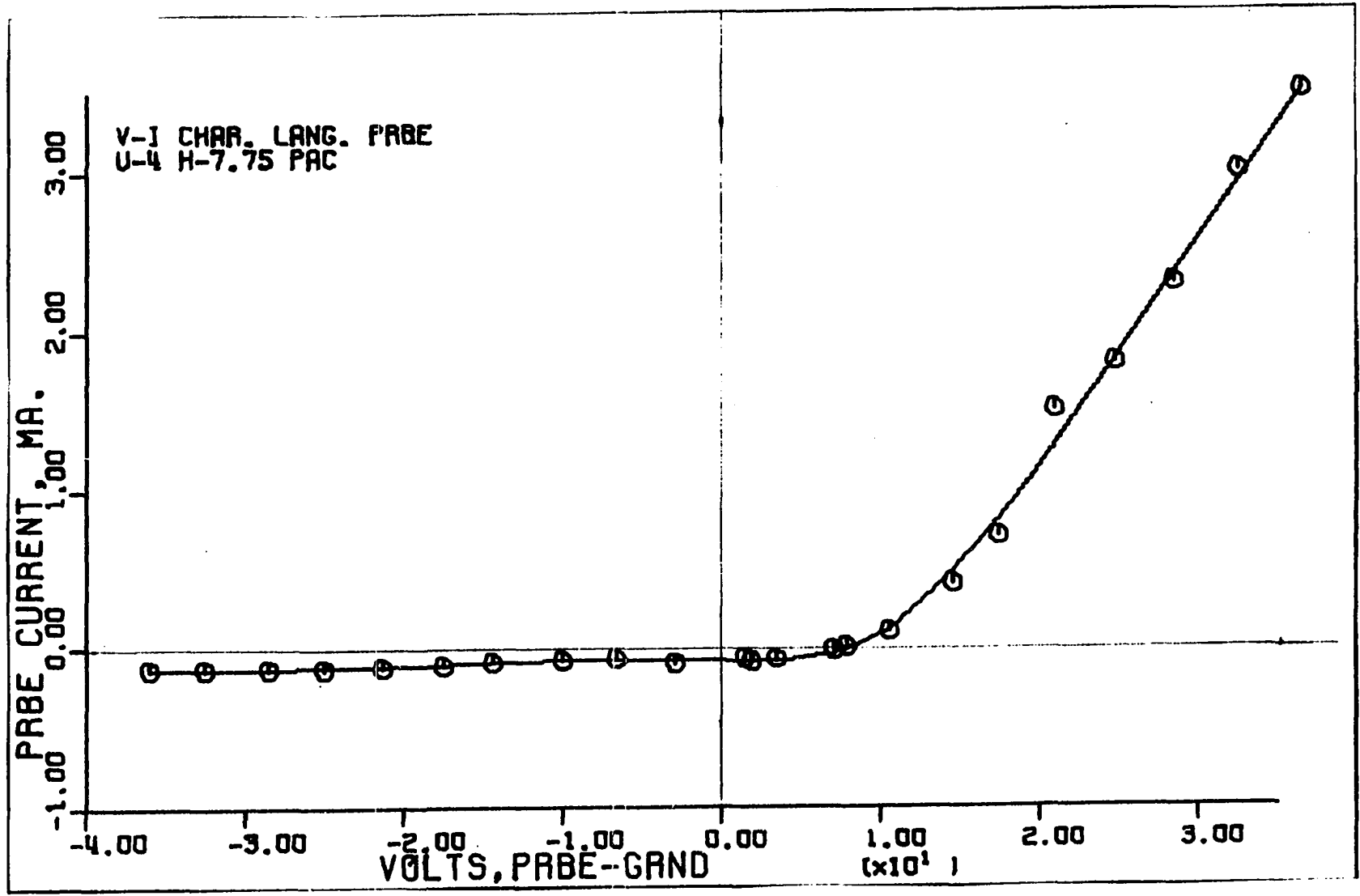


Figure 2.8b. Langmuir probe characteristics for the case I (with the floating cathode) with the probe tip located at $x = 4.45$ cm, $y = 0$ and $z = 1.27$ cm

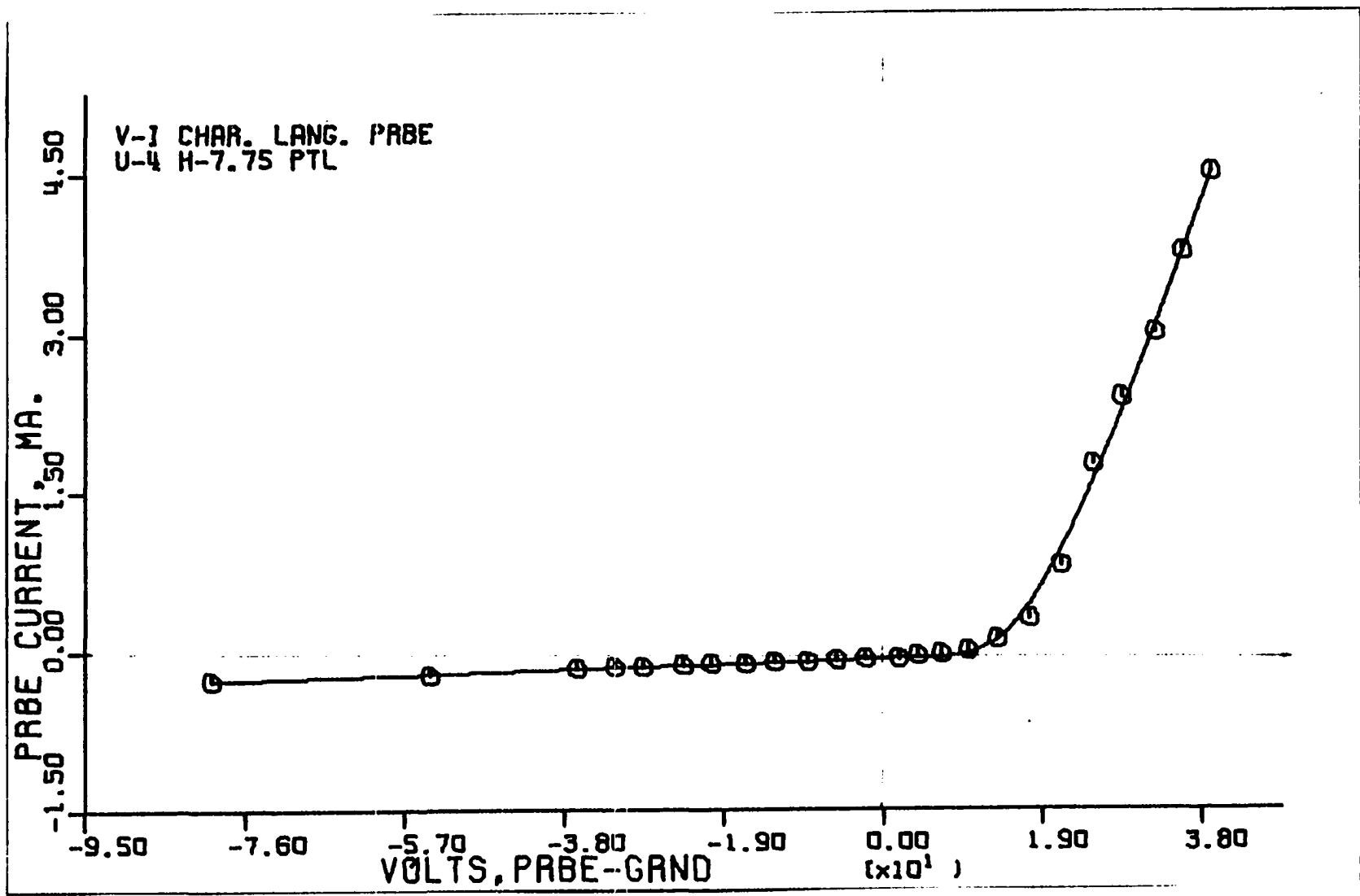


Figure 2.8c. Langmuir probe characteristics for the case I (with the floating cathode) with the probe tip located at $x = 10.52$ cm, $y = -2.44$ cm and $z = 1.27$ cm

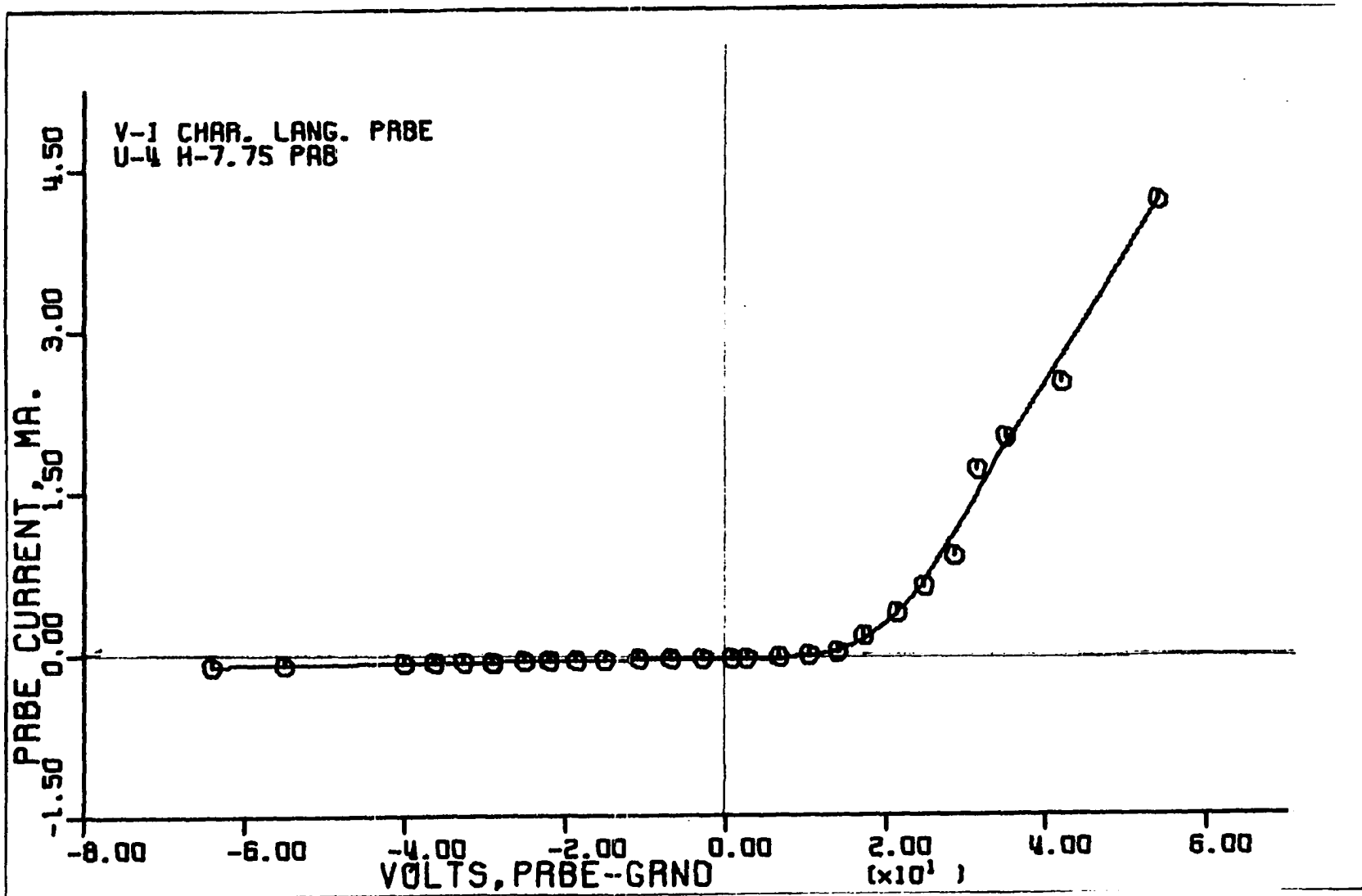
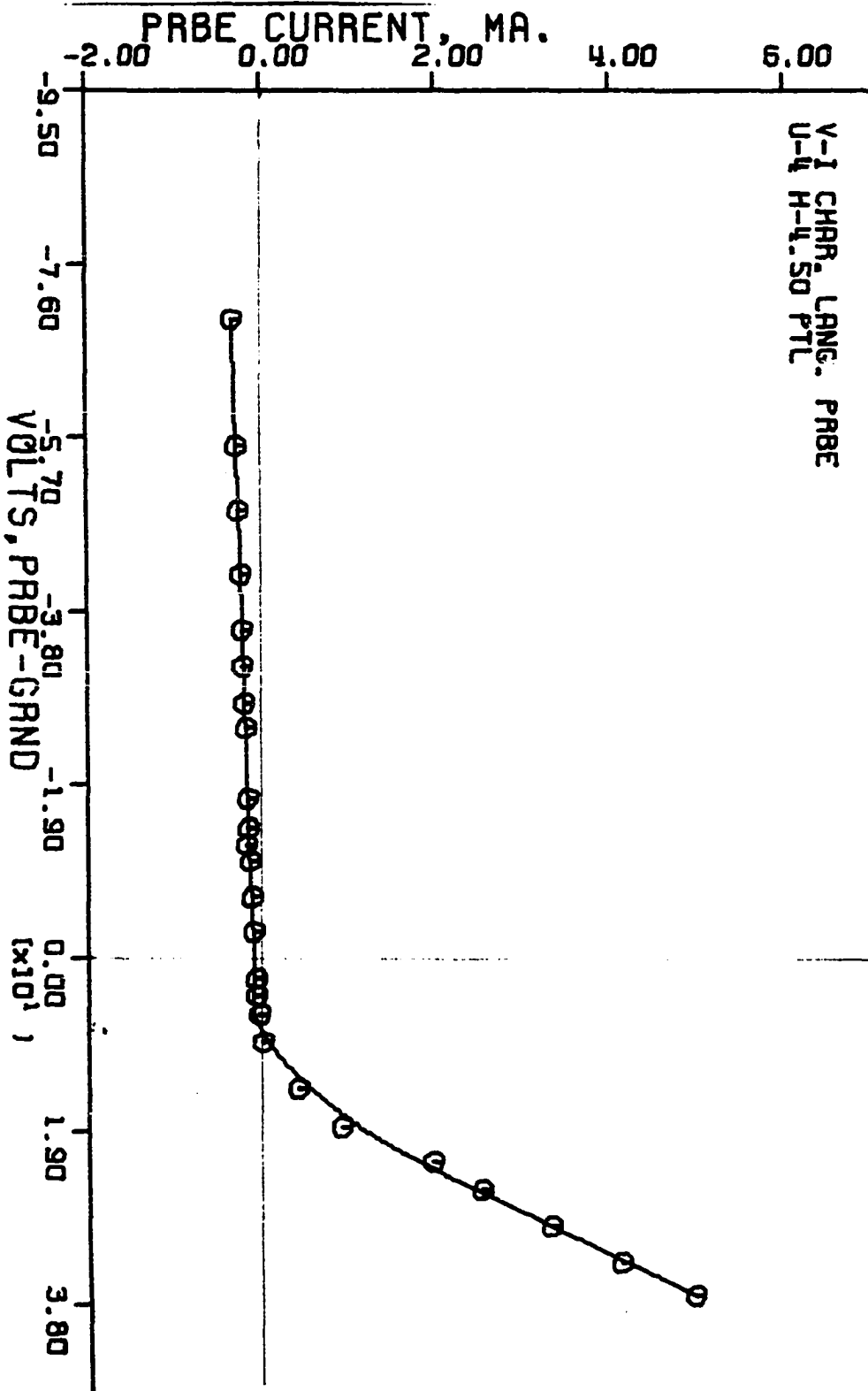


Figure 2.8d. Langmuir probe characteristics for the case I (with the floating cathode) with the probe tip located at $x = 4.45$ cm, $y = 0.0$ and $z = 11.43$ cm



cathode (case I), in Figure 2.9a,b,c,d for case of a grounded cathode (case II), and in Figures 2.10a,b,c,d for case of a biased cathode (case III).

These characteristic curves were obtained at a constant pressure inside the bell jar of 7.5×10^{-4} Torr and a constant magnetic field strength of 19 Oe (produced by a constant 4 A current in the Helmholtz coils), (see Figure 2.2b). In other words, the axial magnetic flux density was kept at 19 G.

A four-electrode cylindrical probe unit protrudes through the top plate of the bell jar in such a manner that the argon plasma can be sampled at a desired point by adjusting the depth and orientation of the probe.

The procedures used in taking the data for I-V characteristics are as follows:

1. Place the probe unit at the desired position.
2. Clean the electrode by applying a sufficiently high voltage to the probe.
3. Apply dc voltage to the probe at some desired value.
4. Record the probe ammeter and voltmeter readings.
5. Repeat above procedure to obtain the I-V characteristic.

A typical I-V characteristic is illustrated in Figure

Figure 2.9a. Langmuir probe characteristics for the case II (with the grounded cathode) with the probe tip located at $x = 1.17$ cm, $y = -0.48$ cm and $z = 1.27$ cm

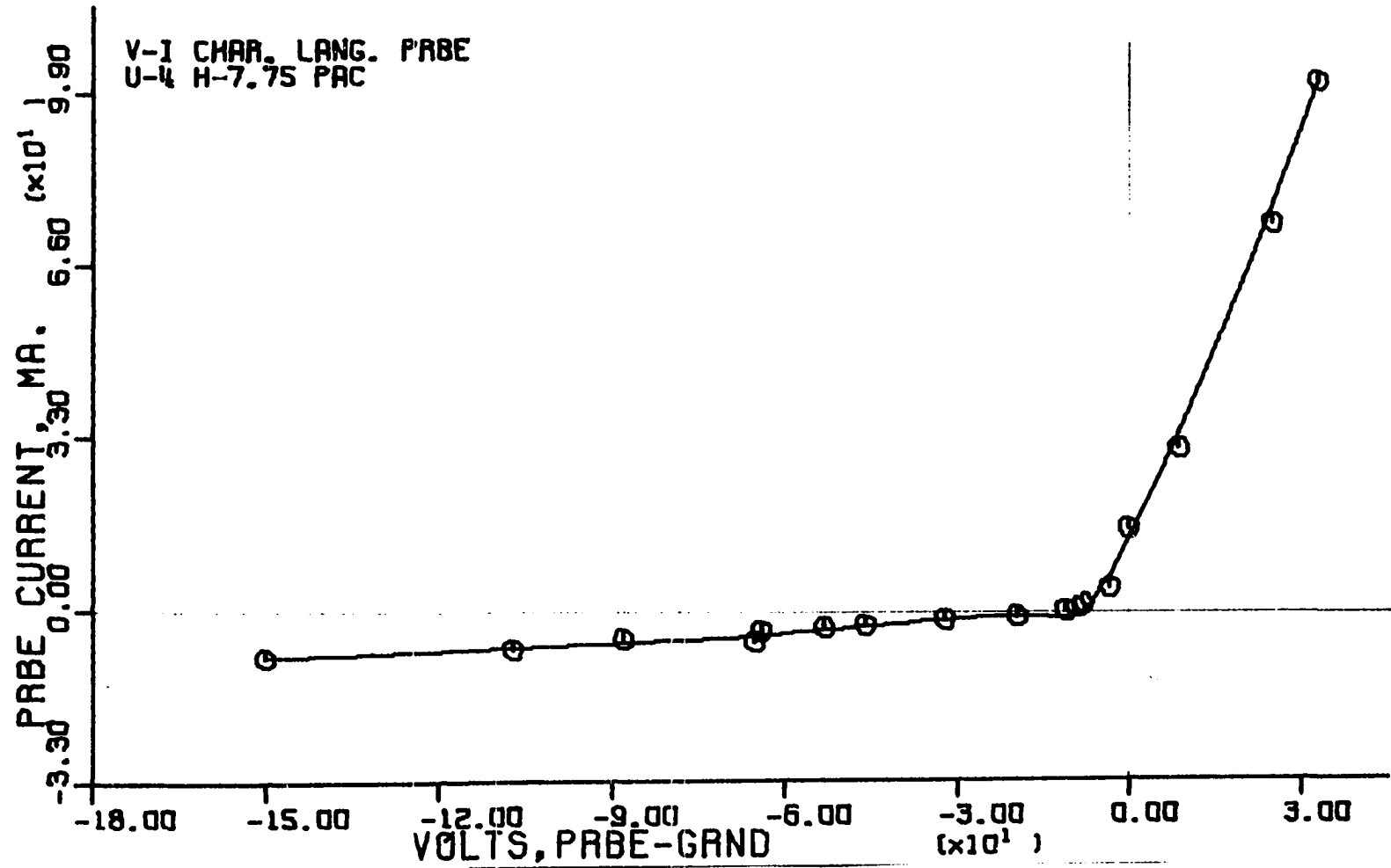


Figure 2.9b. Langmuir probe characteristics for the case II (with the grounded cathode) with the probe tip located at $x = 4.45$ cm, $y = 0.0$, and $z = 1.27$ cm

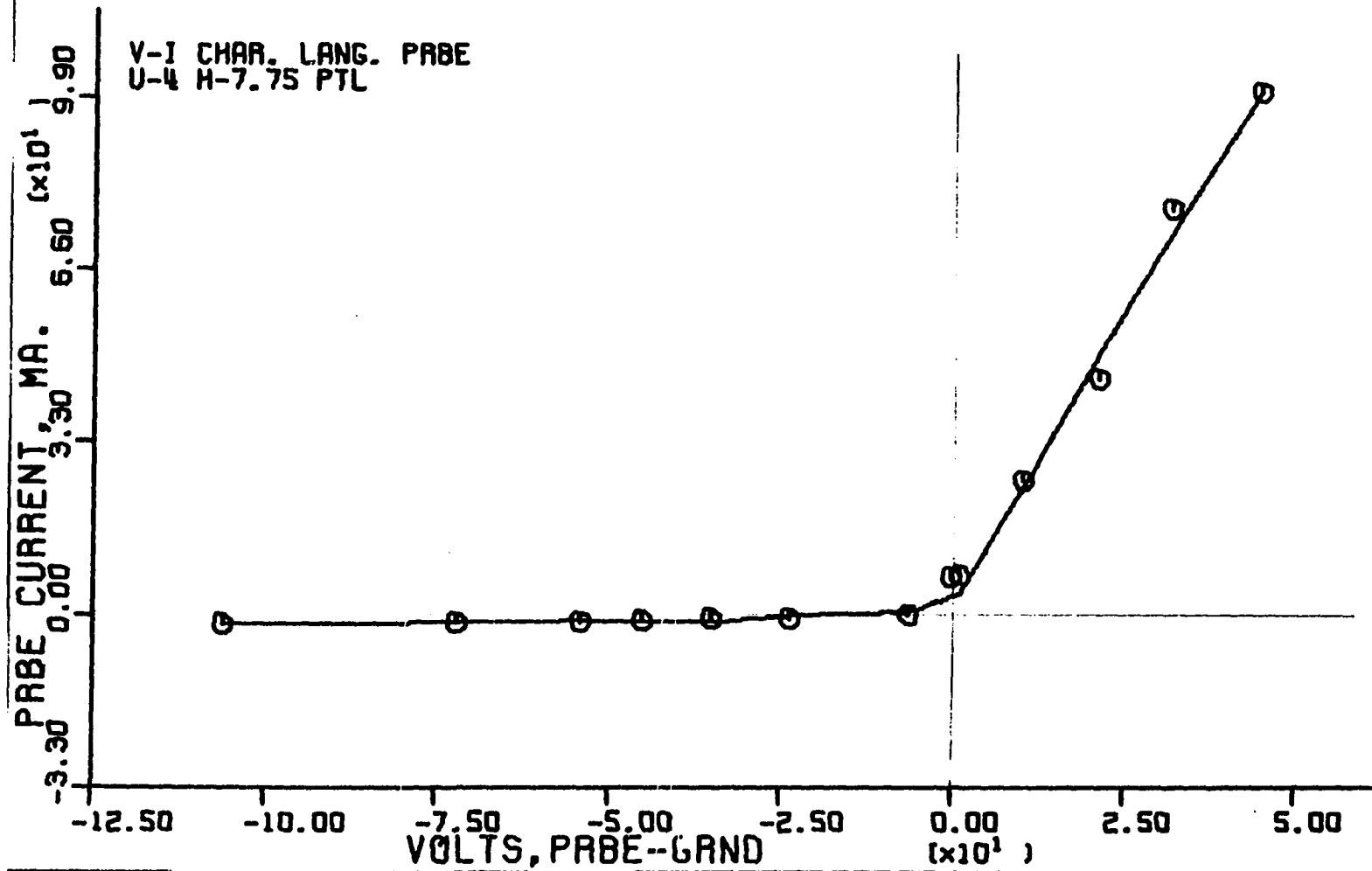


Figure 2.9c. Langmuir probe characteristics for the case II (with the grounded cathode) with the probe tip located at $x = 10.52$ cm, $y = -2.44$ cm and $z = 1.27$ cm

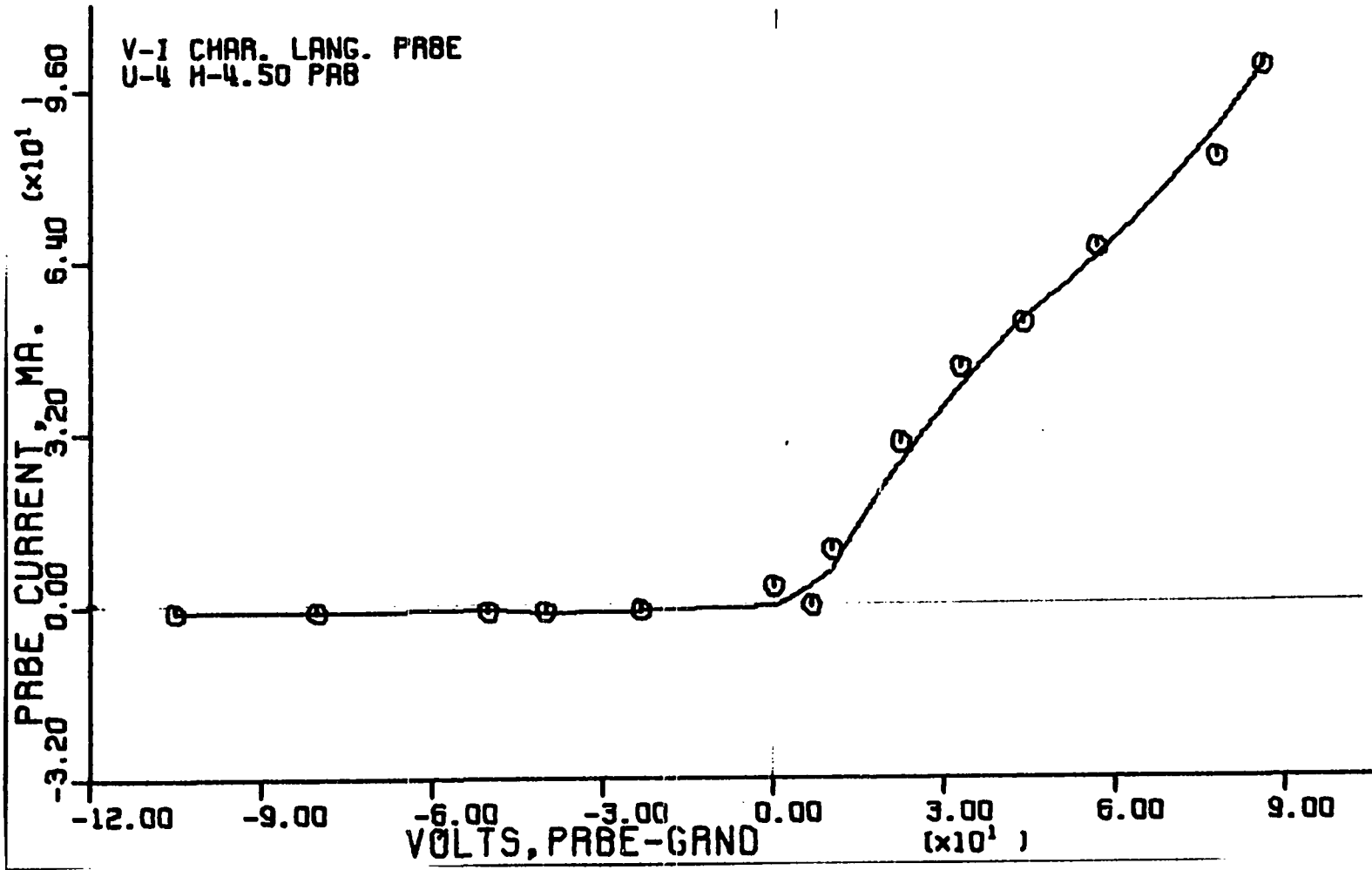


Figure 2.9d. Langmuir probe characteristics for the case II (with the grounded cathode) with the probe tip located at $x = 4.45$ cm, $y = 0.0$, and $z = 11.43$ cm

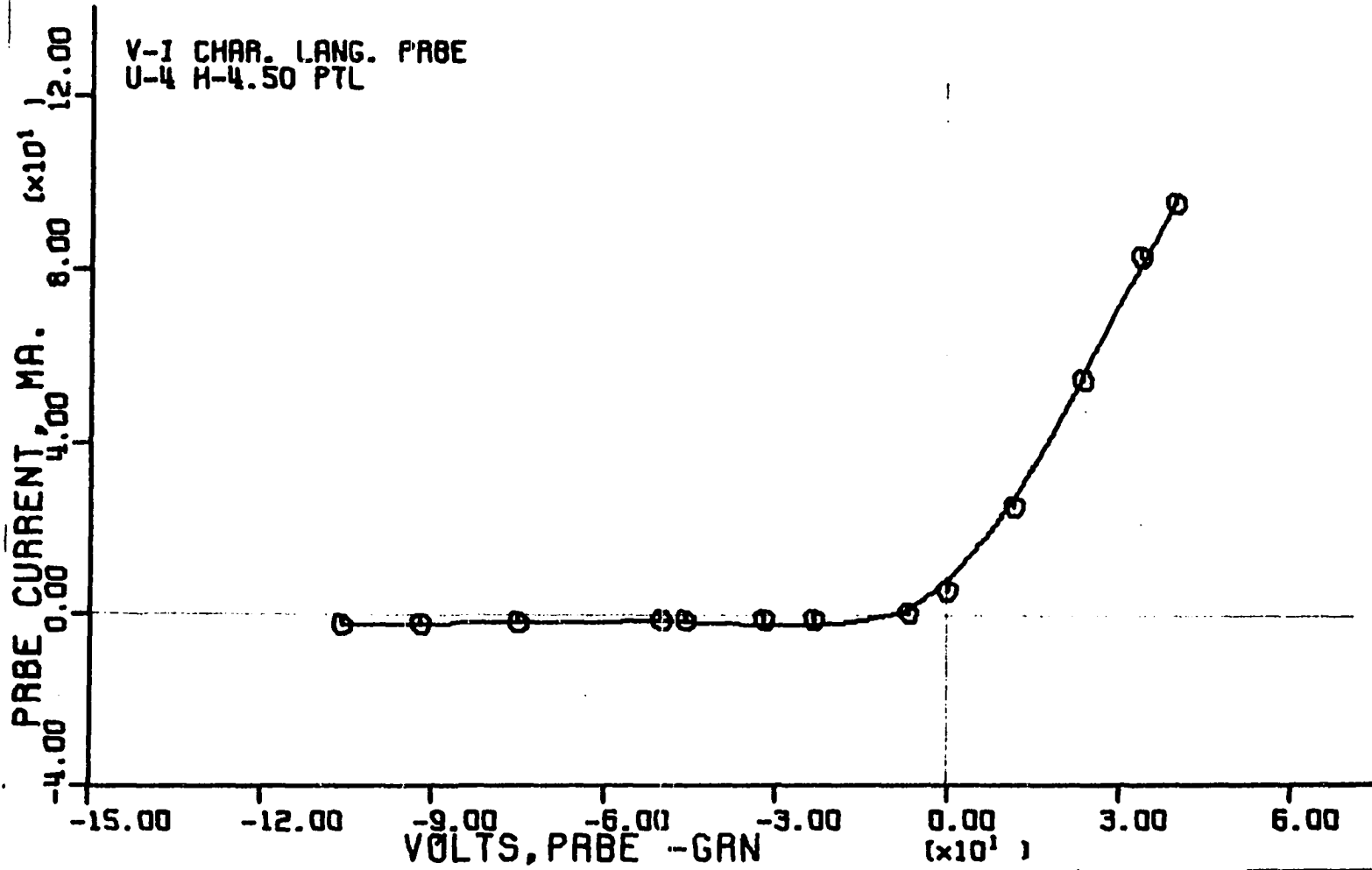


Figure 2.10a. Langmuir probe characteristics for the case III (with the biased cathode in sputtering condition). with the probe tip located at $x = 1.17$ cm, $y = -0.48$ cm and $z = 1.27$ cm

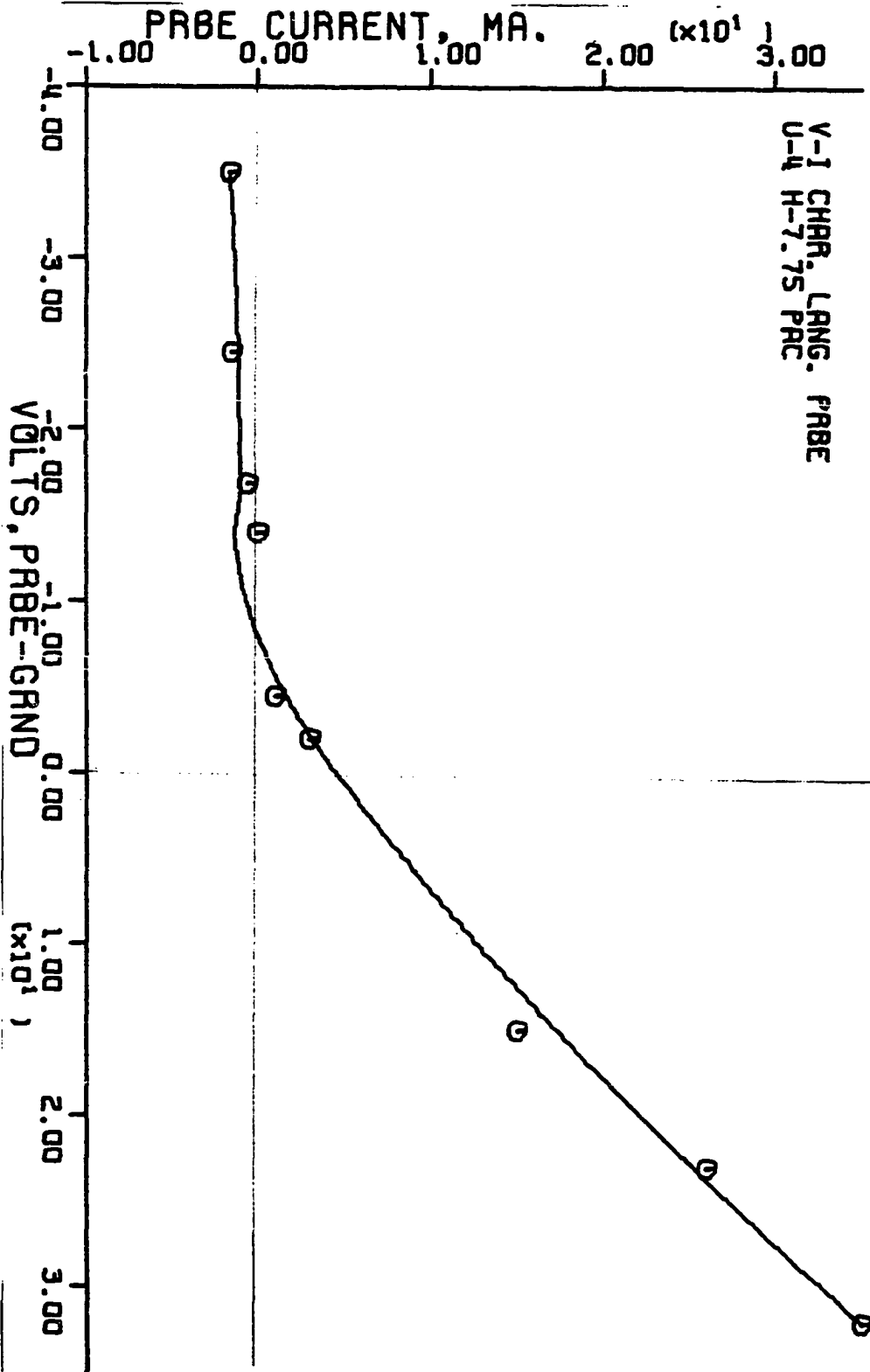


Figure 2.10b. Langmuir probe characteristics for the case III (with the biased cathode, in sputtering condition) with the probe tip located at $x = 4.45$ cm, $y = 0$ and $z = 1.27$ cm

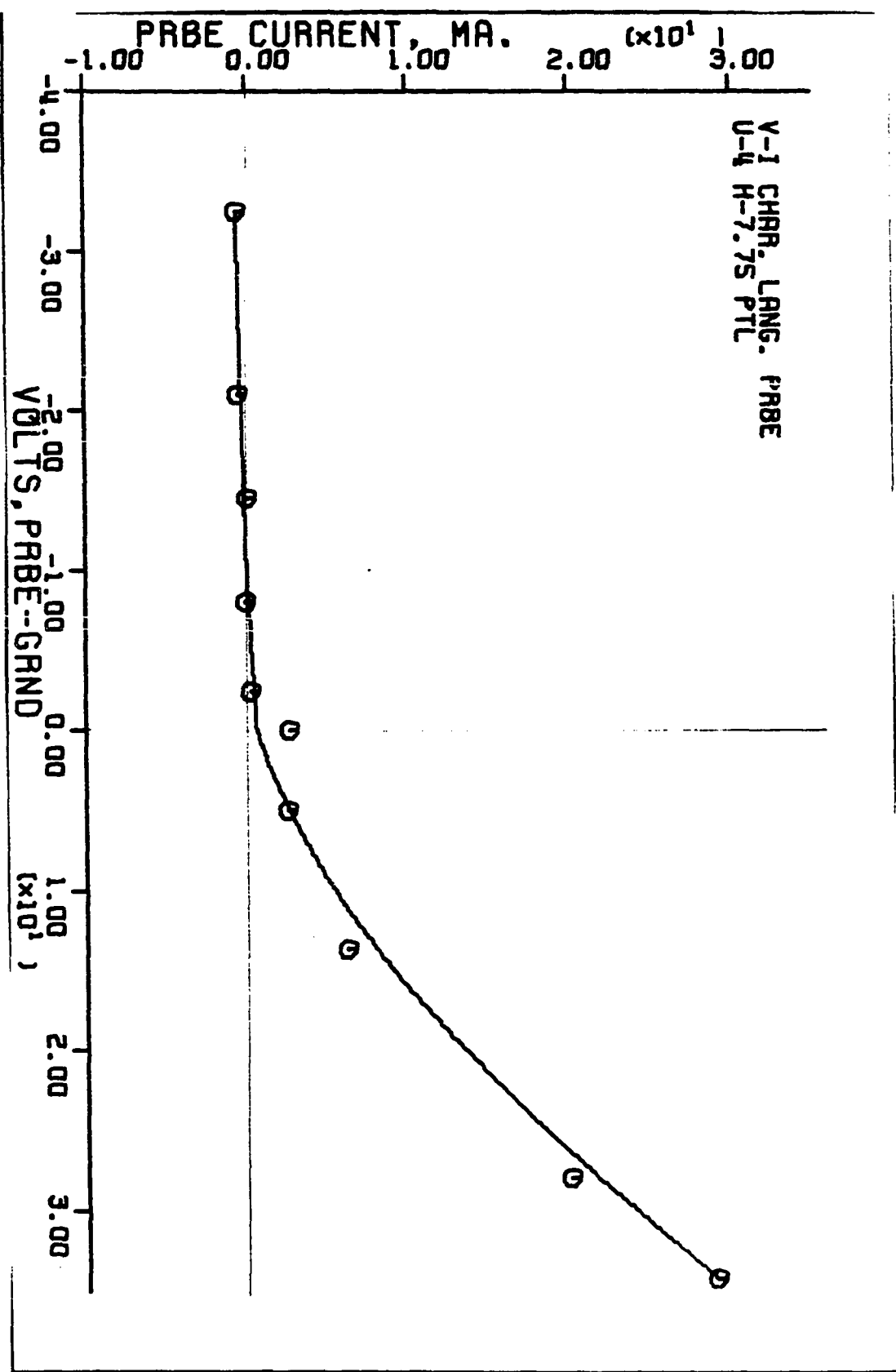


Figure 2.10c. Langmuir probe characteristics for the case III (with the biased cathode, in sputtering condition) with the probe tip located at $x = 1.17$ cm, $y = -0.48$ cm and $z = 11.43$ cm

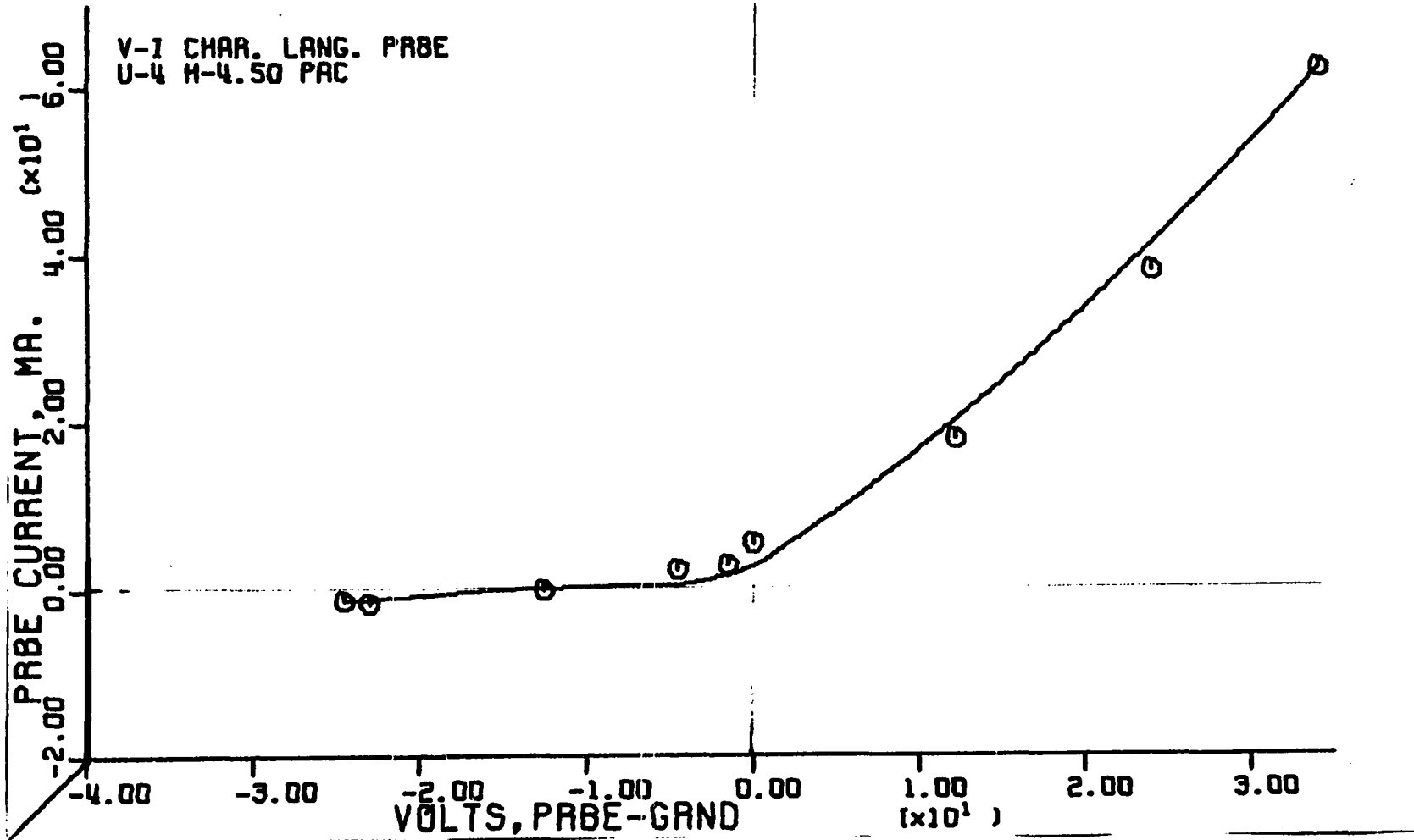
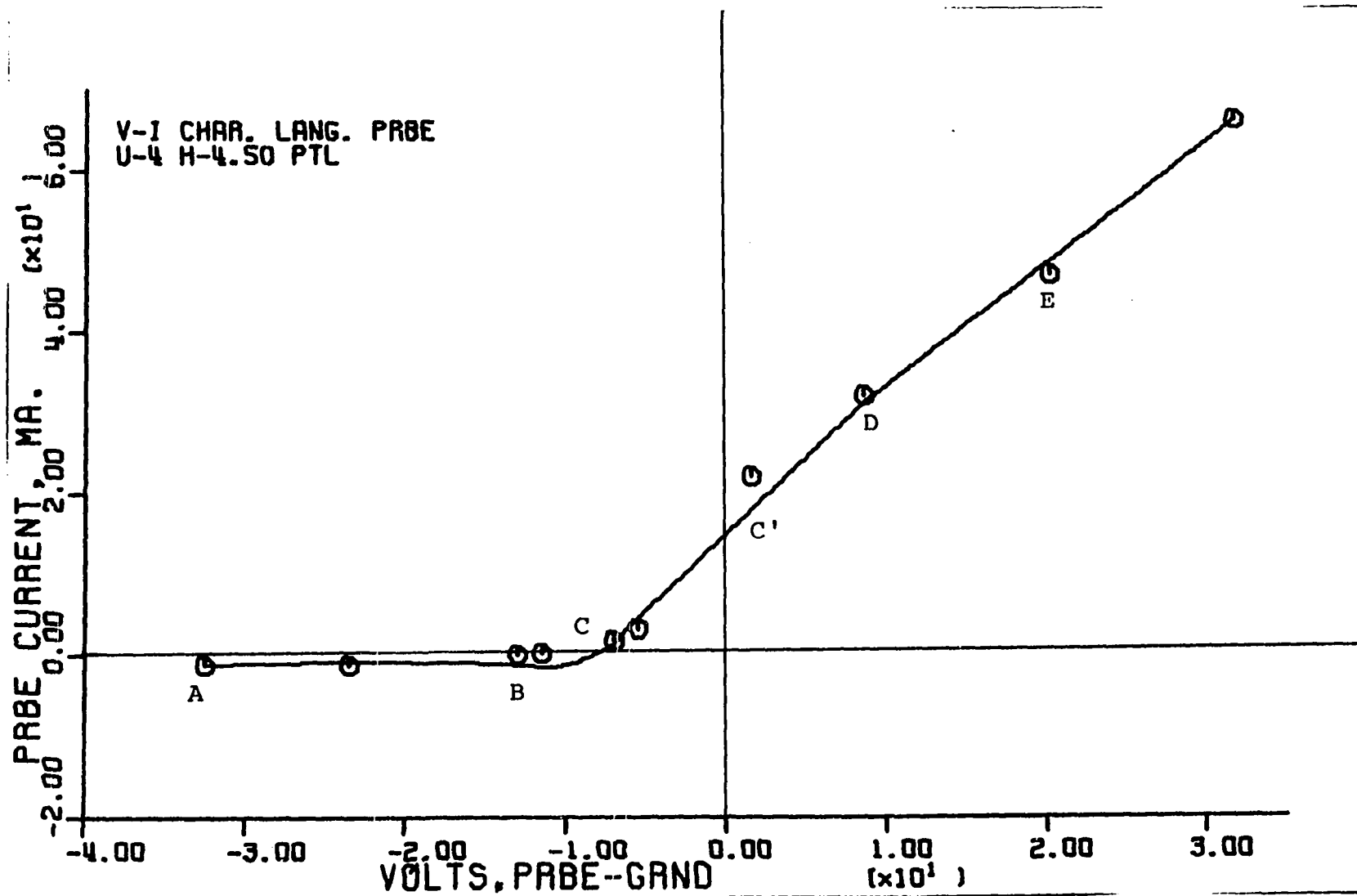


Figure 2.10d. Langmuir probe characteristics for the case III (with the biased cathode in sputtering condition) with the probe tip located at $x = 4.45$ cm, $y = 0$ and $z = 11.43$ cm



2.10d. In region AB, the probe is depressed to a large negative voltage with respect to the plasma. Most of the plasma electrons are repelled, and a positive-ion space charge is established adjacent to the probe surface, which tends to cause saturation of the ion current.

As the probe is made less negative, the operating point changes from B to C, and some of the higher-velocity electrons in the plasma begin to penetrate the space-charge sheath, causing a decrease in probe current. At operating point C, the probe collects equal numbers of ions and electrons. The potential at this point is known as the "wall potential", because it is the potential that an insulator would assume in the plasma. Due to the type of scaling used, it is difficult to observe the region around operating point D, but as the electron current increases, there will be a slight inflection in the curve at operating point (D) where the plasma or space potential (V_s) can be obtained. It should be noted that the behavior at the region near the inflection point (D) can be seen more clearly from the plot of $\ln(I_e)$ vs V . At this potential the probe receives the entire random currents due to both electrons and positive ions in the plasma. There is no space-charge sheath. The probe current is thus equal to the difference between the random electron current and the random ion current and is negative as a result of the very high electron mobility.

As the probe potential is made positive with respect to the space potential, the operating point changes from D to E, the ion current is decreased rapidly, and an electron space-charge sheath is formed.

The I-V characteristics of the Langmuir probe were obtained for the following special cases of interest:

1. "floating cathode" where no bias voltage is applied (case I),
2. "grounded cathode" where the cathode is shorted to the grounded anode (case II), and
3. "biased cathode" where negative dc potential is applied to the cathode (case III).

The characteristic curves are illustrated in Figure 2.8a, b,c,d for different probe positions for case I, in Figure 2.9a,b,c,d for case II, and in Figure 2.10a,b,c,d for case III. It should be noted that these figures have the same general shape although the voltage axes intercept (labeled as operating point C of Figure 2.10d) and the current axes intercept (labeled as operating point C' of Figure 2.10d) can be different from the case to the case. Since case II is a special case of case III, it is sufficient to consider the difference between case I and III.

It should be noted that the operating points labeled as C and C' on the I-V characteristics of the Langmuir probe have their special physical significance. The

voltage intercept (operating point C) represents a special point of interest, since at this operating point no net charge flow to the wall is to be expected (electron-current and ion current are equal), and in this case the wall is said to be at its floating potential, V_W . The operating point C is where an insulated wall potential will be different from the plasma potential.

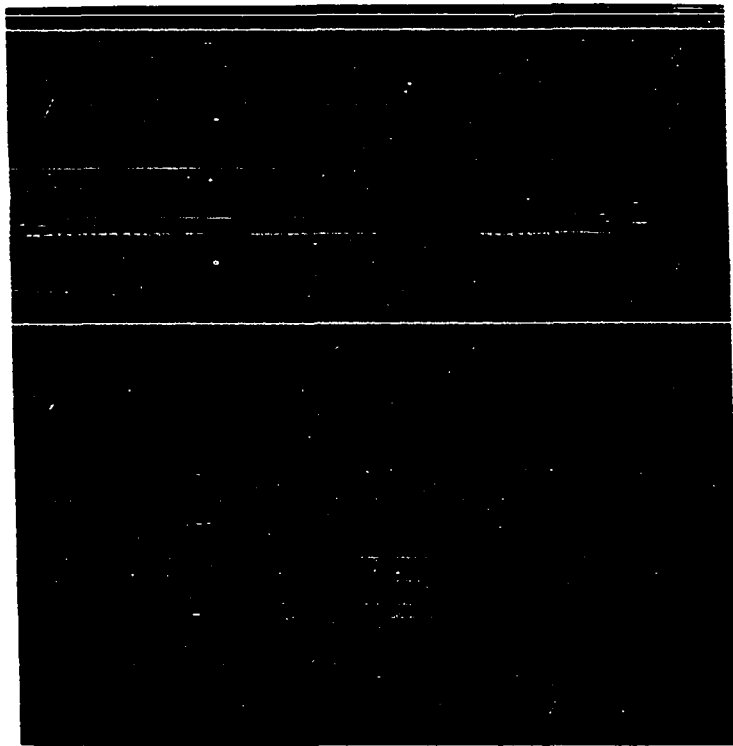
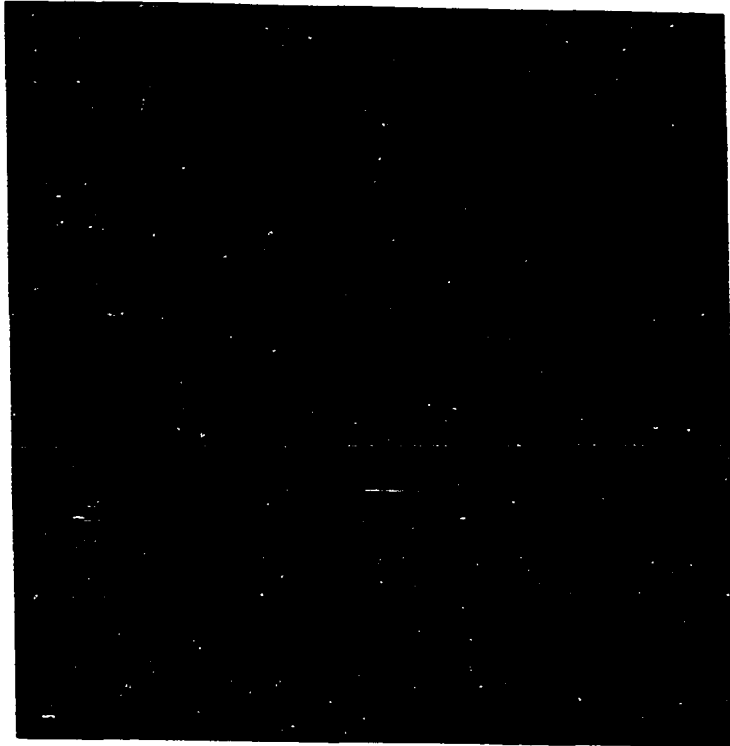
The current intercept (operating point C') is also a point of special interest. At this operating point, the wall potential is equal to the plasma potential, so that the probe potential is equal to zero and a net current flow is observed. Note that the electron current is plotted on the positive axes.

A comparison of the I-V characteristics obtained for cases I and III, shows that the appearance and the shape of the characteristic curves shown in figure 2.8 for case I are essentially the same as those shown in Fig. 2.10 for case III, with two exceptions: (a) The voltage intercept (operating point C) for the case I has a positive wall potential, $V_W > 0$, while that for case III has a negative wall potential, $V_W < 0$. This shift in wall potential from positive to negative is to be expected since the cathode and its vicinity are made to become negative with the applied dc bias potential. (b) The current intercept

(operating point C') of case I is negative while that for the case III is positive. This implies that the net current flowing to the surface area of the Langmuir probe is dominated by the ion current in case I, whereas the net current flow to the surface area of the Langmuir probe is dominated by the electron current in case III. It should also be noted that for the same probe voltage, the probe current measured for case III is about one order of magnitude greater than that measured for case I (compare Figure 2.8d with Figure 2.10d). This is to be expected since the bias electric field tends to accelerate the charged particle so that increases in current density occur. It is interesting to note also that, under the sputtering condition, the glow pattern of the plasma changes with the biased voltage applied to the cathode: the intensity of glow increases with the biased voltage applied to the cathode. This is illustrated in Figure 2.11a,b. Figure 2.11a shows the glow pattern for the case when -400 V (dc) is applied to the cathode, while Figure 2.11b shows the glow pattern for the case when -500 V (dc) is applied to the cathode. In both cases the probe current was measured to be 250 MA (dc). Furthermore, the nonuniformity in the intensity of glow is noted in Figure 2.11a,b. However, this nonuniformity tends to disappear as the bias voltage is removed, i.e., for the case of nonsputtering. This phenomenon is primarily

Figure 2.11a. Plasma glow pattern under the sputtering condition for $V_{AG} = -400, V$ (dc)

Figure 2.11b. Plasma glow pattern under the sputtering condition for $V_{AG} = -500, V$ (dc)



due to the nonuniformity of the magnetic field configuration superimposed on the dc bias field in the vicinity of the end of the center-rod cathode. Since the center-rod cathode is made of an iron material which has a high permeability, when it is imbedded in a uniform static magnetic field produced by a Helmholtz coil, the presence of the rod perturbs the field in the region near the rod to produce a complicated field configuration. The charged particle behavior in the vicinity of the rod will be greatly influenced by these nonuniform static electric and magnetic fields to produce the observed glow pattern. To determine the exact distribution of the fields, a complicated boundary value problem must be solved. This is not attempted in the present study.

5. Information derived from experimental measurements

From the I-V characteristics curve obtained, plasma parameters such as the electron temperature T_e , the electron number density n_e , the electron thermal velocity v_e , and the degree of ionization can be determined. The electron temperature can be determined from Equation (2.3), which is the slope of the tangent line to the plot of $\ln(I)$ vs V , and when the value of T_e is known, the electron thermal velocity can be determined. Furthermore, if the electron temperature is known and the electron current

specified, the electron number density can be determined from Equation (2.5). The determination of these plasma parameters is illustrated for case I, where no biased voltage is applied to the cathode, in the following example.

Equation (2.3) can be expressed approximately as

$$\frac{d}{dV}[\ln(I)] = \frac{e}{KT} = [\ln(I_2/I_1)]/(V_2-V_1) \quad (2.7)$$

where the Boltzmann constant $K = 1.38 \times 10^{-23}$ Joules/°K, and the electronic charge $e = 1.6 \times 10^{-19}$ c. From Figure 2.8b, at $V_1 = 19$ V, $I_1 = 0.64$ mA and at $V_2 = 24$ V, $I_2 = 1.35$ mA, so that $T = 77,700$ °K since $e/K = 11,600$ c °K/Joule. Under thermal equilibrium conditions, the Maxwell-Boltzmann velocity distribution may be assumed so that the average random speed of electron \bar{v}_e is given by $(8KT/\pi m_e)^{1/2}$ since $\bar{v}_e = v_{pr}^2/\sqrt{\pi}$, where $v_{pr} = [2KT/m]^{1/2}$ is the most probable velocity. Since the electronic mass $m_e = 9.11 \times 10^{-31}$ kg for $T_e = 77,700$ °K, the average random speed of an electron is estimated to be $\bar{v}_e = 1.73 \times 10^6$ m/sec. The probe area over which the charged particles are intercepted A is estimated to be 2.28×10^{-2} cm², and $e = 1.6 \times 10^{-19}$ c, so that Equation (2.5) yields $n_e = 6.77 \times 10^9$ cm⁻³.

On the other hand, the degree of ionization,

$\alpha = (n_e/N)$, where N is the atom number density, in cm^{-3} , can be estimated as follows: if the ideal gas law $p = NKT$, is assumed to be applicable to the argon gas under study, and the gas pressure p , in dyne/cm^2 , and the gas temperature T , in $^\circ\text{K}$, are known, the value of N can be estimated so that α can be calculated. For example, with $T = 703 \text{ }^\circ\text{K}$, and $p = 7.5 \times 10^{-4} \text{ Torr}$ it is estimated that $N = 1.03 \times 10^{13} \text{ cm}^{-3}$. Consequently, the degree of ionization is estimated to be $\alpha = 0.066\%$.

With regard to the degree of ionization of an ionized gas, there is a relationship given by well known Saha's Equation (62). However, this relationship cannot be applied for the argon plasma under investigation because the temperature of the argon plasma and the pressure of the argon gas are not in the proper range. Saha's Equation is applicable for argon plasmas in which the gas temperature is in the range of $5,000 \text{ }^\circ\text{K}$ to $20,000 \text{ }^\circ\text{K}$ and the pressure is above 10 atm (63).

The plasma parameters T_e , n_e , \bar{v}_e and the degree of ionization α determined by the method illustrated above for case I, are tabulated in Table 1 for different probe positions, $P(x,y,z)$ in the Cartesian coordinate system, as indicated in Figure A-1 of the Appendix. Similarly, these parameters for case III are shown in Table 2.

Table 1. The values of electron temperature, T_e , the electron number density, n_e , electron mean velocity \bar{v}_e and the degree of ionization, α , interpreted from the Langmuir probe measurement for the case I, at various probe tip positions

Case I		a	b	c	d
Probe Tip Position	x (cm)	1.17	4.45	10.52	4.45
	y (cm)	-0.48	0.00	-2.44	0.00
	z (cm)	1.27	1.27	1.27	11.43
n_e (cm ⁻³)		7.22×10^9	6.77×10^9	3.95×10^9	8.58×10^9
T_e (°K)		10.51×10^4	7.77×10^4	6.52×10^4	10.48×10^4
\bar{v}_e (cm/sec)		2.01×10^8	1.73×10^8	1.59×10^8	2.01×10^8
α (%)		7.01×10^{-2}	6.57×10^{-2}	3.83×10^{-2}	8.33×10^{-2}

Table 2. The values of electron temperature, T_e , the electron number density, n_e , electron mean velocity \bar{v}_e and the degree of ionization, α , interpreted from the Langmuir probe measurement for the case III (biased cathode) at various probe tip positions

CASE III		a	b	c	d
Probe Tip Position	x (cm)	1.17	4.45	1.17	4.45
	y (cm)	-0.48	0.00	-0.48	0.00
	z (cm)	1.27	1.27	11.43	11.43
n_e (cm^{-3})		7.27×10^{10}	5.96×10^{10}	12.21×10^{10}	14.84×10^{10}
T_e ($^{\circ}\text{K}$)		35.45×10^4	17.26×10^4	22.55×10^4	36.90×10^4
\bar{v}_e (cm/sec)		3.70×10^8	2.58×10^8	2.95×10^8	3.77×10^8
α (%)		7.06×10^{-1}	5.79×10^{-1}	11.85×10^{-1}	14.85×10^{-1}

C. Measurement of rf Power Supplied to the Sputtering System

A schematic diagram representing the electrical network used in the instrumentation for the rf power measurement is shown in Figure 2.12a,b. The block diagram in Figure 2.12a shows the case for rf power monitoring in the vicinity of the rf excitation loop and the bell jar. The block diagram shown in Figure 2.12b is for the case where the rf power meter is located about 112 in. away from the rf excitation loop.

It was noted that when the rf power meter was located near the rf loop, as in Figure 2.12a, it was very difficult to obtain accurate readings due to fluctuations of the meter needle. This condition was a result of the rf power meter being located in an area where the strong influence of Helmholtz coil field and the rf electromagnetic field, produced by the rf loop antenna, are present. These electromagnetic fields interfere with the internal mechanism of the rf power meter and cause erroneous readings. To avoid this difficulty, the rf power meter was moved away from the bell jar region so that the undesired interference could be minimized, as shown in Figure 2.12b.

Particular attention was given to case I, in which no bias voltage was applied externally to the center-rod cathode. The results of the measurements for this case

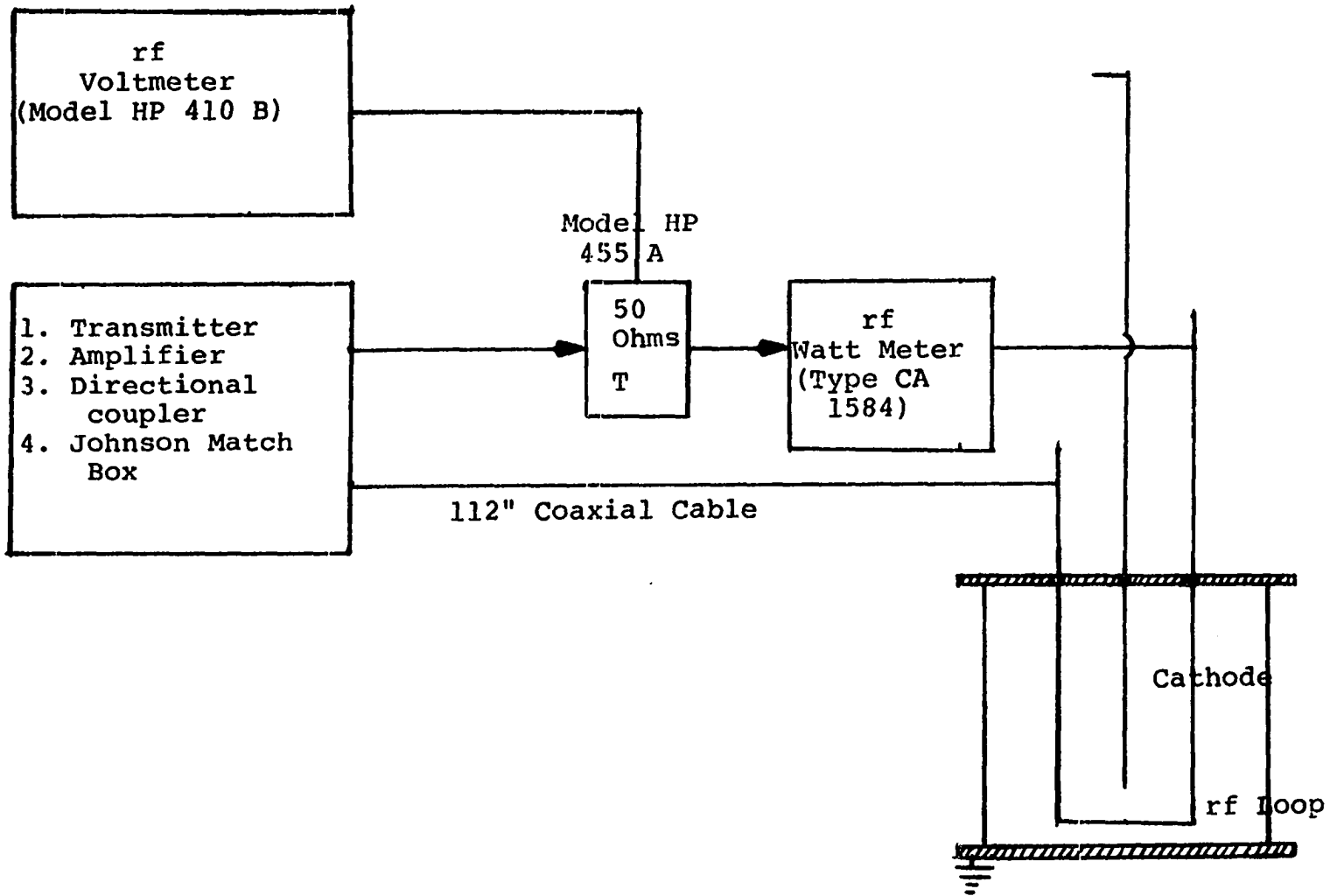


Figure 2.12a. Schematic diagram showing electrical network for rf power measurement for the case when rf power meter is located near the rf loop

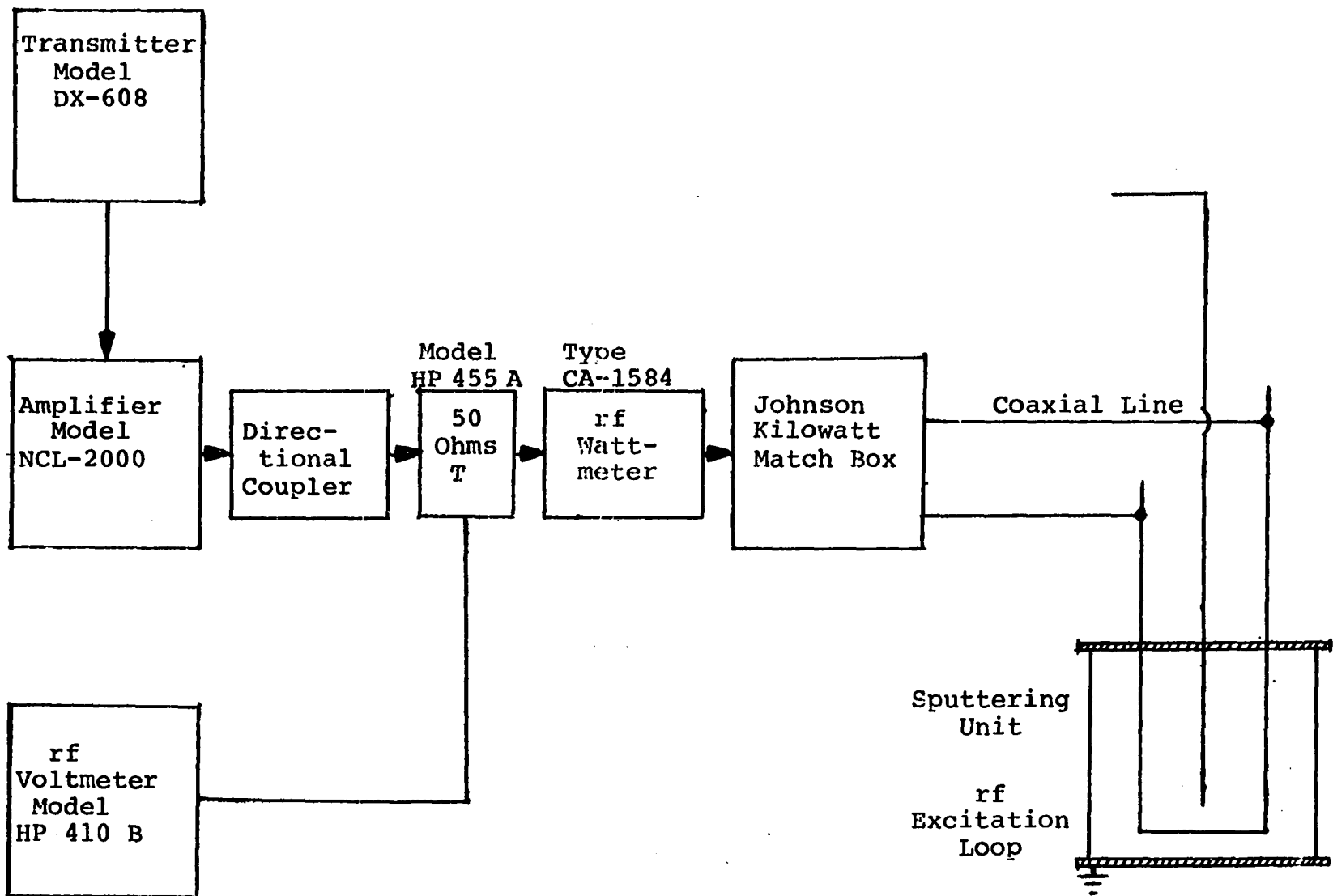


Figure 2.12b. Schematic diagram showing electrical network for rf power measurement for the case when rf power meter is placed away from the rf loop

are shown in Table 3, where an asterisk indicates which readings were taken with the set-up shown in Figure 2.12b.

The table contains two sets of data, one for the case of preionization, when the argon plasma was not yet formed, and the other for the case where the argon plasma is present. It should be noted that for the first case the rf excitation loop is radiating in an environment of unionized gas, in which the displacement current density plays an important role, in energy storage while in the second case the rf excitation loop is radiating in an environment of weakly ionized gas, in which the conduction current density plays an important role in energy absorption.

D. Some Remarks on the Measurement Techniques and Sources of Error

In order to maximize the degree of accuracy of various measurements, special attention was given to the following: the careful design of the Langmuir probe, the shielding of the measuring apparatus from undesired signals, the design of the rf filter, the proper interpretation of the I-V characteristics obtained, and the proper location of the rf power meter.

For example, certain design criterion for the Langmuir probe had to be met. The probe unit size had to be small

Table 3. Radio frequency power flow measurements

	Amplifier plate- current (Amp)	Amplif. plate- voltage (volts)	Match box S.W.R. reading	dc magnetic field (Oersted)	Forward power flow (watts)	Reverse power flow (watts)	Absorb power (watts)	Trans. line voltage (volts)
Without argon plasma	320	1600	2.7	19	490	385	105	410
	380*	1600*	2.5*	19*	400*	40*	360*	190*
With argon plasma present	320	1600	2.7	19	375	330	45	410
	380*	1600*	2.5*	19*	400*	35*	365*	190*

so that it would not cause too much disturbance of the plasma under investigation. The surface area of the probe that was exposed to the plasma had to be large enough to intercept the charged particle flux, but small enough not to cause perturbation of the plasma. The electrodes were cleaned with a large negative or a large positive voltage before the measurement was taken and recorded.

Perhaps the most difficult task during the course of experimental measurement was the elimination of the influence of the rf signal upon the dc measuring apparatus. It was necessary to put the measuring apparatus inside the metal cabinet enclosure shown in Figure 2.6b, and use a long coaxial cable to minimize the effect of rf energy coupling and energy coupling due to the dc magnetic field produced by the Helmholtz coils. The fluctuation in the needles of the measuring meters was reduced significantly in this manner. An improvement was also made by use of rf filters designed for minimum impedance. The filter circuit was placed in parallel with the measuring apparatus, as shown in Figure 2.6b. With these arrangements, the fluctuations in the meter needles were practically eliminated.

In estimating the electron temperature from the slope of the plot $\ln(I_e)$ vs V , it should be noted that a small error in reading the value of the slope can lead to a large error in the value of the

temperature.

As for the rf power measurement, particular care should be given to the location of the rf power meter, since the power meter is an electromechanical device, which undoubtedly would respond to the influence of the strong electromagnetic fields produced by the rf loop or the Helmholtz coil. With the arrangement shown in Figure 2.12b, the influence of electromagnetic fields on the rf power meter was minimized, and satisfactory readings of power flow were obtained.

In addition to the measurement techniques discussed above, the quality of the instruments used in this experimental study certainly played an important part in obtaining accurate information. For example, when the data for the I-V characteristics curve was being taken, the loading effect on the meter was noticeable in some cases.

III. THEORETICAL ANALYSIS

A. Basic Equations Governing the Interaction of Electromagnetic Fields with Plasma

It is well known that there are two theoretical approaches frequently used in describing the behavior of the charged particles in a plasma subjected to the influence of externally applied electromagnetic fields. One approach uses Boltzmann's equation, based on the microscopic kinetic theory of plasma, in which particle velocity distribution is properly taken into account. The other approach uses the Langevin Equation, based on macroscopic, magnetohydrodynamic theory, in which the plasma is regarded as a conducting fluid. In the first approach (64-69), one can conveniently describe the state of a system of particles with the aid of one particle distribution function $F_s(\vec{r}, \vec{v}, t)$ (64) where \vec{r} is a position vector and \vec{v} is the velocity vector of the particle at time t . The subscript s denotes the type of charged particle under consideration. For example, s becomes e for the electron and i for the ion. The interpretation of $F(\vec{r}, \vec{v}, t)$ is such that $F(\vec{r}, \vec{v}, t) d\vec{r} d\vec{v}$ is the number of particles in a volume element $d\vec{r} d\vec{v}$ in the phase space, and the equation of which $F(\vec{r}, \vec{v}, t)$ is the solution is known as Boltzmann's Equation. The latter equation, for the particle of mass m_s , and electric charge q_s can be written as

$$\frac{\partial F_s}{\partial t} + \vec{v} \cdot \nabla_r F_s + \frac{q_s}{m_s} [\vec{E} + \vec{v} \times \vec{B}] \cdot \nabla_v F_s = \left(\frac{\partial F}{\partial t} \right)_{\text{coll}} \quad (3.1)$$

where ∇_r and ∇_v are the del operators in coordinate phase space and velocity phase space, respectively.

The term on the right-hand side takes into consideration only the collision effect, namely, the collisions which modify charged particle distribution by interaction with other charged and neutral particles. Basically, encountering each other at distances less than the Debye length of the plasma will interact via the term $\left(\frac{\partial F}{\partial t} \right)_{\text{coll}}$.

If $F(\vec{r}, \vec{v}, t)$ is known, then one can find the average of any instantaneous physical property $\phi(\vec{r}, \vec{v}, t)$ of the system in the following manner

$$\langle \phi_i \rangle = \frac{1}{n(\vec{r}, t)} \int F(\vec{r}, \vec{v}, t) \phi_i(\vec{r}, \vec{v}, t) dv \quad (3.2)$$

and

$$n(\vec{r}, t) = \int F(\vec{r}, \vec{v}, t) dv \quad (3.3)$$

It should be noted that $\langle \phi_i \rangle$ is still a function of \vec{r} and t in Equation 3.2. Since one averages over the velocity distribution of the plasma, the n given in Equation 3.3 must be interpreted as the instantaneous particle density.

For example, the convection current density $J_s(\vec{r}, t)$ and the charge density $\rho_s(\vec{r}, t)$ can be expressed in terms of the distribution function $F_s(\vec{r}, \vec{v}, t)$ as follows:

$$\vec{J}_s(\vec{r}, t) = q_s \int \vec{v} F_s(\vec{r}, \vec{v}, t) d\vec{v} \quad (3.4)$$

and

$$\rho_s(\vec{r}, t) = q_s \int F_s(\vec{r}, \vec{v}, t) d\vec{v} \quad (3.5)$$

where q_s is the electric charge of the s^{th} species particle. For example, $q_e = -e$ and $q_i = +e$ are the electronic charge and positive ion charge, respectively where e is taken as a positive quantity.

In order to solve the Boltzmann's Equation (3.1) for the distribution function $F(\vec{r}, \vec{v}, t)$, the collision model must be specified, and the electromagnetic fields \vec{E} and \vec{B} must be known. On the other hand, the electromagnetic fields in the plasma are governed by Maxwell's field equations, which can be expressed as follows:

$$\nabla \times \vec{H} = \vec{J} + \epsilon_0 \frac{\partial \vec{E}}{\partial t} \quad (3.6)$$

$$\nabla \times \vec{E} = -\mu_0 \frac{\partial \vec{H}}{\partial t} \quad (3.7)$$

$$\nabla \cdot \vec{B} = 0 \quad (3.8)$$

$$\nabla \cdot \vec{D} = \rho \quad (3.9)$$

Where the magnetic field intensity \vec{H} , in A/m, and the magnetic flux density \vec{B} , in Wb/m², are related by

$$\vec{B} = \mu_0 \vec{H} \quad (3.10)$$

and the electric field intensity \vec{E} , in V/m, and the electric flux density, \vec{D} , in C/m², are related by

$$\vec{D} = \epsilon_0 \vec{E} \quad (3.11)$$

in which ϵ_0 and μ_0 denote, respectively, the dielectric constant and to permeability of vacuum.

It should be noted that Equation 3.6 expresses the Ampere's law, with Maxwell's displacement current taken into account, Equation (3.7) expresses the Faraday's law of induction and Equations 3.8 and 3.9 express the Gauss law.

The space-charge density ρ , and the convection current density J , when the contribution of both electron and positive ions are significant, are given by

$$\rho = \sum_s \rho_s = e(n_i - n_e) \quad (3.12)$$

and

$$\vec{J} = \sum_s \vec{J}_s = \vec{J}_i + \vec{J}_e \quad (3.13)$$

It should be noted also that the current density J , in A/m and the space-charge density ρ , in C/m³, are related by the continuity equation, expressing the idea of the conservation of charge:

$$\nabla \cdot \vec{J}_s + \frac{\partial \rho_s}{\partial t} = 0 \quad (3.14)$$

It should be observed that since the distribution function $\vec{F}(\vec{r}, \vec{v}, t)$ is a function of the electromagnetic fields \vec{E} and \vec{H} through Boltzmann's Equation (3.1), while the electro-

magnetic fields \vec{E} and \vec{H} are the functions of the current density \vec{J} via the Maxwell's curl Equation (3.6), and the current density \vec{J} is also the function of $F(\vec{r}, \vec{v}, t)$, the complete solution of the interaction problem involves the solution of the coupled Boltzmann-Maxwell Equations.

The latter equation is a partial-differential-integral equation, which is very difficult to solve. The solution of this problem has been attempted by various authors but has been only partially successful. Many workers have applied this approach in investigating some simplified physical situations with series of approximations in order to reduce the mathematical complexity. Consequently, the solution has been obtained only for some special cases. It appears that the complete general solution of this problem has not yet been found even after the extensive research work carried out by many able researchers in plasma physics over the past half century.

The second approach, which is somewhat less rigorous but more easily solved, uses the Langevin Equation, as shown in Equation 3.15, to describe the motion of the average charged particle:

$$\frac{d\vec{u}_s}{dt} + \nu\vec{u}_s = \frac{q_s}{m_s}[\vec{E} + \vec{u}_s \times \vec{B}] \quad (3.15)$$

and

$$\vec{J} = \sum_s q_s n_s \vec{u}_s \quad (3.16)$$

where \vec{u}_s denotes the velocity of the average charge particle, and ν is responsible for viscous damping and is related to the average momentum-transfer collision frequency of the charged particle with the other constituents of the plasma.

The Langevin Equation 3.15 and Equation 3.16 are often used in conjunction with Maxwell's Equations to describe the dynamics of the plasma. The restrictions and assumptions which are inherent in the usage of Equation 3.15 rather than Equation 3.1 have been discussed by several authors (70-72) and will not be considered here. However, it should be pointed out that the use of Equations 3.15 and 3.16 leads to an expression for the current density which is reasonably accurate for many physical situations.

Equations 3.15 and 3.16 can be solved for current density in terms of the plasma parameters and the electromagnetic fields so that

$$\vec{J} = \overleftrightarrow{\sigma} \cdot \vec{E} \quad (3.17)$$

where $\overleftrightarrow{\sigma}$ is the conductivity tensor of the magnetoplasma. The elements of this tensor are, in general, a function of plasma parameters such as the collision frequency ν , the angular frequency of the time-varying electromagnetic fields ω , the plasma density, and the static electric and

magnetic fields applied externally to the system. On the other hand, the static electric and magnetic fields also depend upon the type of the boundary condition imposed. Thus, in principle, once the electric current density \vec{J} is determined, the time-averaged power density absorbed by the medium can be determined by

$$p_r = \frac{1}{2} \operatorname{Re}(\vec{J}^* \cdot \vec{E}) \quad (3.18)$$

where the asterisk (*), denotes the complex conjugation and Re denotes the real part.

The integral of p_r over a volume in the medium can be regarded as the net time-averaged power flow into the volume.

The second approach is adopted for the present study, with the aid of a series of appropriate assumptions listed below.

B. Basic Assumptions Made in the Analysis

1. Assumption 1

The Lorentz gas model (73-75) is assumed to be applicable.

The weakly ionized argon gas under study can be regarded as a plasma in which the number densities of electrons and positive ions are considerably less than the number density of the neutral particles. Only the electron gas component of the mixture participates in the phenomenon of interest. The electronic motion is modified by collisions

with the neutral particles, which are assumed to have an infinite mass. Interactions with the positive ions are unimportant, as are electron-electron interactions. These conditions describe the plasma model known as the Lorentz gas. For this model of the plasma, the equation of motion for a single electron in an applied electric and magnetic field is given by the Langevin Equation as

$$m \frac{\partial \vec{u}}{\partial t} + m\nu \vec{u} = -e[\vec{E} + \vec{u} \times \vec{B}] \quad (3.19)$$

Where m and $e > 0$ denote the mass and electric charge of electron, respectively, and ν is the collision frequency of electron with a neutral.

2. Assumption 2

The rates of ionization and deionization are assumed to be negligibly small.

In the situation where the ionization and deionization processes are taking place in a plasma, the continuity equation takes form (73, 74).

$$\frac{\partial n}{\partial t} + \nabla \cdot (n\vec{u}) = \nu_I n - \alpha_R n^2 - \nu_A n \quad (3.20)$$

where n denotes the electron number density and $\nu_I, \alpha_R,$ and ν_A denotes, respectively, the ionization rate, the recombination coefficient, and the frequency of attaching collisions.

In the present study it is assumed that the right-hand side of Equation 3.20 is negligible compared with the left-hand side so that the continuity equation takes the following familiar form:

$$\frac{\partial n}{\partial t} + \nabla \cdot (n\vec{u}) = 0 \quad (3.21)$$

3. Assumption 3

The excitation fields produced by the rf current are predominant.

In the physical system under consideration, the argon gas is excited by the radiation fields produced by the rf current flow along the rf loop, which oscillates with time at a frequency of 27 MHz. The amplitude of the electromagnetic field induced in the vicinity of the rf loop antenna depends upon the current distribution on the rf loop structure. It should be noted that the resultant electric field intensity, evaluated at a point inside the plasma contained in the bell jar, can be expressed as

$$\vec{E}_r = \vec{E} + \vec{E}_s + \vec{E}_b \quad (3.22)$$

Where \vec{E} represents the externally applied electric field which includes the electric field induced by the 27 MHz rf current along the loop, and \vec{E}_s represents the space-charge field. \vec{E}_b represents the field due to the scattering

from the various boundaries, such as the bell jar wall, top and bottom plates, and the center-rod cathode.

It is assumed that $|\vec{E}_s| \ll |\vec{E}|$, and $|\vec{E}_p| \ll |\vec{E}|$ so that

$$\vec{E}_r = \vec{E} \quad (3.23)$$

which implies that quasi-electrical neutrality is held and that boundary effects on the electromagnetic field distribution are negligible.

Consequently, the rf electric field can be determined from the rf magnetic field via Maxwell's curl Equation, while the rf magnetic field can be determined from its source current distribution on the rf loop with the aid of the Biot-Savart law.

4. Assumption 4

Filamental current distribution on rf loop is assumed.

Since the rf loop is made of a copper tube of a finite thickness, the electric current would normally be distributed over the ring cross section, rather than over the circular cross section of the solid cylinder. For mathematical simplicity, it is assumed that the current is concentrated along the axis of the copper tube to form a U-shaped filament.

Furthermore, it is assumed that the current which, in general, can be induced on the rf loop structure by the

resultant electric field, \vec{E}_r , as described by Equation 3.22, is negligible compared to the rf current supplied externally. This type of the assumption has often been used in antenna theory (76).

5. Assumption 5

Time-harmonic variation of the form, $e^{j\omega t}$ is assumed.

All physical quantities of interest are considered to be composed of two parts, a time-independent part and a time-varying part, which are denoted by the subscripts 0 and 1, respectively:

$$\vec{B} = \vec{B}_0(\vec{r}) + \vec{B}_1(\vec{r})e^{j\omega t}$$

$$\vec{E} = \vec{E}_0(\vec{r}) + \vec{E}_1(\vec{r})e^{j\omega t}$$

$$\vec{H} = \vec{H}_0(\vec{r}) + \vec{H}_1(\vec{r})e^{j\omega t}$$

$$\vec{u} = \vec{u}_0(\vec{r}) + \vec{u}_1(\vec{r})e^{j\omega t}$$

$$\vec{J} = \vec{J}_0(\vec{r}) + \vec{J}_1(\vec{r})e^{j\omega t}$$

$$n = n_0(\vec{r}) + n_1(\vec{r})e^{j\omega t}$$

and

$$\rho = \rho_0(\vec{r}) + \rho_1(\vec{r})e^{j\omega t} \quad (3.24)$$

In the present investigation, the small-signal condition is assumed to be satisfied so that the terms involving the product of two time-varying quantities are negligible. This

assumption permits the linearization of the various differential equations involved so that a linear analysis can be made.

It should be noted that in Equation 3.24 the static magnetic flux density \vec{B}_0 in the present study is that produced by passing a dc current through the Helmholtz coil. This flux density can be controlled by varying the magnitude of the dc current. The experimental arrangement produces a uniform static magnetic flux density inside the bell jar where the plasma is contained.

The static electric field $\vec{E}_0(\vec{r})$ may be present or absent depending on whether or not a bias dc voltage is applied to the center-rod cathode. On the other hand, by Assumption 2, the time-varying electromagnetic fields $\vec{E}_1 e^{j\omega t}$ and $\vec{H}_1 e^{j\omega t}$ are those due to the current flow along the rf loop structure.

6. Assumption 6

The Helmholtz magnetic field \vec{B}_0 is assumed to be directed along the positive z-axis.

The static uniform magnetic flux density \vec{B}_0 produced by the Helmholtz coils is assumed to be directed along the positive z-axis, which coincides with the center-rod cathode and the axis of the cylindrical bell jar, i.e.,

$$\vec{B}_0 = \vec{a}_z B_0 \quad (3.25)$$

where \vec{a}_z is the unit vector.

Normally, the cylindrical coordinate systems might be used since the geometrical configuration of the bell jar tends to suggest the use of this type of coordinate system. If the boundary-value problem is to be solved, it would be advantageous to use the cylindrical coordinates system. However, for the purpose of studying the first-order effect of the rf excitation by the current loop, the rectangular, cartesian coordinate system can be used without too much complication since the boundary effects are not to be included in the present analysis. The coordinate system used for the present analysis is shown in Figure A.1.

With the various assumptions and simplifying approximations stated, the theoretical analysis of the plasma can now be carried out in detail by the following procedures:

First, the rf current distribution I along the rf excitation loop structure is assumed to be known. The expression for the time-varying magnetic field \vec{H}_1 is derived in terms of I with the aid of Biot-Savat law. The expression for the corresponding time-varying electric field \vec{E}_1 is then derived from the Maxwell's curl equation, which relates to \vec{H}_1 . When the plasma is subjected to the influence of the exciting electromagnetic fields \vec{E}_1 and \vec{H}_1 the electron

response manifests itself in the current density \vec{J}_1 . The expression for \vec{J}_1 is derived with the aid of Langevin Equation 3.15 in terms of \vec{E}_1 and \vec{H}_1 , and this expression can be put into the form $\vec{J}_1 = \overleftrightarrow{\sigma} \cdot \vec{E}_1$ with the aid of the convection current density definition, Equation 3.16, and the continuity equation, so that the conductivity tensor can also be identified. The expression for the power density absorbed by the medium can also be obtained.

With the aid of the experimental data obtained from the measurement of the rf power supplied to the rf loop imbedded in the plasma, the magnitude of the current I on the rf loop is estimated with the aid of transmission line theory, so that further numerical analysis can be carried out.

C. Radio-frequency Power Supplied to the Plasma

1. The conductivity tensor of magneto-plasma

If a static magnetic field is imposed on the plasma and the conditions are such as to render the plasma anisotropic, then the conductivity must be treated as a tensor.

Based on Assumptions 1 and 5, if the substitutions of Equation 3.24 into Equation 3.16 and the Langevin Equation (3.19) are made and those equations governing the time-independent quantities are separated from those concerning the time-varying quantities, the following are obtained.

The time-independent set of equations:

$$\vec{J}_0 = -en_0\vec{u}_0 \quad (3.26)$$

$$-e(\vec{E}_0 + \vec{u}_0 \times \vec{B}_0) = v m \vec{u}_0 \quad (3.27)$$

and the time-varying set of equations:

$$\vec{J}_1 = -e(n_0\vec{u}_1 + n_1\vec{u}_0) \quad (3.28)$$

$$j\omega m \vec{u}_1 = -e(\vec{E}_1 + \vec{u}_1 \times \vec{B}_0) - v m \vec{u}_1 \quad (3.29)$$

It should be pointed out that in Equation 3.29 the approximation $|\vec{u}_0 \times \vec{B}_1| \ll |\vec{E}_1|$ was made. This is reasonable because in a free space, $B_1 = \mu_0 H_1 = \mu_0 (\sqrt{\epsilon_0/\mu_0} \vec{E}_1) = E_1/c$, where c denotes the speed of light in free space, and because a nonrelativistic motion of the electron is being considered.

Equation 3.29 can be rearranged into the following form:

$$(1 + j\omega\tau)\vec{u}_1 + \vec{u}_1 \times \vec{B}_0 \mu = -\mu \vec{E}_1 \quad (3.30)$$

where $\mu = (e/mv)$ denotes the electron mobility, $\tau = (1/v)$ denotes the electron collision time, and e is the electronic charge, taken as a positive quantity.

Under Assumption 6, $\vec{B}_0 = \vec{a}_2 B_0$, Equation 3.30 yields the following component equations:

$$(1 + j\omega\tau)u_{1x} + (\mu B_0)u_{1y} = -\mu E_{1x} \quad (3.31a)$$

$$-(\mu B)u_{1x} + (1 + j\omega\tau)u_{1y} = -\mu E_{1y} \quad (3.31b)$$

$$(1 + j\omega\tau)u_{1z} = -\mu E_{1z} \quad (3.31c)$$

Consequently, the components of the time-varying velocity can be expressed explicitly in terms of the time-varying electric field components as follows:

$$\begin{aligned} u_{1x} &= A_{11}E_{1x} + A_{12}E_{1y} \\ u_{1y} &= A_{21}E_{1x} + A_{22}E_{1y} \\ u_{1z} &= A_{33}E_{1z} \end{aligned} \quad (3.32)$$

where

$$\begin{aligned} A_{11} &= \frac{-\mu(1+j\omega\tau)}{(\mu B_0)^2 + (1+j\omega\tau)^2} = A_{22} \\ A_{12} &= \frac{\mu^2 B_0}{(\mu B_0)^2 + (1+j\omega\tau)^2} = -A_{21} \\ A_{33} &= \frac{-\mu}{(1+j\omega\tau)} \end{aligned}$$

It should be noted that the time-varying electric convection current density \vec{J}_1 , depends on both the time-independent and the time-varying components of the electron number density as well as those of the electron velocity, in

general, as shown in Equation 3.28.

The time-independent (dc) drift velocity \vec{u}_0 is governed by the externally applied static electric \vec{E}_0 and magnetic flux density \vec{B}_0 via Equation 3.27, which can be given as

$$u_{0x} = (-\mu E_{0x} + \mu^2 B_0 E_{0y}) / (1 + (\mu B_0)^2) \quad (3.33a)$$

$$u_{0y} = (-\mu^2 B_0 E_{0x} - \mu E_{0y}) / (1 + (\mu B_0)^2) \quad (3.33b)$$

$$u_{0z} = -\mu E_{0z} \quad (3.33c)$$

The dc drift velocity is normally small, unless the externally applied static electric field (\vec{E}_0) is sufficiently high. Furthermore, for the small signal analysis, n_1 is much smaller than n_0 so that the approximation

$$|n_1 \vec{u}_0| \ll |n_0 \vec{u}_1| \quad (3.34)$$

is made in the following discussion. Consequently, Equation 3.28 is reduced to give

$$J_{1x} = -en_0 u_{1x}, \quad J_{1y} = -en_0 u_{1y}, \quad J_{1z} = -en_0 u_{1z} \quad (3.35)$$

The substitution of Equations 3.32 into Equation 3.35 then yields the desired relationship ($\vec{J}_1 = \overleftrightarrow{\sigma} \cdot \vec{E}_1$) between the current density \vec{J}_1 and the electric field intensity \vec{E}_1 . This relationship can be expressed in the following matrix form:

$$\begin{bmatrix} J_{1x} \\ J_{1y} \\ J_{1z} \end{bmatrix} = \begin{bmatrix} \sigma_1 & -\sigma_2 & 0 \\ \sigma_2 & \sigma_1 & 0 \\ 0 & 0 & \sigma_3 \end{bmatrix} \begin{bmatrix} E_{1x} \\ E_{1y} \\ E_{1z} \end{bmatrix} \quad (3.36)$$

$$\text{where } \tilde{\sigma}_1 = -en_0 A_{11} = \frac{\sigma_0 (1+j\omega\tau)}{(\mu B_0)^2 + (1+j\omega\tau)^2}$$

$$\tilde{\sigma}_2 = en_0 A_{12} = \frac{\sigma_0 (\mu B_0)}{(\mu B_0)^2 + (1+j\omega\tau)^2}$$

$$\tilde{\sigma}_3 = -en_0 A_{33} = \frac{\sigma_0}{(1+j\omega\tau)}$$

in which $\sigma_0 = (en_0\mu)$ represents the dc conductivity of the medium in the absence of the static magnetic field.

It should be noted that, in the case of very low frequency, $|\omega\tau| \ll 1$, and in the absence of a static magnetic field, $B_0 = 0$, $\sigma_1 = \sigma_3 = \sigma_0$ while $\sigma_2 = 0$ so that the conductivity tensor $\overleftrightarrow{\sigma}$ is reduced to a scalar quantity.

2. The distribution of excited electromagnetic fields

Suppose that the current flow along the u-shaped loop is filamental and has the form

$$\vec{I} = I_0 e^{j\omega t} \quad (3.37)$$

where I_0 is constant throughout the loop, and $\omega = 2\pi f$, with $f = 27$ MHz. For a given instance of time, the current

flow is in the direction indicated in Figure A.1.

The differential time-varying magnetic field intensity $d\vec{H}_1(p)$, evaluated at an observation point $P(x,y,z)$, produced by a differential time-varying current element $\hat{I} d\vec{l}$, located at the source point $Q(x',y',z')$ (see Figure A.1), can be obtained from the Biot-Savart law and is expressed as follows (77):

$$d\vec{H}_1 = \hat{I} d\vec{l} \times \vec{a}_R / 4\pi R^2 \quad (3.38)$$

where

$$\vec{R} = \vec{a}_x(x-x') + \vec{a}_y(y-y') + \vec{a}_z(z-z')$$

$$R = |\vec{R}|, \text{ and } \vec{a}_R = \vec{R}/|\vec{R}|$$

in which $(\vec{a}_x, \vec{a}_y, \vec{a}_z)$ are the base unit vectors in the cartesian coordinate system.

Integrating Equation 3.38 along the u-shaped loop yields the time-varying magnetic field $\vec{H}_1(p)$ which is expressed as follows (see Appendix A for the detailed derivation):

$$\vec{H}_1 = \vec{a}_x H_{1x} + \vec{a}_y H_{1y} + \vec{a}_z H_{1z} \quad (3.39)$$

with

$$H_{1x} = \hat{I} h_x / 4\pi, \quad H_{1y} = \hat{I} h_y / 4\pi, \quad H_{1z} = \hat{I} h_z / 4\pi$$

where

$$h_x = \left[\frac{(y-a)}{P} - \frac{(y+a)}{N} \right] (z-b) + \left[\frac{1}{M} + \frac{1}{F} \right] (y+a) \\ - \left[\frac{1}{K} + \frac{1}{V} \right] (y-a) z$$

$$\begin{aligned}
h_y &= \left[\frac{1}{N} - \frac{1}{P} \right] (z-b)x + \left[\frac{1}{K} - \frac{1}{M} \right] zx \\
h_z &= \left[\frac{(y-a)}{V} - \frac{(y+a)}{F} \right] x
\end{aligned} \tag{3.40}$$

in which

$$\begin{aligned}
N(x,y,z) &= \{x^2 + (y+a)^2\} [x^2 + (y+a)^2 + (z-b)^2]^{\frac{1}{2}} \\
M(x,y,z) &= \{x^2 + (y+a)^2\} [x^2 + (y+a)^2 + z^2]^{\frac{1}{2}} \\
P(x,y,z) &= \{x^2 + (y-a)^2\} [x^2 + (y-a)^2 + (z-b)^2] \\
K(x,y,z) &= \{x^2 + (y-a)^2\} [x^2 + (y-a)^2 + z^2]^{\frac{1}{2}} \\
V(x,y,z) &= (x^2+z^2) [x^2 + (y-a)^2 + z^2]^{\frac{1}{2}} \\
F(x,y,z) &= (x^2+z^2) [x^2 + (y+a)^2 + z^2]^{\frac{1}{2}}
\end{aligned} \tag{3.41}$$

On the other hand, the time-varying electric field intensity \vec{E}_1 and the time-varying magnetic field intensity \vec{H}_1 are related by Equation 3.6 which yields

$$\nabla \times \vec{H}_1 = \overleftrightarrow{\sigma} \cdot \vec{E}_1 + j\omega\epsilon_0 \vec{E}_1 \tag{3.42}$$

which can be written as

$$\nabla \times \vec{H}_1 = \overleftrightarrow{\gamma} \cdot \vec{E}_1 \tag{3.43}$$

where the effective conductivity tensor $\overleftrightarrow{\gamma}$ has the form:

$$\vec{\gamma} = \begin{bmatrix} \gamma_1 & -\gamma_2 & 0 \\ \gamma_2 & \gamma_1 & 0 \\ 0 & 0 & \gamma_3 \end{bmatrix} \quad (3.44)$$

where

$$\gamma_1 = \sigma_1 + j\omega\epsilon_0 \quad \gamma_2 = \sigma_2$$

and

$$\gamma_3 = \sigma_3 + j\omega\epsilon_0$$

Equation 3.43 can also be expressed in the component form as follows:

$$\frac{\gamma}{4\pi} \left[\frac{\partial h_z}{\partial y} - \frac{\partial h_y}{\partial z} \right] = \gamma_1 E_{1x} - \gamma_2 E_{1y} \quad (3.45a)$$

$$\frac{\gamma}{4\pi} \left[\frac{\partial h_x}{\partial z} - \frac{\partial h_z}{\partial x} \right] = \gamma_2 E_{1x} + \gamma_1 E_{1y} \quad (3.45b)$$

$$\frac{\gamma}{4\pi} \left[\frac{\partial h_y}{\partial x} - \frac{\partial h_x}{\partial y} \right] = \gamma_3 E_{1z} \quad (3.45c)$$

in which the functions h_x , h_y , and h_z are given by Equation 3.40.

Solving the set of algebraic equations 3.45a,b,c explicitly for E_{1x} , E_{1y} , and E_{1z} yields

$$E_{1x} = \frac{\gamma}{4\pi} \left[\frac{\gamma_1}{(\gamma_1^2 + \gamma_2^2)} M_x + \frac{\gamma_2}{(\gamma_1^2 + \gamma_2^2)} M_y \right] \quad (3.46a)$$

$$E_{1y} = \frac{\gamma}{4\pi} \left[\frac{-\gamma_2}{(\gamma_1^2 + \gamma_2^2)} M_x + \frac{\gamma_1}{(\gamma_1^2 + \gamma_2^2)} M_y \right] \quad (3.46b)$$

$$E_{1z} = \frac{\gamma}{4\pi} \left[\frac{1}{\gamma_3} M_z \right] \quad (3.46c)$$

where

$$M_x = \left(\frac{\partial h_z}{\partial y} - \frac{\partial h_y}{\partial z} \right) \quad (3.47a)$$

$$M_y = \left(\frac{\partial h_x}{\partial z} - \frac{\partial h_z}{\partial x} \right) \quad (3.47b)$$

$$M_z = \left(\frac{\partial h_y}{\partial x} - \frac{\partial h_x}{\partial y} \right) \quad (3.47c)$$

Substitution of Equation 3.40 into Equations 3.47 yields

$$M_x = \left[\frac{x}{[x^2 + (y-a)^2 + (z-b)^2]^{3/2}} - \frac{x}{[x^2 + (y+a)^2 + (z-b)^2]^{3/2}} \right] \quad (3.48)$$

$$M_y = \left[\frac{y-a}{[x^2 + (y-a)^2 + z^2]^{3/2}} - \frac{y+a}{[x^2 + (y+a)^2 + z^2]^{3/2}} \right]$$

$$M_z = \left[\frac{(z-b)}{[x^2 + (y-a)^2 + (z-b)^2]^{3/2}} - \frac{z-b}{[x^2 + (y+a)^2 + (z-b)^2]^{3/2}} \right]$$

It is constructive, at this point, to estimate the contribution of Maxwell's displacement current density to the total current density in Equation 3.42. It is sufficient to compare the magnitude $|\omega\epsilon_0|$ with $|\sigma_1|$ or $|\sigma_3|$ in Equation (3.44). First, the value of the electron collision frequency for the plasma under consideration must be known. Since the plasma under study is a weakly ionized gas (the

Lorentz gas model is being considered), the most important collision factor is that due to electrons colliding with neutral particles; consequently, electron-ion and electron-electron interaction can be neglected. The elastic mean free path of the electron λ_c is given (78) by

$$\lambda_c = 1/NQ \quad (3.49)$$

Where N is the number density of neutral particles, in m^{-3} , and Q denotes the elastic collision cross section, in m^2 .

The collision frequency ν is defined as the number of collisions the electron undergoes per unit time (per second). In one second the electron travels, on the average, a distance equal to its mean random velocity \bar{v} in meters. Since it collides at the rate of $1/\lambda_c$ collisions per unit path, the number of collisions per second is

$$\nu = \bar{v}/\lambda_c = \bar{v}NQ \quad (3.50)$$

The mean random velocity \bar{v} of a thermal collection of electrons in any direction is

$$\bar{v} = \sqrt{8KT/(m\pi)} = 6.21 \times 10^3 \sqrt{T} \text{ m/sec}$$

The total elastic collision cross section NQ , due to electron impact for some gases, according to published experimental measurements (79, 80), has been plotted against the electron energy in Figure 3.6 of the reference (78) for

the case where $T = 0^\circ \text{C} = 273^\circ \text{K}$, $p_0 = 1 \text{ Torr}$, and $N_0 = 3.56 \times 10^{22} \text{ molecules/m}^3$.

From the gas law, $p = NKT$, where K is Boltzmann's constant, it follows that

$$N = N_0 (p/p_0) (T_0/T) \quad (3.51)$$

so that

$$(NQ) = (N_0 Q) p (273/T) \quad (3.52)$$

upon substitution of Equation 3.52 into Equation 3.50, the collision frequency can be estimated.

From Table 1 of Section II, the plasma under study has parameters in the following ranges: electron density, $3 \times 10^9 < n_e < 9 \times 10^9 \text{ cm}^{-3}$; electron temperature, $6 \times 10^4 < T_e < 11 \times 10^4^\circ \text{K}$; thermal velocity, $1.5 \times 10^8 < \bar{v} < 2.2 \times 10^8 \text{ cm/sec}$. Moreover, the gas pressure $p = 7.5 \times 10^{-4} \text{ Torr}$, and the gas temperature $T = 703^\circ \text{K}$.

Suppose that an electron in the plasma has a thermal energy of 8 eV, with the corresponding kinetic temperature $T = 9.3 \times 10^4^\circ \text{K}$, and thermal velocity $\bar{v} = 1.186 \times 10^6 \text{ m/sec}$. From Figure 3.6 of reference (78), $N_0 Q = 50 \text{ cm}^{-1}$ for the electron energy of 8 eV. The value of the total elastic collision cross section (NQ) for the plasma under study is given by Equation 3.52 as $1.456 \times 10^{-2} \text{ cm}^{-1}$; consequently, the collision frequency, ν , according to

Equation 3.50, is $1.727 \times 10^6 \text{ sec}^{-1}$, and the electron mobility $\mu = (e/mv) = 1.019 \times 10 \text{ m}^2 \text{v}^{-1} \text{sec}^{-1}$ so that the dc conductivity $\sigma_0 = (n_e \mu e) = 53.3 \text{ } \Omega/\text{m}$ when $n_e = 3 \times 10^9 \text{ cm}^{-3}$.

Since the plasma is subjected to a dc magnetic field produced by the Helmholtz coils, which have $H = 19 \text{ Oe}$ or $B_0 = 19 \text{ G} = 19 \times 10^{-4} \text{ Wb/m}^2$, $(\mu B_0) = 193.6$. At $f = 27 \text{ MHz}$, $(\omega\tau) = (\frac{\omega}{\nu}) = 98.2$ and $(\omega\epsilon_0) = 1.50 \times 10^{-3} \text{ } \Omega/\text{m}$. Then, the numerical analysis using Equation 3.36 shows that $|\sigma_1/\omega\epsilon_0| = 125$, $|\sigma_2/\omega\epsilon_0| = 250$, and $|\sigma_3/\omega\epsilon_0| = 360$, thus

$$|\omega\epsilon_0| \ll |\tilde{\sigma}_1| \quad \text{and} \quad |\omega\epsilon_0| \ll |\tilde{\sigma}_3| \quad (3.53)$$

which suggests that the contribution of the displacement current can be neglected in the plasma under study.

Consequently, in Equation 3.44 $\gamma_1 = \sigma_1$, $\gamma_2 = \sigma_2$, and $\gamma_3 = \sigma_3$ so that Equation 3.46 becomes

$$E_{1x} = \frac{\gamma}{4\pi} e_x, \quad E_{1y} = \frac{\gamma}{4\pi} e_y, \quad E_{1z} = \frac{\gamma}{4\pi} e_z \quad (3.54)$$

where

$$e_x = \left(\frac{\sigma_1}{(\sigma_1^2 + \sigma_2^2)} M_x + \frac{\sigma_2}{(\sigma_1^2 + \sigma_2^2)} M_y \right) \quad (3.55a)$$

$$e_y = \left(\frac{-\sigma_2}{(\sigma_1^2 + \sigma_2^2)} M_x + \frac{\sigma_1}{(\sigma_1^2 + \sigma_2^2)} M_y \right) \quad (3.55b)$$

$$e_z = \left(\frac{1}{\sigma_3} M_z \right) \quad (3.55c)$$

where M_x , M_y , and M_z are given by Equation 3.48, while σ_1 , σ_2 , and σ_3 are given by Equation 3.36. Thus, for the plasma under study the distribution of the time-varying magnetic field intensity \vec{H}_1 is given by Equation 3.39 while the time-varying electric field intensity \vec{E}_1 is given by Equation 3.54.

3. The power density

It is well known (81) that the concept of complex power density \hat{p} has been used effectively in determining the energy stored in an electromagnetic field problem or the power absorbed by the medium. For the present study, the complex power density \hat{p} can be defined as

$$\hat{p} = \frac{1}{2}[\vec{E}_1 e^{j\omega t} \cdot \vec{J}_1^* e^{-j\omega t}] = \frac{1}{2}[\vec{E}_1 \cdot (\vec{\sigma}^* \cdot \vec{E}_1^*)] \quad (3.56)$$

where * denotes the complex conjugation.

The real part of the complex power density, $p_r \equiv \text{Re}(\hat{p})$, represents the time-averaged power density absorbed in the medium, and the imaginary part of complex power density, $p_i \equiv \text{Im}(\hat{p})$, contributes to the energy stored in the medium.

The substitution of Equation 3.36 into Equation 3.56 yields

$$\begin{aligned} \hat{p} = & \frac{1}{2}[\hat{\sigma}_1^*(|E_{1x}|^2 + |E_{1y}|^2) + \hat{\sigma}_3^*|E_{1z}|^2 + \\ & + \hat{\sigma}_2^*(E_{1x}^*E_{1y} - E_{1x}E_{1y}^*)] \end{aligned} \quad (3.57)$$

where the time-varying electric field components, E_{1x} , E_{1y} , and E_{1z} are given by Equation 3.55.

It should be noted that the collisions in a plasma cause the directed energy of motion to be redistributed in a random manner. In a weakly ionized gas, energy given to ions by an electric field is rapidly transferred to neutrals and lost to the boundaries. This energy is usually small in any case. Electrons, on the other hand, find it difficult to transfer energy by elastic collisions with much heavier particles and are therefore readily heated until excitation and ionization begin to be noticeable in the weakly ionized gas. The heating of the plasma can be calculated with the aid of what is called the cold plasma conductivity equation.

Using the fact that $(E_{1x}^*E_{1y} - E_{1x}E_{1y}^*) = 2j\text{Im}(E_{1x}^*E_{1y})$ is a purely imaginary quantity, and $|E_{1x}|$, $|E_{1y}|$, and $|E_{1z}|$ are positive real quantities, if \tilde{p} , $\tilde{\sigma}_1$, $\tilde{\sigma}_2$, and $\tilde{\sigma}_3$ are written as

$$\begin{aligned}\tilde{p} &= p_r + jp_i, & \tilde{\sigma}_1 &= \sigma_{1r} + j\sigma_{1i} \\ \tilde{\sigma}_2 &= \sigma_{2r} + j\sigma_{2i}, & \tilde{\sigma}_3 &= \sigma_{3r} + j\sigma_{3i}\end{aligned}\tag{3.58}$$

Then the real and imaginary parts of Equation 3.57 are given respectively by

$$P_r = \frac{1}{2}[\sigma_{1r}(|E_{1x}|^2 + |E_{1y}|^2) + 2\sigma_{2i}\text{Im}\cdot(E_{1x}^*E_{1y}) + \sigma_{3r}|E_{1z}|^2] \quad (3.59a)$$

and

$$P_i = \frac{1}{2}[\sigma_{1i}(|E_{1x}|^2 + |E_{1y}|^2) - 2\sigma_{2r}\text{Im}\cdot(E_{1x}^*E_{1y}) + \sigma_{3i}|E_{1z}|^2] \quad (3.59b)$$

where $|E_{1x}|$, $|E_{1y}|$, and $|E_{1z}|$ are the magnitudes of the electric field components which are real and are proportional to $|I|$. σ_{nr} and σ_{ni} are, respectively, the real and imaginary parts of the complex component of the conductivity tensor, with $n = 1, 2$, or 3 , which are given by Equation 3.36.

Equations 3.59 can be expressed in the following forms with the aid of Equations 3.54 and 3.55 (see Appendix C for the detailed derivation):

$$P_r(x, y, z) = \frac{1}{2}|I|^2 S_r(x, y, z) \quad (3.60a)$$

where

$$S_r(x, y, z) = \frac{1}{(4\pi)^2} \left\{ \frac{\sigma_r}{|\Delta|^2} (M_x^2 + M_y^2) + \frac{\sigma_{3r}}{|\sigma_3|^2} M_z^2 \right\} \quad (3.60b)$$

and

$$p_i(x,y,z) = \frac{1}{2} |I|^2 S_i(x,y,z) \quad (3.61a)$$

where

$$S_i(x,y,z) = \frac{1}{(4\pi)^2} \left\{ \frac{q_i}{|\Delta|^2} (M_x^2 + M_y^2) + \frac{\sigma_{3i}}{|\sigma_3|^2} M_z^2 \right\} \quad (3.61b)$$

in which

$$q_r = \sigma_{1r} (|\sigma_1|^2 + |\sigma_2|^2) - 2\sigma_{2i} (\sigma_{1r}\sigma_{2i} - \sigma_{2r}\sigma_{1i}) \quad (3.62a)$$

$$q_i = \sigma_{1i} (|\sigma_1|^2 + |\sigma_2|^2) + 2\sigma_{2r} (\sigma_{1r}\sigma_{2i} - \sigma_{2r}\sigma_{1i}) \quad (3.62b)$$

$$|\Delta|^2 = \{(\sigma_{1r}^2 + \sigma_{2r}^2) - (\sigma_{1i}^2 + \sigma_{2i}^2)\}^2 + 4(\sigma_{1r}\sigma_{1i} + \sigma_{2r}\sigma_{2i})^2 \quad (3.62c)$$

with

$$\sigma_{1r} = \sigma_0 (b_0^2 + a_0^2 + 1) / g_0, \quad \sigma_{1i} = \sigma_0 a_0 (b_0^2 - a_0^2 - 1) / g_0$$

$$\sigma_{2r} = \sigma_0 b_0 (b_0^2 - a_0^2 + 1) / g_0, \quad \sigma_{2i} = -2\sigma_0 a_0 b_0 / g_0$$

$$\sigma_{3r} = \sigma_0 / (1 + a_0^2), \quad \sigma_{2i} = -a_0 \sigma_0 / (1 + a_0^2)$$

$$g_0 = [(b_0^2 - a_0^2 + 1)^2 + 4a_0^2], \quad a_0 = (\omega\tau)$$

$$b_0 = (\mu B_0) \quad (3.63)$$

Having obtained the expression for the time-averaged power per unit volume absorbed by the plasma, the total absorbed power P_r can, in principle, be evaluated by the integration of $p_r(x,y,z)$ over the region which is

occupied by the plasma. That is to say, P_r can be expressed as

$$P_r = \frac{1}{2} |\dot{I}|^2 \iiint_{\tau_0} S_r(x, y, z) dx dy dz \quad (3.64)$$

where τ_0 is the volume occupied by the plasma, bounded by the cylindrical bell jar from outside by the insulating plates at the top and bottom and by the central rod cathode and the rf excitation loop structure from inside. Thus τ_0 has a very complicated boundary configuration. In order to evaluate the integral in Equation 3.64, the limits of the integration must be specified to describe the boundaries of the region of the integration.

On the other hand, the total power stored in the volume P_i , can be expressed as

$$P_i = \frac{1}{2} |\dot{I}|^2 \iiint_{\tau_0} S_i(x, y, z) dx dy dz \quad (3.65)$$

Since the rf excitation loop can be regarded as an antenna radiating in the plasma environment, if the total time-averaged power absorbed by its surrounding medium is known, the equivalent radiation resistance of the rf loop antenna R_r can be conveniently defined as

$$R_r = \frac{2P_r}{|\dot{I}|^2} \quad (3.66)$$

so that

$$R_r = \iiint_{\tau_0} S_r(x, y, z) dx dy dz \quad (3.67)$$

Similarly, the equivalent antenna reactance X_A can be defined as

$$X_A = \frac{2P_i}{|I|^2} \quad (3.68)$$

so that

$$X_A = \iiint_{\tau_0} S_i(x, y, z) dx dy dz \quad (3.69)$$

Since the rf power is supplied to the plasma by a 27 MHz generator through a section of transmission line and the rf excitation loop imbedded in the plasma, conventional circuit and transmission line theory can be utilized in the analyses of the electrical network involved in the present study. The electrical load under consideration consists of the rf excitation loop antenna imbedded in the plasma, which can be represented by a circuit parameter of the load impedance, $\tilde{z}_L = R + jX$. Here R and X denote, respectively, the load resistance and the load reactance.

With the aid of the antenna theory (82), the load under consideration can be represented by

$$\tilde{z}_L = R + jX = (R_\ell + R_r) + j(X_\ell + X_A) \quad (3.70)$$

where R_ℓ denotes the loss resistance due to the copper losses in the rf loop structure, and R_r the radiation

resistance, is given by Equation 3.67. Since the rf loop structure is made of copper, this loss is expected to be small in comparison to the power radiated into the plasma so that $R_\ell \ll R_r$.

$X_\ell = \omega L$ is the reactance produced by the self-inductance of the rf excitation loop L , and X_A is the antenna reactance, given by Equation 3.69, and can be either inductive or capacitive. It should be noted that R_r and X_A depend upon the physical conditions of the plasma and the geometry of the rf loop antenna.

Having specified the load impedance, the equivalent circuit of the electrical network under consideration can be represented as shown in Figure 3.1.

According to transmission line theory, the impedance looking toward load $\tilde{z}_{in}(\ell)$ at an arbitrary point along a loss less transmission line, located ℓ meters away from the load, can be expressed in terms of the load impedance z_L and the characteristic impedance z_0 in the following familiar form (83):

$$z_{in} = \frac{V_{in}}{I_{in}} = z_0 \left[\frac{\tilde{z}_L + jz_0 \tan \beta \ell}{z_0 + j\tilde{z}_L \tan \beta \ell} \right] \quad (3.71)$$

where β is the wave number of the voltage wave and of the current wave traveling along the line. For example, in an air-filled transmission line, $\beta \approx \frac{\omega}{c}$, where c is the speed

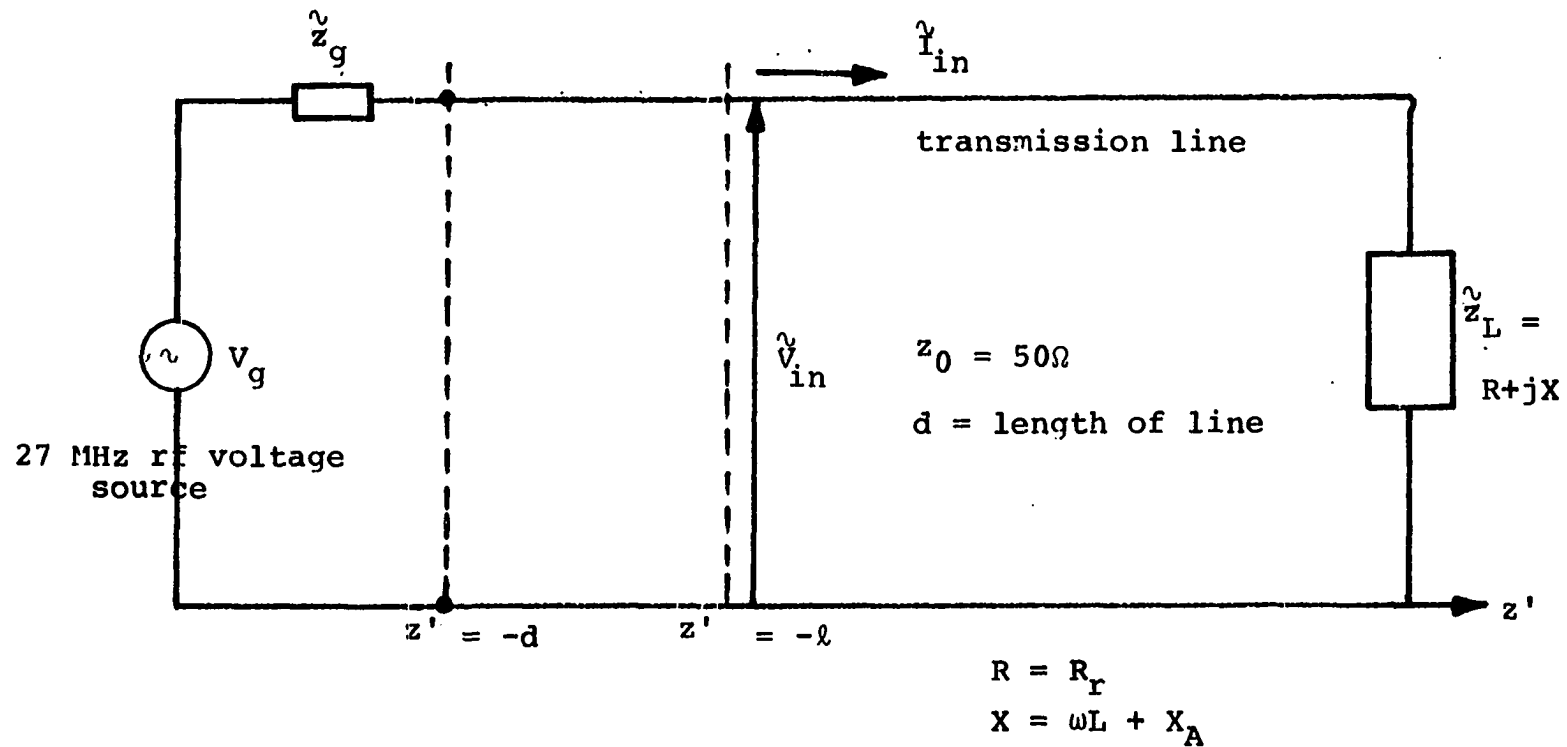


Figure 3.1. Equivalent circuit for the electrical network under study. z_g = internal impedance of the voltage source, z_0 = characteristic impedance of transmission line

of light in free space. \hat{V}_{in} is the voltage across the line, and \hat{I}_{in} is the total current flow toward the load at $z' = -l$.

When $\hat{z}_{in} = (R_{in} + jX_{in})$ is known, the value of the internal impedance of source $\hat{z}_g = (R_g + jX_g)$ can be chosen in such a way as to have a maximum transfer of power into the load, based on the "maximum power transfer theorem" of circuit theory (84). For example, the condition for the maximum power supplied by the source can be given by

$$\hat{z}_g = \hat{z}_{in}^* \quad (3.72)$$

4. Estimation of the self-inductance of the rf excitation loop

Suppose for a given instant of time that the current flow in the rf excitation loop is in the direction indicated in Figure 3.1.

The magnetic flux lining the rf loop is given by

$$\Phi = \iint_A \vec{B}_1 \cdot d\vec{S} = \int_{\delta}^b \int_{-(a-\delta)}^{(a-\delta)} B_{1x} dy dz \quad (3.71)$$

with

$$B_{1x} = \mu_0 H_{1x}(0, y, z) = \frac{\mu_0 I}{4\pi} h_x(0, y, z)$$

where $h_x(x, y, z)$ is given by Equation (3.40). The parameter $\delta \ll a$ is introduced to avoid integration through the singularity of h_x at $x=0$, $y=\pm a$ and $z=0$.

The self-inductance of the rf loop L can be expressed

as

$$L = \frac{\Phi}{I} = \frac{\mu_0}{4\pi} \int_{\delta}^b \int_{-(a-\delta)}^{(a-\delta)} h_x(0, y, z) dy dz \quad (3.72)$$

Setting $x=0$ in Equation 3.40, substituting into Equation 3.72, and evaluating the double integral, yields the following expression (see Appendix B for the details):

$$L = \frac{\mu_0}{4\pi} [6\sqrt{4a^2+b^2} - 12a - 6b - 2\delta \log(\sqrt{2} + 1) + \delta \log\left\{\frac{\sqrt{2}-1}{\sqrt{2}+1}\right\} + 2a \log\left\{\left(\frac{16a^2}{\delta^2}\right)\left[\frac{\sqrt{4a^2+b^2}-2a}{\sqrt{4a^2+b^2}+2a}\right]\right\}] \quad (3.73)$$

Once the values of parameters a , b , and δ are specified, the value of L can be estimated by Equation 3.73, which is illustrated in Section IV.

It should be observed that the time-averaged power density absorbed by the plasma p_r , given by Equation 3.60, depends not only on plasma parameters such as the electron number density n_0 , and the electron-neutral collision frequency ν (or σ_0 and μ), but also on the current in the rf loop I . The power absorbed by the plasma is consumed in heating up the plasma and contributes to the increase in electron temperature.

5. A method for determining the current in the rf excitation loop and the equivalent load impedance

The current flow in the rf loop can be measured directly with an appropriately scaled rf ammeter. Unfortunately, however, such an instrument was not available for the present investigation. Other methods of estimating the value of the current $|\hat{I}|$ were therefore employed. The method discussed below is based on measurement of the rf power flow toward and away from the load by an rf watt meter placed at some convenient location along the transmission line.

The experimental set-up used for the rf power measurement is shown in Figure 2.12b. Assume that the rf voltmeter and the rf power meter are placed at location $z' = -\ell$, as shown in Figure 3.1. The power flow toward the load at this location, denoted by W^+ , and the power flow toward generator, denoted by W^- , are measured.

From transmission theory (85) it is well known that the voltage and current along the line can be regarded as the superposition of the forward (toward the load) traveling wave and the backward (toward the generator) traveling wave, and expressed as follows:

$$\hat{V}_{in}(\ell) = \hat{V}_0^+ e^{j\beta\ell} + \hat{V}_0^- e^{-j\beta\ell} \quad (3.74a)$$

$$\hat{I}_{in}(\ell) = \frac{1}{z_0} [\hat{V}_0^+ e^{j\beta\ell} - \hat{V}_0^- e^{-j\beta\ell}] \quad (3.74b)$$

where \hat{V}_0^+ and \hat{V}_0^- are the complex amplitudes at the load of the forward and backward traveling voltage waves, respectively.

The input impedance $\hat{z}_{in}(\ell)$ can be expressed as

$$\hat{z}_{in}(\ell) = \frac{\hat{V}_{in}(\ell)}{\hat{I}_{in}(\ell)} = \bar{z}_0 \left[\frac{1 + \hat{\Gamma}_L e^{-j2\beta\ell}}{1 - \hat{\Gamma}_L e^{-j2\beta\ell}} \right] \quad (3.75)$$

where $\hat{\Gamma}_L \equiv (\hat{V}_0^- / \hat{V}_0^+)$ is the complex voltage reflection coefficient which can be written as

$$\hat{\Gamma}_L = \Gamma_L e^{j\theta} = \Gamma_r + j\Gamma_i \quad (3.76)$$

or

$$\Gamma_r = \Gamma_L \cos \theta, \text{ and } \Gamma_i = \Gamma_L \sin \theta \quad (3.77)$$

Equation (3.75) can also be written as

$$\frac{\hat{z}_L}{z_0} = \frac{1 - \hat{\Gamma}}{1 + \hat{\Gamma}} \quad (3.78)$$

where the voltage reflection coefficient at $z' = -\ell$, can be given by

$$\hat{\Gamma} = \Gamma_L e^{j(\theta - 2\beta\ell)} \quad (3.79)$$

The time-averaged power flow along the transmission line at location $z' = -\ell$ can be given, with the aid of Equations 3.74a and 3.74b, as

$$\frac{1}{2} \text{Re}[\hat{V}_{in} \hat{I}_{in}^*] = \frac{1}{2} \text{Re} \left[\left(\frac{|\hat{V}_0^+|^2}{z_0} - \frac{|\hat{V}_0^-|^2}{z_0} + \left\{ \frac{V_0^+ V_0^- e^{-j2\beta\ell}}{z_0} - \frac{V_0^+ V_0^- e^{+j2\beta\ell}}{z_0} \right\} \right) \right] \quad (3.80)$$

For a lossless line, the characteristic impedance z_0 and the wave number of the voltage and current wave β are real. Consequently, the quantity in the curly bracket on the right-hand side of Equation 3.80 is purely imaginary, so that

$$\frac{1}{2} \text{Re}[\hat{V}_{in}(\ell) \hat{I}_{in}^*(\ell)] = \frac{|\hat{V}_0^+|^2}{2z_0} - \frac{|\hat{V}_0^-|^2}{2z_0} \quad (3.81)$$

which is independent of ℓ . It should be noted that the first term on the right-hand side of Equation 3.81 represents the time averaged power flow toward the load, denoted by W^+ , and the second term represents the time-averaged power flow toward the generator, denoted by W^- . Moreover, it is of interest to note that the net time-averaged power flow is independent of the location along the line, which is to be expected since the lossless line is being considered.

On the other hand, at the load (by setting $\ell = 0$) in Equations 3.74a and 3.74b, the net time-averaged power flow is given by

$$\frac{1}{2} \text{RE}[\hat{V}_L \hat{I}_L^*] = \frac{1}{2} \left(\frac{|V_0^+|^2}{z_0} - \frac{|V_0^-|^2}{z_0} \right) \quad (3.82)$$

which implies that the time-averaged power absorbed by the

load is

$$P_{ab} = W^+ - W^- = \frac{1}{2} \operatorname{Re}[\hat{V}_L \hat{I}_L^*] = \frac{1}{2} \operatorname{Re}[\hat{V}_{in} \hat{I}_{in}^*] \quad (3.83)$$

where

$$W^+ = \frac{1}{2} \frac{|\hat{V}_0^+|^2}{z_0} \quad \text{and} \quad W^- = \frac{1}{2} \frac{|\hat{V}_0^-|^2}{z_0} \quad (3.84)$$

It is of interest to note that at this load since $\ell = 0$ and $z_L = z_{in}(0)$, Equation 3.78 becomes

$$\frac{z_L}{z_0} = \frac{1 + \hat{\Gamma}_L}{1 - \hat{\Gamma}_L} \quad (3.85a)$$

or

$$\hat{\Gamma}_L = \frac{z_L - z_0}{z_L + z_0} \quad (3.85b)$$

which expresses the relationship between the voltage reflection coefficient at the load $\hat{\Gamma}_L$ and the load impedance z_L . This is the basic relationship upon which the Smith chart is constructed.

Substitution of Equation 3.85b into Equation 3.75 yields the alternative form of $z_{in}(\ell)$ as given by Equation 3.71. Moreover, the power reflection coefficient $\eta \equiv (W^-/W^+)$ can be given by

$$\eta = \frac{|\hat{V}_0^-|^2}{2z_0} / \frac{|\hat{V}_0^+|^2}{2z_0} = |\hat{\Gamma}_L|^2 \quad (3.86)$$

From Equation 3.79

$$|\hat{\Gamma}| = |\hat{\Gamma}_L| = \Gamma_L, \quad \text{which suggests that the measurement}$$

of the power flow can be made anywhere on the line and still yield the information on $|\hat{\Gamma}_L|$.

Furthermore, the voltage distribution along the line is of interest. The absolute value of $V_{in}(\ell)$ (as would be given by a voltmeter) is desired, and this is given by Equation 3.74a as

$$|\hat{V}_{in}(\ell)| = |\hat{V}_0^+| \sqrt{1 + \Gamma_L^2 + 2\Gamma_L \cos \phi} \quad (3.87)$$

where

$$\phi \equiv (\theta - 2\beta\ell)$$

The magnitude of the current at the load, which is of primary interest in the present study, can be obtained from Equation 3.74b as

$$|\hat{I}_L| = |\hat{I}_{in}(\ell=0)| = \frac{|\hat{V}_0^+|}{z_0} \sqrt{(1 + \Gamma_L^2) - 2\Gamma_L \cos \phi} \quad (3.88)$$

which requires that $|\hat{V}_0^+|$, Γ_L , and $\theta = \phi + 2\beta\ell$ be known.

Suppose that measurements of the magnitude of rf voltage $|\hat{V}_{in}(\ell)|$, and the time-averaged power flow toward the load W^+ , and the time-averaged power flow toward the source W^- , are made at location $z' = -\ell$ as shown in Figure 3.1. Since z_0 is known, the magnitude of voltage reflection coefficient $\Gamma_L = \sqrt{W^-/W^+}$ can be determined using Equation 3.86. Similarly, from Equation 3.84, $|\hat{V}_0^+| = \sqrt{2W^+ z_0}$ can be calculated. On the other hand, since $(\beta\ell)$ is known, ϕ can be determined using Equation 3.87 so that the phase angle of

$\tilde{\Gamma}_L$, $\theta = (\phi + 2\beta l)$ can be calculated. Thus, the quantities on the right-hand side of Equation 3.88 are now known so that $|\tilde{\Gamma}_L|$ can be calculated. The numerical illustration of the estimation of $|\tilde{\Gamma}_L|$ is given in Section IV.

Once the complex voltage reflection coefficient at the load $\tilde{\Gamma}_L = \Gamma_L e^{j\theta}$ is known, the equivalent load impedance $\tilde{Z}_L = R + jX$ can easily be determined with the aid of the Smith chart or from Equation 3.85a.

6. Electric scalar potential and charge distribution

As was pointed out previously, knowledge of the electron number density $n(x, y, z) = n_0(x, y, z) + n_1(x, y, z)e^{j\omega t}$ is needed for the determination of the time-averaged power density, given by Equation 3.60 and Equation 3.61, which depends on the dc conductivity $\sigma_0 = (n_0 \mu e)$. It is also needed for determining the time-varying electric field intensity which is apparent from Equation 3.54 and Equation 3.55.

On the other hand, the electric field intensity and the electric space charge density ρ are related by Gauss's law, Equation 3.9, which can be written as

$$\nabla \cdot \vec{E} = \frac{\rho}{\epsilon_0} = \frac{e}{\epsilon_0} (n_i - n) \quad (3.89)$$

where n_i and n denote the positive ion and electron number density, respectively. Substitution of Equation 3.24 into

Equation 3.89 yields the following set of equations:

$$\nabla \cdot \vec{E}_0 = \frac{e}{\epsilon_0} [n_{i0} - n_0] \quad (3.90)$$

and

$$\nabla \cdot \vec{E}_1 = \frac{e}{\epsilon_0} [n_{i1} - n_1] \approx - \frac{e}{\epsilon_0} n_1 \quad (3.91)$$

For example, in the positive column region a way from the electrode boundary, the condition of electrical neutrality ($n_{i0} = n_0$) holds so that Equation 3.90 becomes

$$\nabla \cdot \vec{E}_0 = 0 \quad (3.92)$$

For the plasma under study, the displacement current density is negligible in comparison with the convection current density, so the quasi-static analysis is applicable. In this case, the electric field intensity \vec{E} can be expressed in terms of the electrical potential function $V(x, y, z)$ as

$$\vec{E} = -\nabla V \quad (3.93)$$

so that V is related to ρ by the Poisson's equation:

$$\nabla^2 V = - \frac{\rho}{\epsilon_0} \quad (3.94)$$

Once again, since $V = V_0 + V_1 e^{j\omega t}$, Equation 3.94 requires that the time-independent (dc) potential function V_0 satisfy Laplace's equation

$$\nabla^2 V_0 = 0 \quad (3.95)$$

and that the time-varying (rf) potential function V_1 satisfy the Poisson's equation

$$\nabla^2 V_1 = + \frac{e}{\epsilon_0} n_1 \quad (3.96)$$

Thus, in principle, the dc electric-potential distribution $V_0(x,y,z)$ can be found by solving the Laplace's equation 3.95 with appropriate boundary conditions imposed. Once $V_0(x,y,z)$ is found, \vec{E}_0 can be calculated so that the time-independent (dc) drift velocity \vec{u}_0 can be determined with the aid of Equation 3.33. Consequently, the dc electron number density $n_0(x,y,z)$ can be found by solving the following differential equation:

$$(\nabla n_0) \cdot \vec{u}_0 + n_0 \nabla \cdot \vec{u}_0 = 0 \quad (3.97)$$

which is the time-independent part of the continuity Equation 3.21.

On the other hand, the time-varying electric potential function V_1 and the time-varying electric field intensity \vec{E}_1 are related by

$$\nabla V_1 = -\vec{E}_1 \quad (3.98)$$

and the time-varying electron number n_1 and the time-varying electric field intensity \vec{E}_1 are related by Equation

3.91. Therefore, with \vec{E}_1 given by Equation 3.46, V_1 can be found by solving the differential Equation 3.98, and n_1 can be found by proper differentiation as indicated in Equation 3.91.

It should be pointed out that when a bias dc voltage, for example, is applied externally to the center-rod cathode located along the z-axis, due to the peculiar configuration of electrode system and the rf excitation loop, the determination of the dc potential distribution $V_0(x,y,z)$ inside of the bell jar involves the solution of a rather complicated boundary value problem. Some effort and attention have been given to the solution of this complicated boundary value problem. However, these efforts have not been very successful, and no significant result can yet be reported. The problem is therefore left for future investigation.

The experimental data obtained for the electron number density $n_e = n_0$, shown in Table 2 of Section II, tend to suggest that there is some spatial variation in the dc electron number density n_0 . It has been pointed out that in order to know how n_0 varies spatially, it is necessary to solve Equation 3.97 with an appropriate boundary condition imposed. This solution is not attempted here since the effect of the boundary has been neglected in the present study.

IV. NUMERICAL ILLUSTRATIONS

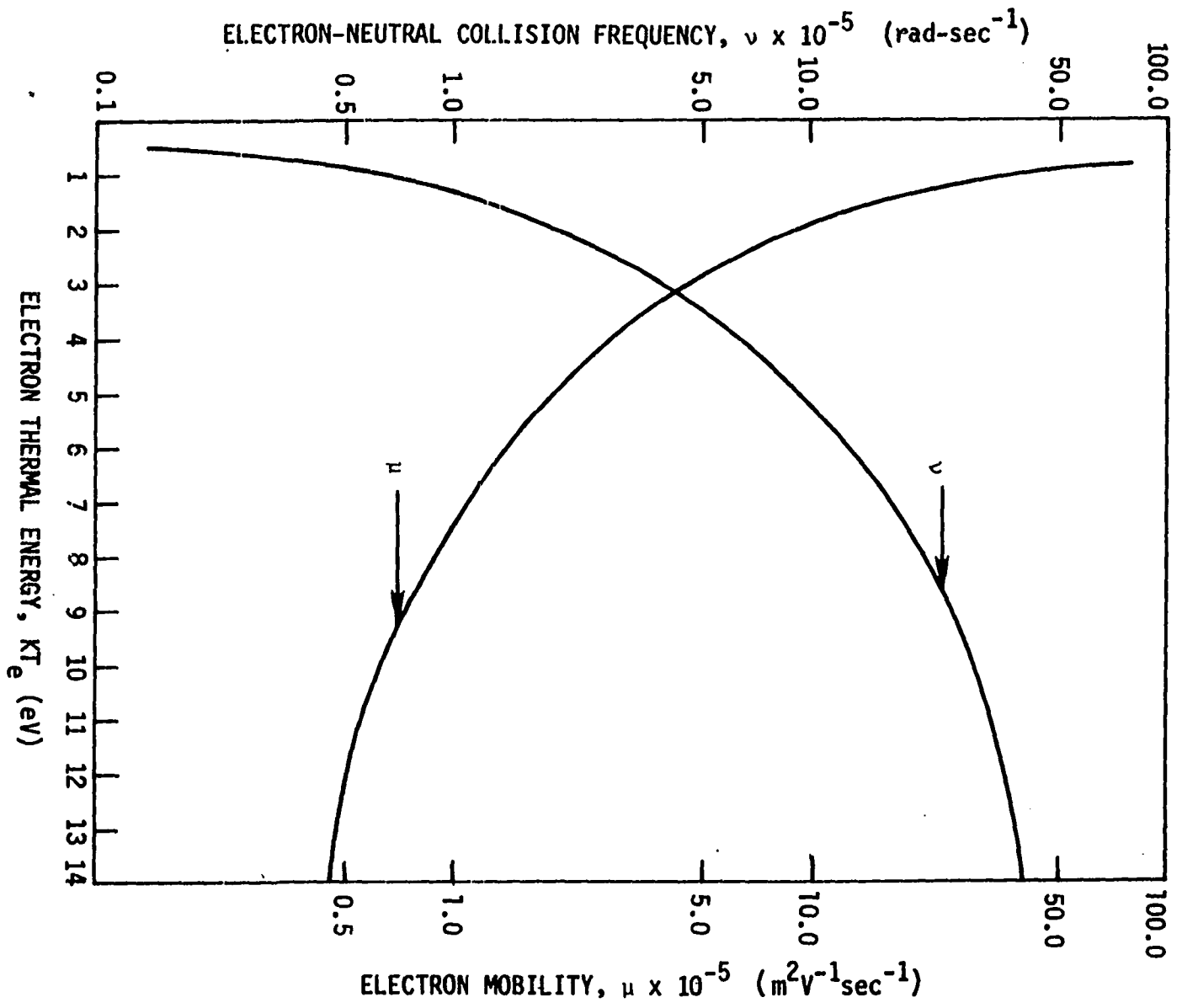
A. Plasma Parameter Variations

1. Electron collision frequency and mobility

As shown previously, the electron-neutral collision frequency ν can be calculated using Equations 3.50 and 3.52 and the experimental data given by Figure 3.6 of reference (78) for the total electron-collision cross section as a function of the electron energy. When the plasma is not subjected to a strong static electric field, the drift velocity of electron is insignificant in comparison to the random thermal velocity. Consequently, the collision frequency depends upon the thermal velocity of the electron as well as the total electron collision cross section; both are functions of electron kinetic energy. In other words, the value of collision frequency ν can be estimated once (KT_e) , the electron thermal energy, is specified. The variation of ν with (KT_e) is illustrated in Figure 4.1 for the argon plasma under study, which has a gas temperature of 703 °K and pressure of 7.5×10^{-4} Torr. The corresponding variation of the electron mobility, $\mu = (e/mv)$ with the electron thermal energy is also illustrated in Figure 4.1.

It is interesting to observe that the electron collision frequency ν for the plasma under study is of the

Figure 4.1. Variation of electron collision frequency and mobility with electron thermal energy



order of 10^6 rad/sec, and the mobility is of the order of $10^5 \text{ m}^2 \text{V}^{-1} \text{sec}^{-1}$. ν increases monotonically with (KT_e) while μ decreases monotonically with (KT_e) . The rate of change of both ν and μ decreases as (KT_e) increases.

2. Components of the conductivity tensor

Since the behavior of the electron mobility for the plasma has been specified, the components of the conductivity tensor $\tilde{\sigma}_n$, with $n = 1, 2, 3$, given in Equation 3.36 can now be investigated in detail, provided the static magnetic flux density B_0 , produced by the Helmholtz coils and the electron number density n_0 are known. In other words, the behavior of the components $\tilde{\sigma}_n(n_0, B_0, f, kTe)$ subject to changes in static magnetic flux density B_0 , electron number density n_0 , rf excitation frequency f , and electron thermal energy or temperature, is to be investigated. For the convenience of discussion, the component $\tilde{\sigma}_n$, with $n = 1, 2$, or 3 is written as

$$\tilde{\sigma}_n = \sigma_{nr} + j\sigma_{ni} \quad (4.1)$$

where σ_{nr} and σ_{ni} are real and are given by Equation 3.63.

First, it should be noted that $\tilde{\sigma}_n$ is proportional to the dc conductivity $\sigma_0 = (n_0 \mu e)$, which is apparent from Equation 3.36. This suggests that σ_{nr} and σ_{ni} both increase proportionally with n_0 . A typical electron number

density n_0 for the plasma under study is taken to be 6×10^9 electrons/cm³ for the present illustration. The plasma is excited by the rf fields produced by a 27 MHz power source via the rf current loop and is subjected to a uniform static magnetic flux density B_0 of 19 G, produced by the Helmholtz coils.

Since the collision time $\tau = (1/\nu)$ is also the function of the mobility μ , the variation of $\tilde{\sigma}_n$ with μ is of interest, and μ is taken as one of the independent variables in the present illustration. The variations of σ_{nr} and σ_{ni} with μ and with B_0 is investigated for a conveniently chosen set of parameter values.

The variation of $\sigma_n(\mu, B_0, f, n_0)$ with μ is illustrated in Figures 4.2a and 4.2b for $n_0 = 6 \times 10^9$ cm⁻³, $B_0 = 19$ G, and $f = 1$ and 27 MHz. The variation of $\tilde{\sigma}_n$ with B_0 is illustrated in Figures 4.3a,b and c, and Figures 4.4a,b,c and d for $\mu = 2.7 \times 10^5$ m²V⁻¹sec⁻¹, 8.5×10^4 m²V⁻¹sec⁻¹, 4.6×10^4 m²V⁻¹sec⁻¹ or $kT_e = 4$ eV, 8 eV, and 12 eV for the plasma under study. A detailed discussion of these plots is presented in Section V.

Figure 4.2a. Variation of the real parts of various components of the conductivity tensor with electron mobility, μ , for case $B_0 = 19$ G, and $n_e = 6 \times 10^9 \text{ cm}^{-3}$, with different values of frequency, f

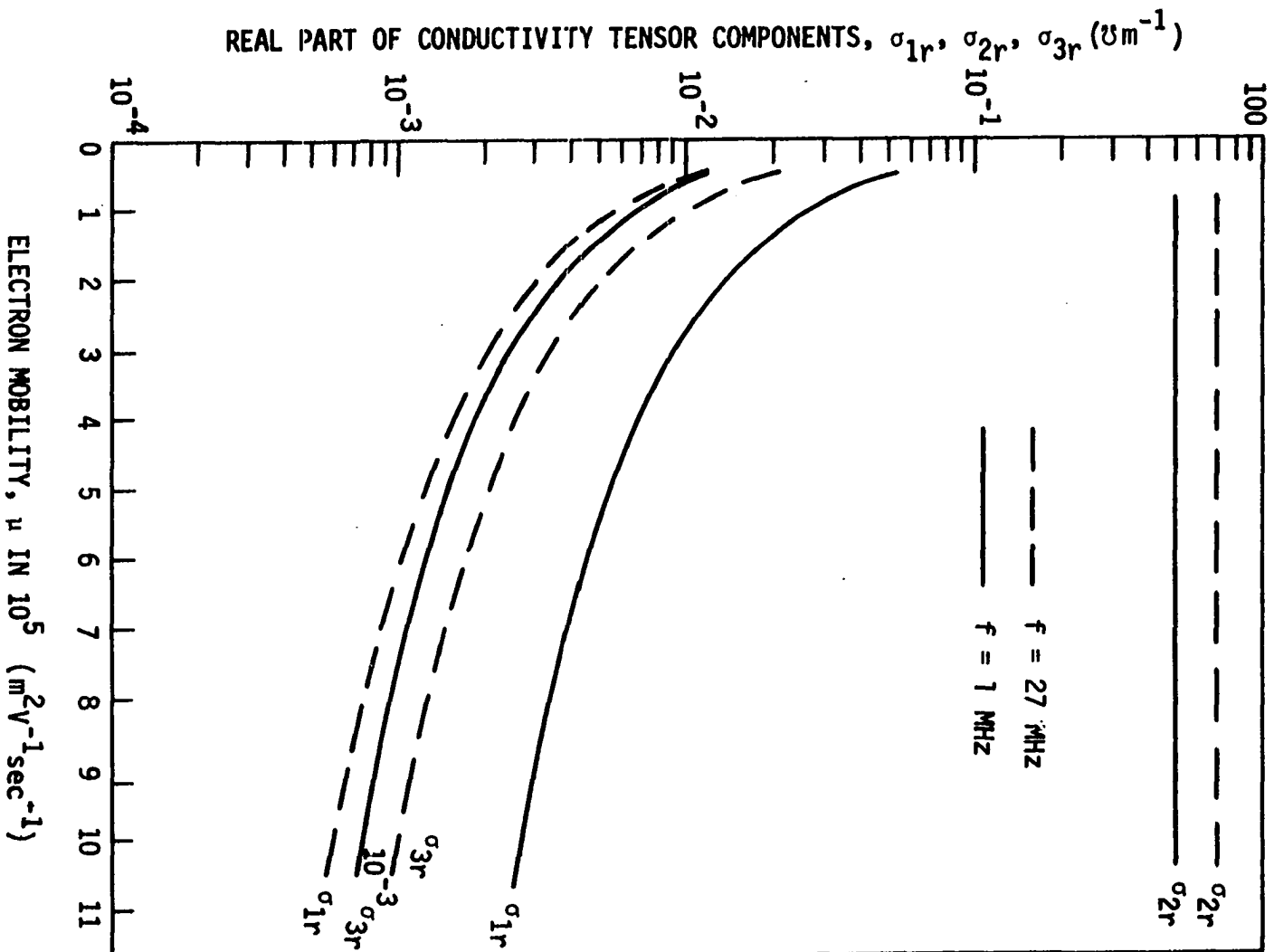


Figure 4.2b. Variation of the imaginary part of various components of the conductivity tensor with electron mobility, μ , for case $B_0 = 19$ G, and $n_e = 6 \times 10^9 \text{ cm}^{-3}$ with different values of frequency, f

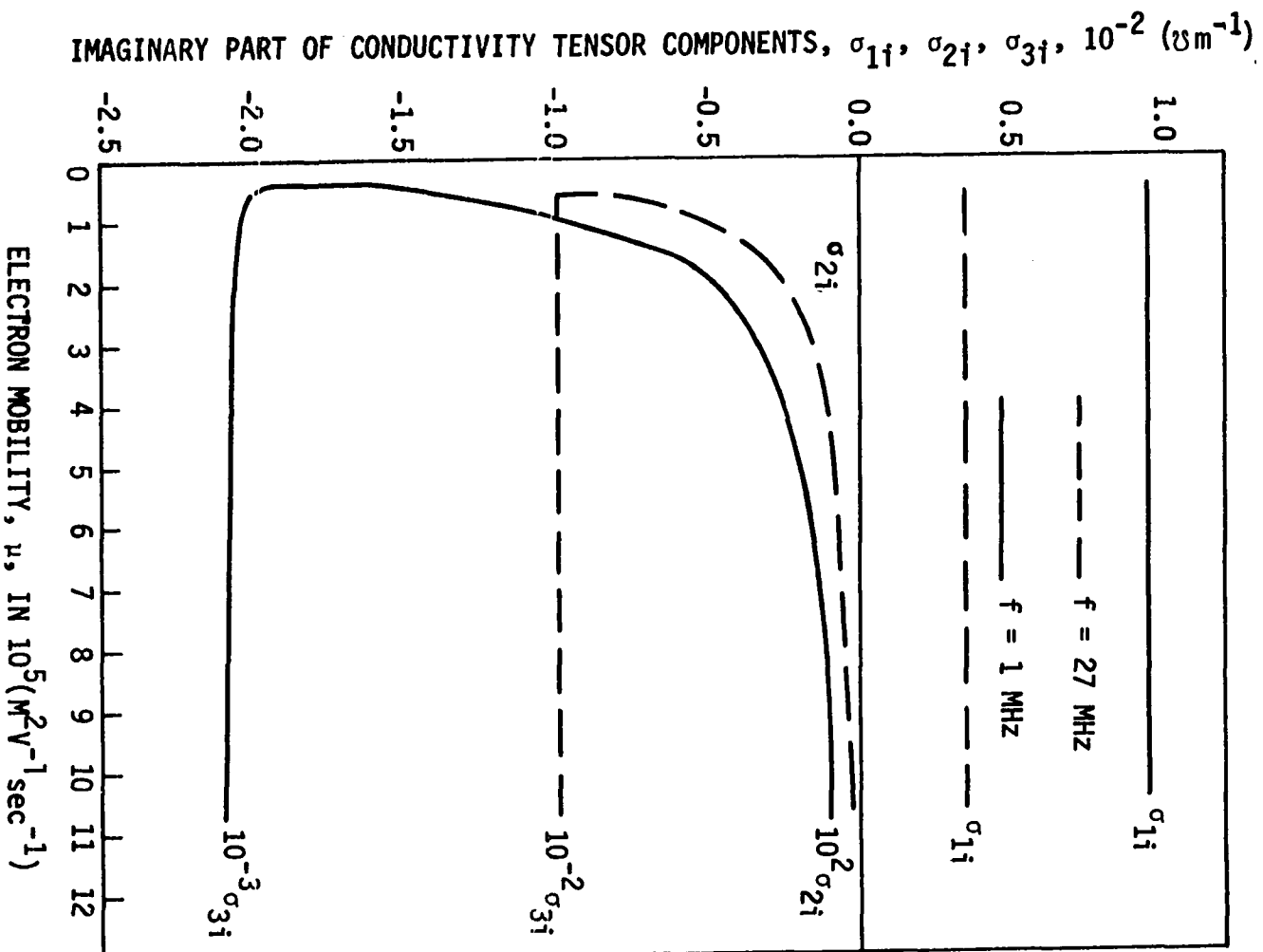


Figure 4.3a. Variation of various components of conductivity tensor with static magnetic flux density, B_0 for case, $f = 27$ MHz, $n_e = 6 \times 10^9 \text{ cm}^{-3}$, and $\mu = 2.7 \times 10^5 \text{ m}^2 \text{ v}^{-1} \text{ sec}^{-1}$ (or $kT_e = 4 \text{ eV}$)

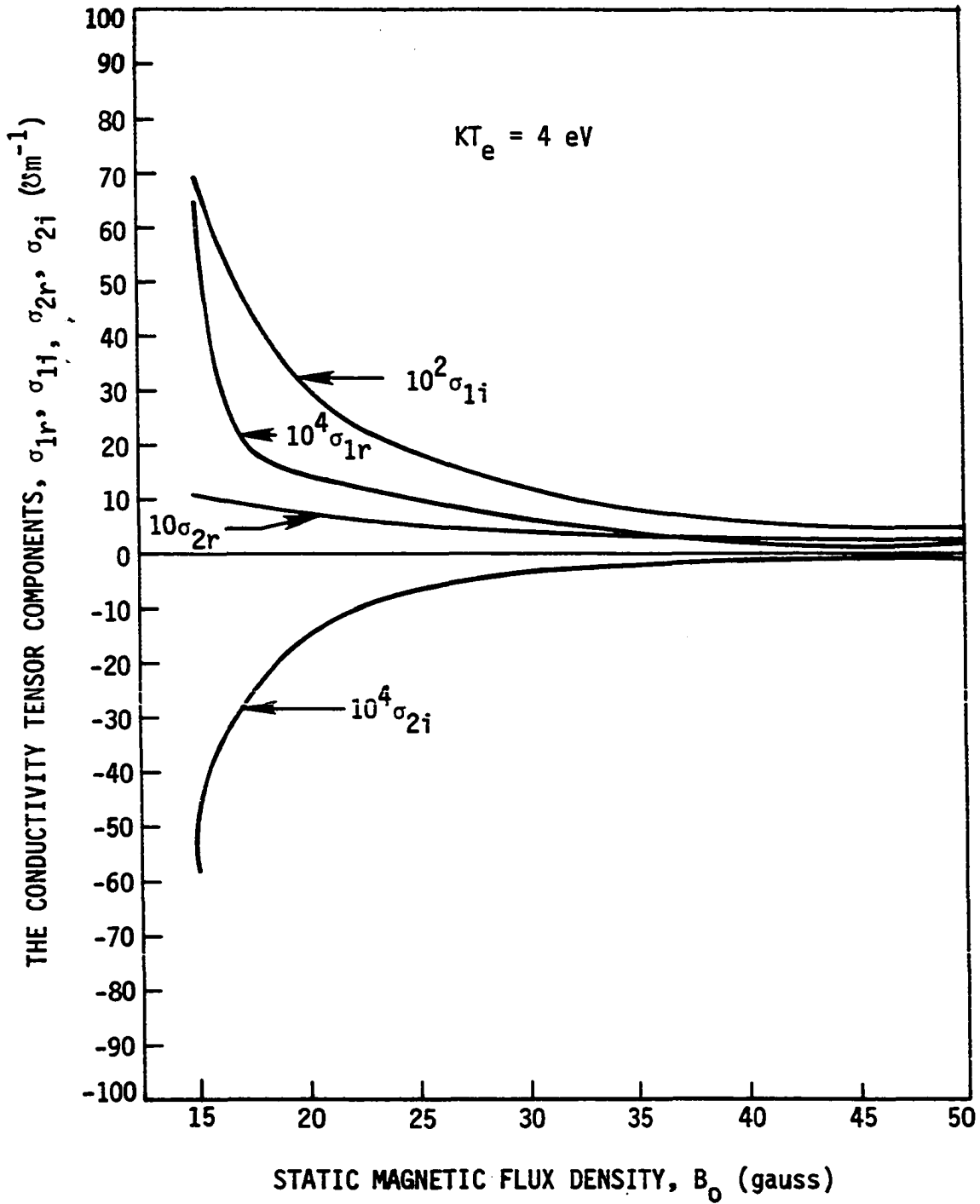


Figure 4.3b. Variation of various components of conductivity tensor with static magnetic flux density, B_0 for case $f = 27$ MHz, $n_e = 6 \times 10^9 \text{ cm}^{-3}$, and $\mu = 8.5 \times 10^4 \text{ m}^2 \text{ v}^{-1} \text{ sec}^{-1}$ (or $KT_e = 8 \text{ eV}$)

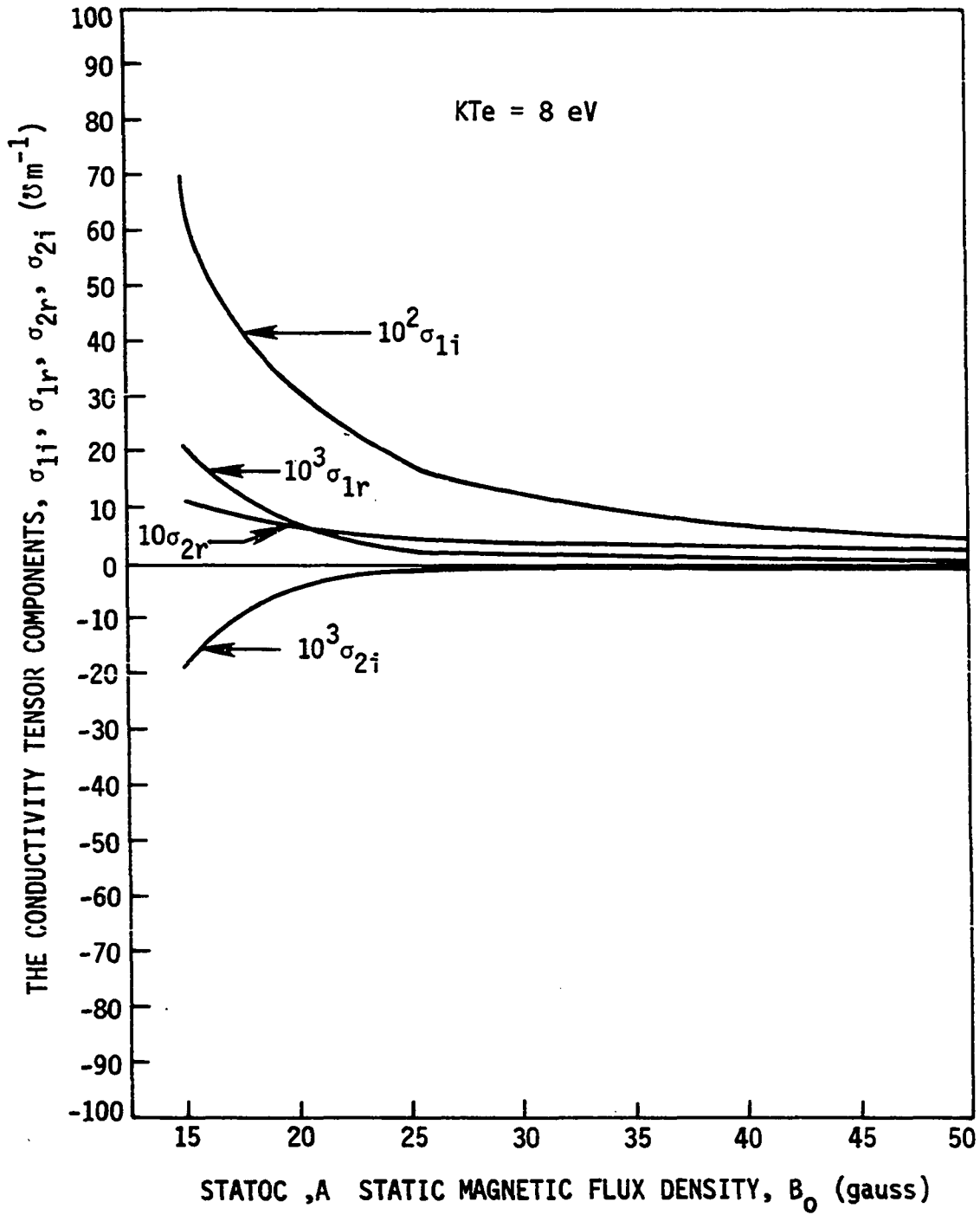


Figure 4.3c. Variation of various components of conductivity tensor with static magnetic flux density, B_0 , for case $f = 27$ MHz, $n_e = 6 \times 10^9 \text{ cm}^{-3}$ and $\mu = 8.5 \times 10^4 \text{ m}^2 \text{ v}^{-1} \text{ sec}^{-1}$ (or $KT_e = 12 \text{ eV}$)

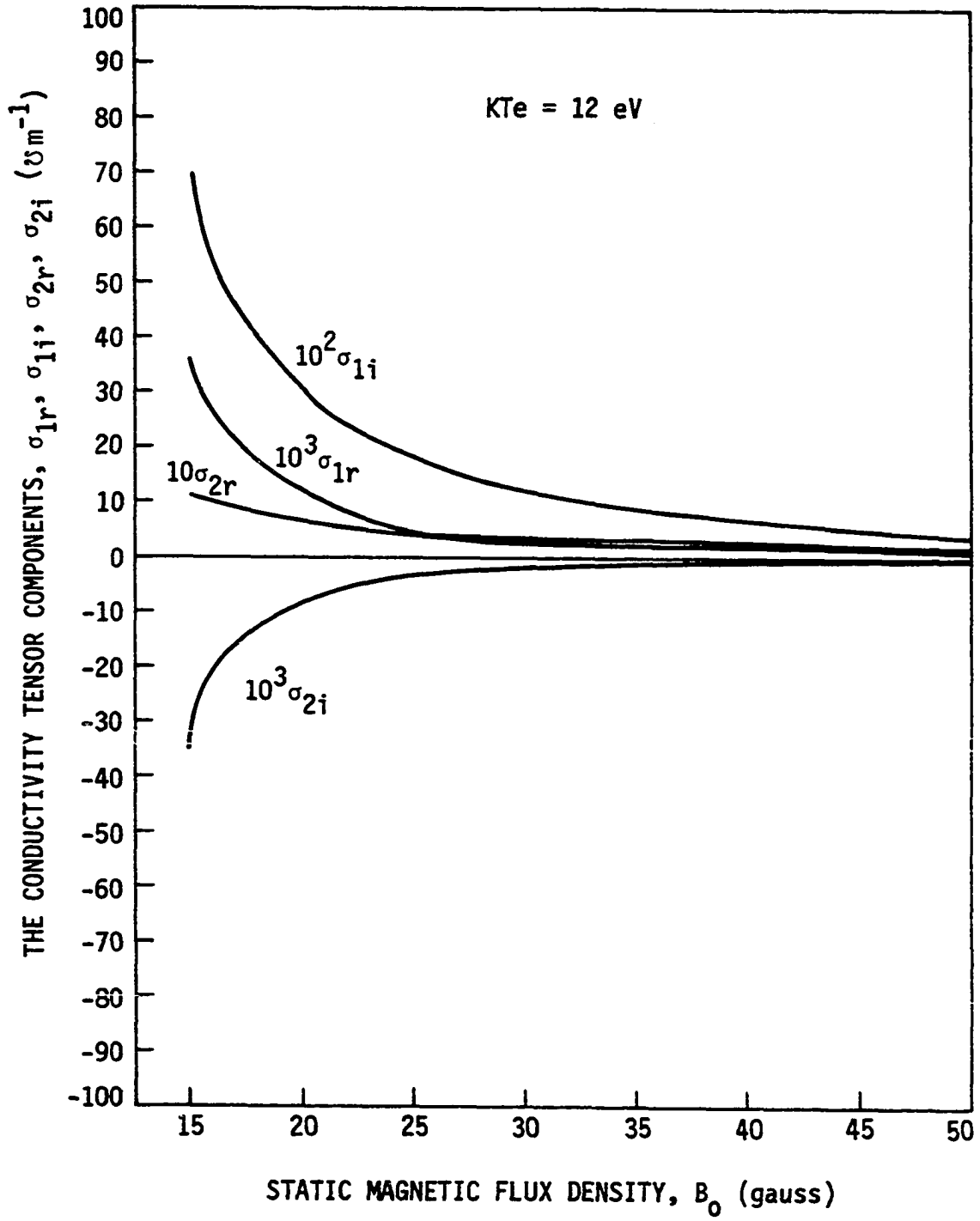


Figure 4.4a. Variation of $\sigma_{1r} = \text{Re}(\hat{\sigma}_1)$ with static magnetic flux density, B_0 for case $n_e = 6 \times 10^9 \text{ cm}^{-3}$ and $f = 27 \text{ MHz}$ with thermal energy as a parameter

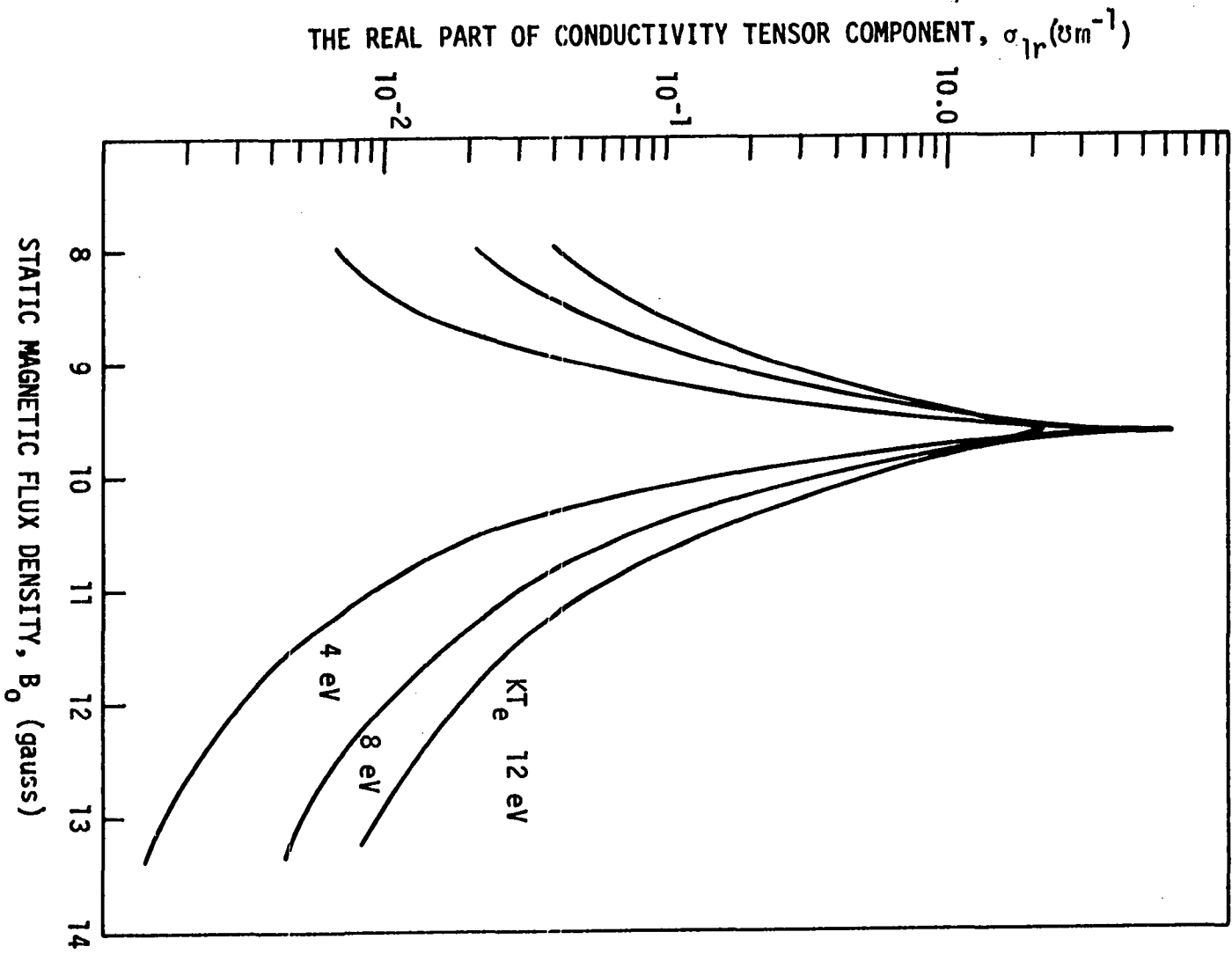


Figure 4.4b. Variation of σ_{1i} , = $\text{Im}(\hat{\sigma}_1)$, with static magnetic flux density, B_0 , for case $n_e = 6 \times 10^9 \text{ cm}^{-3}$ and $f = 27 \text{ MHz}$ with thermal energy as a parameter

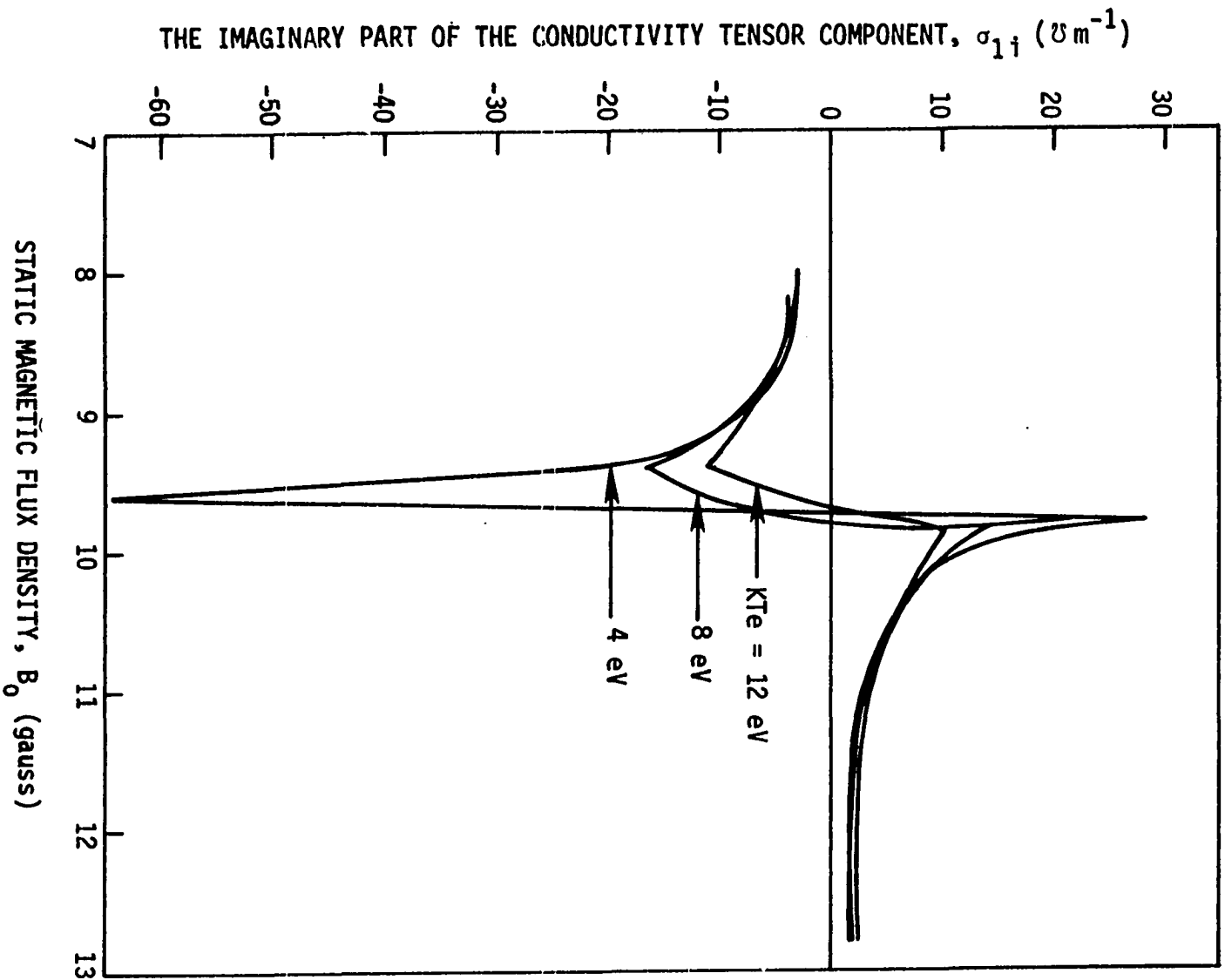


Figure 4.4c. Variation of $\sigma_{2r'} = \text{Re}(\tilde{\sigma}_2)$ with static magnetic flux density B_0 for case $n_e = 6 \times 10^9 \text{ cm}^{-3}$ and $f = 27 \text{ MHz}$ with thermal energy as a parameter

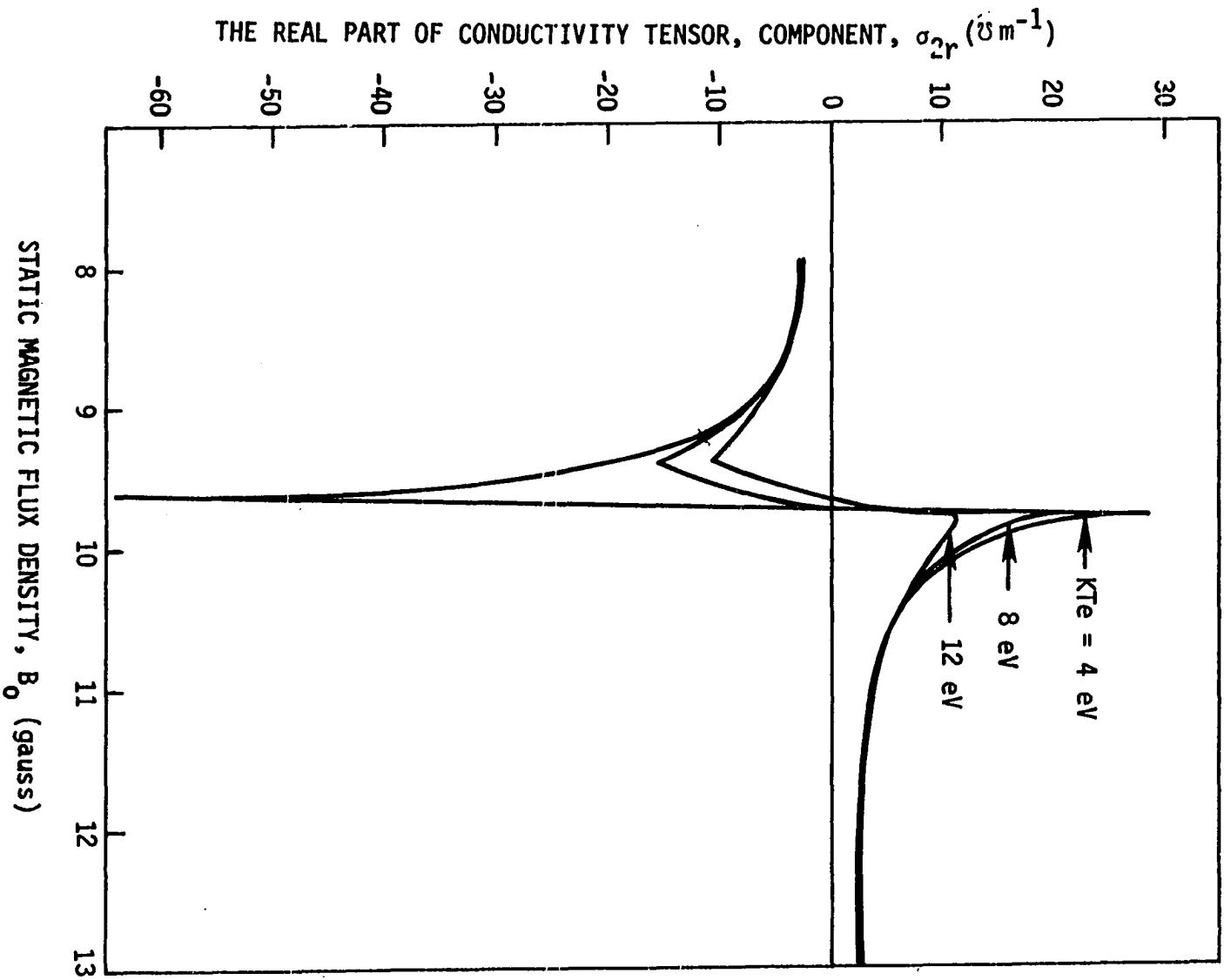
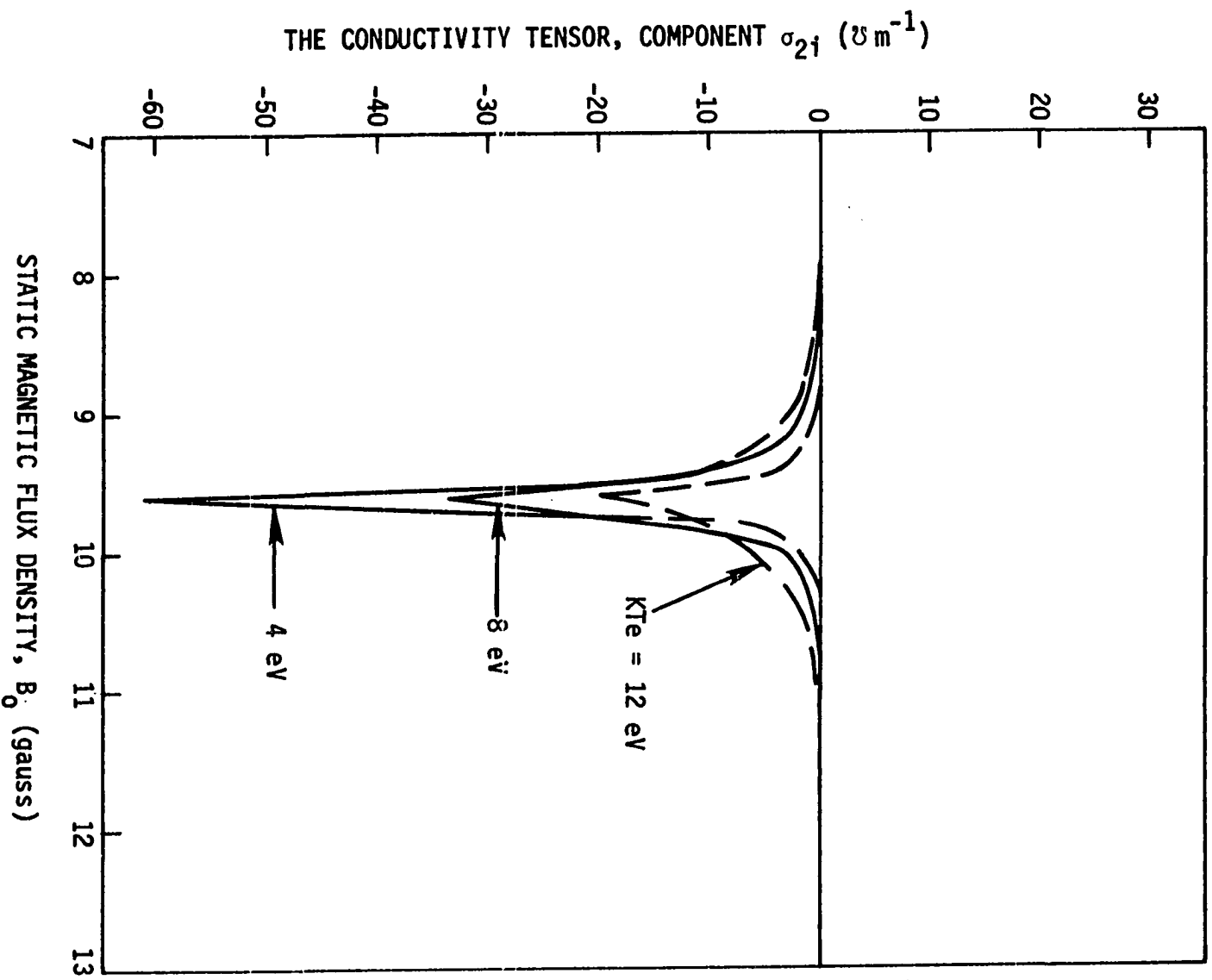


Figure 4.4d. Variation of $\sigma_{2i} = \text{Im}(\hat{\sigma}_2)$ with static magnetic flux density, B_0 for case $n_e = 6 \times 10^9 \text{ cm}^{-3}$ and $f = 27 \text{ MHz}$ with thermal energy as a parameter



B. Circuit Parameter Variations

1. The self-inductance of the rf excitation loop

It is of interest to know how changes in the dimensions of the rf loop will affect the self-inductance of the rf excitation loop $L(a,b,\delta)$, given in Equation 3.73.

For convenience of discussion, $L(a,b,\delta)$ is expressed in the following form in terms of a , δ , and $\alpha = (b/2a)$; (see Figure B.1 for definition of a , b , and δ).

$$L(a,\alpha,\delta) = \frac{a\mu_0}{2\pi} [6(\sqrt{1+\alpha^2} - 1 - \alpha)] - \left(\frac{\delta}{a}\right) 1.763$$

$$+ \log\left(\frac{16a^2}{\delta^2}\right) \left\{ \frac{\sqrt{1+\alpha^2} - 1}{\sqrt{1+\alpha^2} + 1} \right\} \quad (4.2)$$

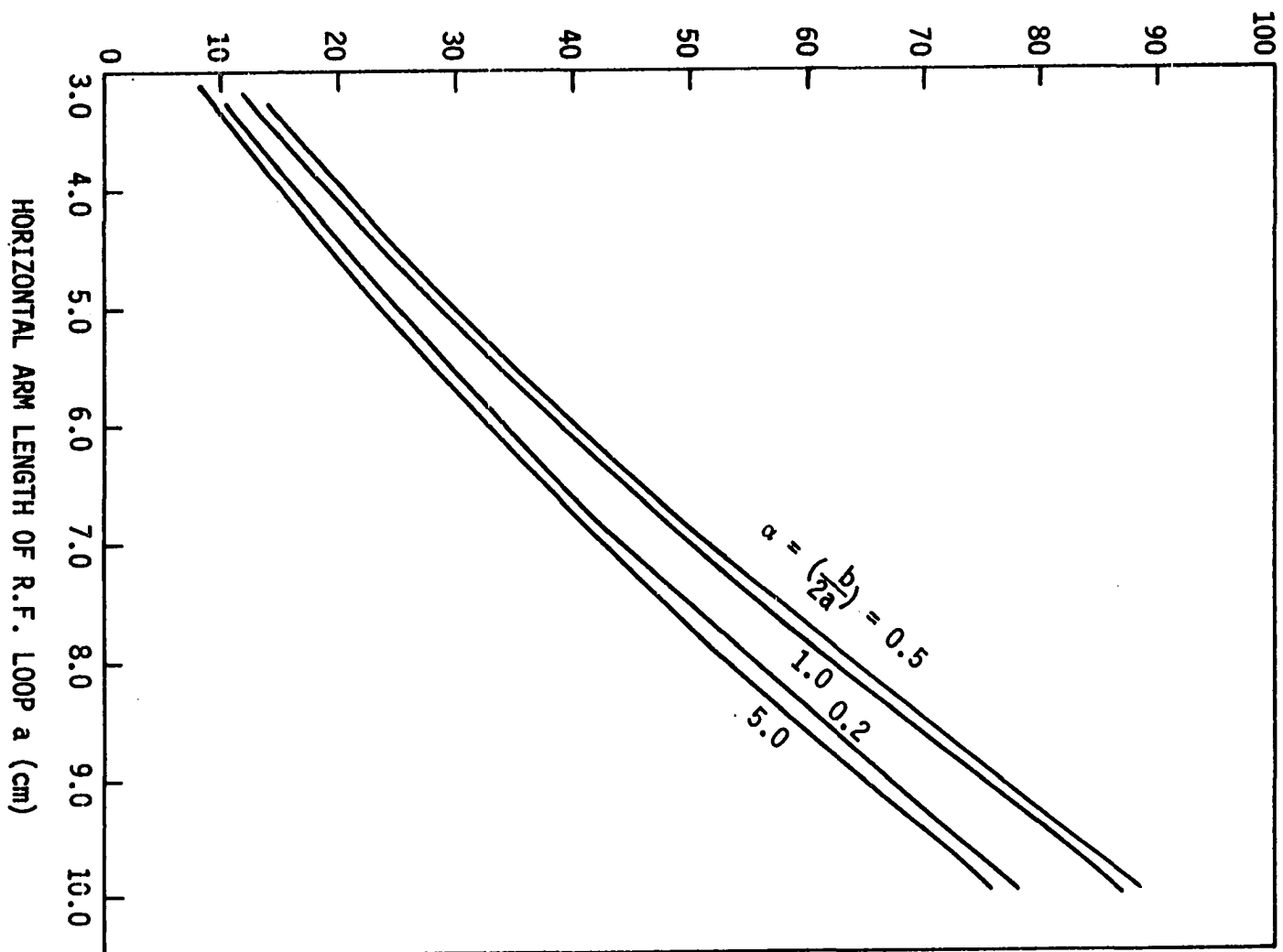
For $\delta = \left(\frac{1}{8}\right)$ in. = 0.32 cm, the variation of $L(a,\alpha,\delta)$ with a , for different values of $\alpha = \left(\frac{b}{2a}\right)$ is illustrated in Figure 4.5.

Note that Figure 4.5 shows that the inductance L increases monotonically with a , for the range of a considered. L also increases with the ratio α until L reaches its maximum value at $\alpha = 0.5$, then decreases with α . This suggests that in order to have a maximum self-inductance dimension a must be equal to dimension b .

For the rf excitation loop used in the present study, $a = 3$ in., $b = 7$ in., and $\delta = 0.125$ in. Substitution of these values and $\mu_0 = \frac{1}{4\pi} \times 10^{-7}$ H/m = 0.567×10^{-7} H/in.

Figure 4.5. Variation of the self-inductance, $L(a, \alpha)$
with the length of horizontal arm of rf loop,
 a , with $\alpha = (\frac{b}{2a})$ as parameter

SELF-INDUCTANCE OF r.f. EXCITATION LOOP, $L(a, \alpha) \times 10^9$ (henrys)



into Equation 4.2 yields $L = 0.567 \times 10^{-7}$ H. Consequently, the rf loop reactance at $f = 27$ MHz is estimated to be

$$X_{\ell} = \omega L = 2\pi fL = 9.62\Omega \quad (4.3)$$

2. The current in the rf excitation loop and equivalent load impedance

As has been discussed previously, the current flow in the rf excitation loop and the equivalent load impedance can be estimated with the aid of experimental measurements of the rf time-averaged power flows \bar{W}^+ and \bar{W}^- and the rf voltage across the transmission line $|\hat{V}_{in}(\ell)|$. This is illustrated below for two cases: case A, where the argon gas has not yet been ionized (no plasma present), and case B, where the gas has been partially ionized (with plasma present). The experimental data are given as

$$\text{Case A): } \bar{W}^+ = 400 \text{ W, } \bar{W}^- = 40 \text{ W, } |\hat{V}_{in}(\ell)| = 190 \text{ V}$$

$$\text{Case B): } \bar{W}^+ = 400 \text{ W, } \bar{W}^- = 35 \text{ W, } |\hat{V}_{in}(\ell)| = 190 \text{ V}$$

which are also shown in Table 3 of Section II. The transmission line used has the characteristic resistance $z_0 = 50\Omega$, and the length is 112 in. $\approx 0.256 \lambda$, where λ is the wave-length of the voltage wave traveling along the transmission line. For an air-line, $\lambda \approx 11.11 \text{ m} = 437.4 \text{ in.}$

Case A:

$$\Gamma_L = \sqrt{\overline{W}^- / \overline{W}^+} = \sqrt{0.1} = 0.3162$$

$$|\hat{V}_0^+| = \sqrt{2\overline{W}^+ z_0} = 200 \text{ V}$$

From Equation 3.87

$$2\Gamma_L \cos \phi = \left| \frac{V_{1n}(\ell)}{V_0^+} \right|^2 - (1 + \Gamma_L^2) = \left(\frac{190}{200} \right)^2 - 1.1 = -0.1975$$

$$\cos \phi = -0.3123 \text{ and } \phi = 1.8884 \text{ rad}$$

Since $\beta\ell = 1.6089$, $\theta = (\phi + 2\beta\ell) = 5.1062 \text{ rad}$. The complex voltage reflection coefficient at the load is

$$\hat{\Gamma}_L = 0.3162 \angle 5.1062 = 0.1213 - j0.2920$$

From Equation 3.88

$$|\hat{I}_L| = \frac{200}{50} \sqrt{1.1 + 0.1975} = 4.56 \text{ A} \quad (4.4)$$

From Equation 3.85a

$$\frac{\hat{z}_L}{z_0} = \frac{1 + \hat{\Gamma}_L}{1 - \hat{\Gamma}_L} = \frac{1.1213 - j0.2920}{0.8787 + j0.2920} = 1.2513 \angle -0.5756$$

Therefore, the equivalent load impedance is given by

$$\hat{z}_L = 52.49 - j34.06 \Omega \quad (4.5)$$

which suggests the presence of the capacitive reactance for the rf loop antenna.

The equivalent load impedance can be written as

$$\tilde{z}_L = R + jX = R_r + j(X_\ell + X_A) \quad (4.6)$$

where R_r denotes the radiation resistance of the loop antenna and $X_\ell = \omega L$ is the loop reactance due to the self-inductance of loop L . For $f = 27$ MHz, $X_\ell = 9.62\Omega$ was given by Equation 4.3. X_A denotes the antenna reactance.

Comparison of Equation 4.5 with Equation 4.6 yields

$$R_r = 52.49 \text{ and } X_A = -43.68\Omega \quad (4.7)$$

Since the capacitive reactance X_A can be represented by an equivalent capacitance C_A as $X_A = -1/(\omega C_A)$, at $f = 27$ MHz, it is estimated that $C_A = 0.135 \times 10^{-9}$ F. Thus the load can be regarded as a circuit with R_r , L , and C_A in series.

Case B:

$$|\Gamma_L| = \sqrt{\bar{W}^- / \bar{W}^+} = \sqrt{0.0875} = 0.2958$$

$$|\tilde{V}_0^+| = 200 \text{ V}$$

$$2\Gamma_L \cos \phi = \left(\frac{190}{200}\right)^2 - 1.0875 = -0.1850$$

$$\cos \phi = -0.3127 \text{ so that } \phi = 1.8888 \text{ rad}$$

which yields

$$\theta = (\phi + 2\beta l) = 5.1066 - \text{rad}$$

From Equation 3.88

$$|\tilde{I}_L|^2 = \frac{200}{50} \sqrt{1.0875 + 0.1850} = 4.51 \text{ A} \quad (4.8)$$

From Equation 3.85a

$$\begin{aligned} \frac{\tilde{z}_L}{z_0} &= \frac{1.1136 - j0.2731}{0.8864 + j0.2731} = 1.2362 \angle -0.5394 \\ &= 1.0607 - j0.6350 \end{aligned}$$

Therefore, the equivalent load impedance is given by

$$\tilde{z}_L = 53.04 - j 31.75 \quad (4.9)$$

Comparison of Equation 4.9 with Equation 4.6 yields

$$R_r = 53.04 \text{ and } X_A = -41.37\Omega \quad (4.10)$$

The equivalent capacitance $C_A = 1/41.37\omega = 0.143 \times 10^9 \text{ F}$.

C. Estimation of Time-Varying Electromagnetic Field Strength and Time-average Power Density

The field strengths of \vec{E}_1 and \vec{H}_1 at an observation point $G(x_0, y_0, z_0)$, which is not too close to any of the boundary structures are estimated in the following manner, for the case when plasma is present.

It is of interest to note that when the observation point G is taken on the plane of symmetry $y_0 = 0$, various

factors in the field expressions are greatly simplified.

From Equation 3.48

$$M_x(x_0, 0, z_0) = 0$$

$$M_y(x_0, 0, z_0) = \frac{-2a}{[x_0^2 + a^2 + z_0^2]^{3/2}} \quad (4.11)$$

$$M_z(x_0, 0, z_0) = 0$$

and from Equation 3.40

$$h_x(x_0, 0, z_0) = \frac{-2a}{P}(z_0 - b) + 2az_0 \left[\frac{1}{M_0} + \frac{1}{F_0} \right]$$

$$h_y(x_0, 0, z_0) = 0$$

$$h_z(x_0, 0, z_0) = 0$$

$$h_z(x_0, 0, z_0) = \frac{-2a}{F_0} \quad (4.12)$$

where

$$P_0 = (x_0^2 + a^2) [x_0^2 + a^2 + (z_0 - b)^2]^{1/2}$$

$$M_0 = (x_0^2 + a^2) [x_0^2 + a^2 + z_0^2]^{1/2}$$

$$F_0 = (x_0^2 + z_0^2) [x_0^2 + a^2 + z_0^2]^{1/2} \quad (4.13)$$

From Equation 3.5

$$e_x = \frac{\sigma_2 M_y}{(\sigma_1^2 + \sigma_2^2)}, \quad e_y = \frac{\sigma_1 M_y}{(\sigma_1^2 + \sigma_2^2)}, \quad e_z = 0 \quad (4.14)$$

For the rf loop used, $a=3$ in. and $b = 7$ in. Suppose that the

observation point G is taken at $x_0 = 1.7$ in., $y_0 = 0$, and $z_0 = 4.5$ in, which corresponds to the location of Langmuir probe tip at d of Tables 1 and 2 in Section II, then by substituting the proper numerical values for x_0 , a , b , and z_0 one obtains: $P_0 = 56.33$ in.³, $M_0 = 60.57$ in.³ and $F_0 = 86.34$ in.³. $h_x = 0.978$ in.⁻¹, $h_y = 0$, $h_z = -0.118$ in.⁻¹.

Consequently, the components of magnetic field intensity are given with the aid of Equation 3.39 and Equation 3.40 as

$$H_x = \frac{I}{4\pi} h_x = \frac{4.51(0.978)}{4\pi(2.54) \times 10^{-2}} = 13.87 \text{ A/m}$$

$$H_y = 0$$

$$H_z = \frac{I}{4\pi} h_z = -1.67 \text{ A/m} \quad (4.15)$$

To estimate the electric field strength, the components of the conductivity tensor must first be calculated. Assuming $n_0 = 6 \times 10^{15} \text{ m}^{-3}$ and $(KT_e) = 8 \text{ eV}$, then from Equations 3.50 and 3.52, $v = 1.727 \times 10^6 \text{ sec}^{-1}$, and $\mu = 1.019 \times 10^5 \text{ m}^2 \text{ v}^{-1} \text{ sec}^{-1}$ so that $\sigma_0 = 106.6 \text{ } \Omega/\text{m}$.

For $B_0 = 19 \text{ G}$, $\mu B_0 = 193.61$, and for $f = 27 \text{ MHz}$, $\omega\tau = 98.23$. Substituting these numerical factors into Equation 3.36 yields

$$\tilde{\sigma}_1 = 0.376 \underline{1.554} \text{ rad} = 0.006 + j 0.376 \text{ } \Omega/\text{m}$$

$$\tilde{\sigma}_2 = 0.741 \underline{-0.007} \text{ rad} = 0.741 - j 0.005 \text{ } \Omega/\text{m}$$

$$\tilde{\sigma}_3 = 1.085 \underline{-1.56} \text{ rad} = 0.011 - j 1.085 \text{ V/m}$$

Since $M_y(x_0, 0, y_0) = -0.704 \times 10^2, 1/m^2$, Equation 3.55 gives

$$e_x = -1.279 \times 10^2, e_y = 0.649 \times 10^2 \underline{-1.581}, e_z = 0 \quad (4.16)$$

so that the electric field strength at the observation point G can be evaluated from Equation 3.24 to give

$$E_x = \frac{I}{4\pi} e_x = \frac{4.51}{4\pi} (-1.279 \times 10^2) = -45.9 \text{ V/m}$$

$$E_y = \frac{I}{4\pi} e_y = 23.29 \underline{-1.581} \text{ rad} = -23.29 - j 0.228 \text{ V/m}$$

$$E_z = 0 \quad (4.17)$$

and the real and imaginary parts of the complex power density \tilde{p} can be respectively evaluated from Equations 3.59a and 3.59b:

$$\begin{aligned} p_r &= \frac{1}{2} [0.006 \{ (45.9)^2 + (23.3)^2 \} - 2(0.005)(45.9)(0.228)] \\ &= 8.00 \text{ W/m}^3 \end{aligned} \quad (4.18)$$

and

$$\begin{aligned} p_i &= -\frac{1}{2} [0.376 \{ (45.9)^2 + (23.3)^2 \} - 2(0.741)(45.9)(0.228)] \\ &= -490.4 \text{ W/m}^3 \end{aligned} \quad (4.19)$$

V. DISCUSSION OF RESULTS

With the aid of experimentally obtained Langmuir probe I-V characteristic curves, as shown in Figure 2.8 for case I and in Figure 2.10 for case III, plasma parameters n_e , T_e , v_e , and α are determined at various probe tip positions. The estimated values of these parameters are shown in Table 1 for case I, where the center-rod cathode is floating and no bias voltage is applied externally. In this case the electron number density n_e , the electron temperature T_e , the electron random mean velocity \bar{v}_e , and the degree of ionization α , are estimated to be $6.5 \times 10^9 \text{ cm}^{-3}$, $8.5 \times 10^4 \text{ }^\circ\text{K}$, $1.81 \times 10^8 \text{ cm/sec}$, and 0.06%, respectively. It is observed that a slight nonuniformity exists in the electron number density and in the electron temperature. The degree of ionization is quite low and the argon gas is very weakly ionized.

It should be noted that the probe technique was introduced by Langmuir and Mott-Smith (6) in 1924. The critical assumption upon which their development is based is that the mean free path of all plasma particles are large with respect to probe dimensions. When this assumption is valid, the probe is screened from the plasma by a space-charge sheath and does not affect the plasma beyond the sheath edge. Plasma parameters determined from

the probe characteristics are those of the undisturbed plasma. When this condition is violated, density gradients are created, thereby causing ions and electrons to diffuse from the plasma to the sheath region and the probe's electric field to penetrate the plasma beyond the sheath edge. The presence of the probe, therefore, causes a perturbation of both plasma density and potential in its vicinity. In this case the plasma parameters determined from the probe characteristic are not the same as those of the undisturbed plasma. This problem has been attacked theoretically by various researchers (86-90).

Since the electron collision frequency ν is estimated to be of the order of 10^6 rad/sec, for the plasma under consideration (see Section IV.A1), the electron mean free path $\bar{\lambda} = (\bar{v}_e/\nu)$ is estimated to be 1.6×10^2 cm for case I, which is certainly larger than that of the probe unit and also much larger than that of the gold probe tip, exposed to the plasma. Consequently, the perturbation due to the presence of probe can be neglected.

The estimated values of the plasma parameters are shown in Table 2 for the case III, where the center-rod cathode is biased externally to maintain -200 V with respect to ground. In this case, the estimated values are $n_e \approx 1.0 \times 10^{11} \text{ cm}^{-3}$, $T_e \approx 2.7 \times 10^5 \text{ }^\circ\text{K}$, $v_e \approx 3.23 \times 10^8$ cm/sec and $\alpha \approx 1.0\%$. In this case also some nonuniformity

is observed in T_e and n_e . It should be noted that in the case III the cathode sputtering process is taking place. Comparison of cases I and III, with the aid of Tables 1 and 2, shows that the electron density n_e , or the degree of ionization, in case III is about one order of magnitude greater than that for the case I. This is reasonable since the presence of a sufficiently strong dc biased electric field causes the neutral argon gas atom to be ionized so that the population of the electron is increased. The electron density n increases rapidly with the biased voltage applied to the cathode. The electron will be accelerated toward the grounded anode, and the probe current will be increased (comparison of Figure 2.8 and Figure 2.10 tends to support this fact). On the other hand, under the cathode sputtering condition, the probe as well as other electrodes in the system will experience sputtering process. Consequently the probe surface area will be changed by the sputtering. It is rather difficult to estimate the change; however, it will have effect on the interpretation of the data obtained. Thus the numerical values shown in Table 2 should be taken as approximate values (order of magnitude estimates) rather than as the exact values. It was noted, for example, that when the dc biased voltage applied to cathode was increased to -500 V, the sputtering of probe took place so quickly that it

was difficult to take reasonable measurements of I-V characteristics.

Measurements of rf power supplied to the sputtering unit were made, and the data are shown in Table 3 for two different physical conditions of argon gas: case A, in which the argon gas contained in the sputtering chamber (bell jar) was not ionized; case B, in which the argon gas was ionized so that plasma was present in the bell jar. The sputtering unit consists of the rf current loop, radiating at a frequency of 27 MHz, in the nonionized gas contained in the bell jar for case A and in the argon plasma environment for case B, and the boundary of the bell jar structure and that of cathode. The data, displayed in Table 3, indicates that the time-averaged power absorbed by the sputtering unit is 360 W for case A and 365 W for case B, which is reasonable since the contribution of absorption by the plasma is included in case B. The rf energy is supplied to the sputtering unit through a section of transmission line by a 27 MHz rf power source, as shown in Figure 3.1.

The sputtering unit can be represented by an electrical load, characterized by an equivalent load impedance, given by Equation 3.70 and having the form $z_L = R_r + j(\omega L + X_A)$, where the radiation resistance R_r , the antenna reactance X_A , and the self-inductance of rf loop L are given by

Equation 3.67, Equation 3.69 and Equation 3.73, respectively.

Using the data obtained from the rf power measurement, as shown in Table 3, and a simple transmission line theory, the estimated values of the rf loop current are obtained.

I_L , R_r , and X_A are given by Equations 4.4 and 4.7 as

$I_L = 4.4$ A, $R_r = 26.2\Omega$, and $X_A = -3.5\Omega$ for case A and by

Equations 4.8 and 4.10 as $I_L = 4.5$ A, $R_r = 27.8\Omega$, and $X_A = -15.9\Omega$ for case B.

It is of interest to note that R_r for case B is larger than that for the case A, which is to be expected since R_r includes the contribution of the power absorbed by the plasma in case B. It should be pointed out that in considering the energy stored in the electric and magnetic fields and the energy absorption, the Maxwell's displacement current density plays an important role in case A, while conduction current density plays a major role in case B, since the argon plasma can be regarded as a conducting fluid (see Equation 3.53). The antenna reactance X_A for both cases appears to be capacitive since it has a negative algebraic sign. Since the total current density in a point inside of bell jar can in general be given by $\vec{J} = \sigma\vec{E} + j\omega\epsilon_0\vec{E}$, where σ is the conductivity of the medium, and since in the case of nonionized gas $\sigma \approx 0$, the complex power density becomes $p = \frac{1}{2}(\vec{E} \cdot \vec{J}^*) = -j \frac{1}{2} \omega\epsilon_0 |\vec{E}|^2$ so that it is easily seen that X_A is negative quantity. On the other

hand, for case B, it is seen from Equation 3.69 that X_A is also negative since q_i given by Equation 3.62b is a positive quantity. This can also be seen from Equation 4.19, where p_i is estimated to be -490 W/m^3 . From Equations 3.65 and 3.68, it is easily seen that X_A must be negative.

It is of interest to note that R_r given by 3.67 and X_A given by Equation 3.69, depend upon the plasma volume τ_0 . In order to evaluate the integrals expressed in Equations 3.67 and 3.69, τ_0 must be specified in detail, i.e., the boundary configuration must be specified in detail. The integrands $S_r(x,y,z)$ and $S_i(x,y,z)$ given by Equation 3.60b and Equation 3.61b, respectively, are not only functions of M_x, M_y, M_z , which are functions of rf loop size, but also the function of the conductivity tensor, which depends on the plasma parameters. The conductivity tensor components, $\sigma_{nr}(n_e, f, B_0, E_0, \nu)$ and $\sigma_{ni}(n_e, f, B_0, E_0, \nu)$ with $n = 1, 2, \text{ or } 3$, given by Equation 3.63, are functions of the externally applied static magnetic field B_0 and electric field E_0 .

In order to have a maximum rf power transfer to the load, $\tilde{z}_L = (R+jX)$, it is necessary to know the value of R and X for a given operating condition so that the impedance looking toward the load and a section of transmission line \tilde{z}_{in} can be found, and the proper value of the source impedance \tilde{z}_g can be chosen to satisfy the condition

$$z_g^2 = z_{in}^{*2}.$$

Note that a change in B_0 will change the values of σ_{nr} and σ_{ni} as well as those of S_r and S_i ; consequently, a change in B_0 leads to changes in R_r and X_A . It is therefore desirable to find out how the conductivity tensor varies with B_0 or E_0 .

The expression for the conductivity tensor σ_{nr} and σ_{ni} is given by Equation 3.36 or Equation 3.63 for the case in which no bias voltage is applied to the cathode. The variation of the real parts and the imaginary parts of various components of the conductivity tensor with electron mobility μ , which is a function of electron temperature T_e , for the case $B_0 = 19$ G, $n_e = 6 \times 10^9$ cm⁻³, with different values of frequency f are illustrated in Figures 4.2a and 4.2b, respectively. It is observed that σ_{1r} and σ_{3r} decrease monotonically with μ for both $f = 1$ MHz and $f = 27$ MHz, while σ_{2r} remains unchanged as μ varies. σ_{1r} increases with f while σ_{2r} and σ_{3r} decrease with f . For $f = 27$ MHz, $\sigma_{1r} < \sigma_{2r} < \sigma_{3r}$, and σ_{3r} is much larger than σ_{1r} , for the range of electron mobility considered. On the other hand, Figure 4.2b shows that σ_{1i} is positive while σ_{2i} and σ_{3i} are negative. σ_{2i} decreases monotonically with μ while it increases with the frequency f . $|\sigma_{1i}|$ and $|\sigma_{3i}|$ vary slightly with μ , while they decrease with the frequency.

With the aid of Equation 3.63, the variations of σ_{nr}

and σ_{ni} (where $n = 1, 2, \text{ or } 3$), with the static magnetic flux density B_0 are investigated for the case where $n_e = 6 \times 10^9 \text{ cm}^{-3}$, $f = 27 \text{ MHz}$, and the electron thermal energy (KT_e) values vary.

It should be noted that σ_{3r} and σ_{3i} depend only upon $a_0 \equiv (\omega\tau)$ but not on $b_0 \equiv (\mu B_0)$; i.e., they do not depend upon B_0 . Moreover, for the range of B_0 such that $b_0^2 > (a_0^2 + 1)$, i.e., $(\mu B_0)^2 > (\omega^2 \tau^2 + 1)$, σ_{1r} , σ_{1i} and σ_{2r} are all positive while σ_{2i} is negative. The variation of σ_{1r} , σ_{1i} , σ_{2r} , and σ_{2i} with B_0 , for the range of $15 < B_0 < 50 \text{ G}$, are illustrated in Figures 4.3a,b and c, for the cases of $KT_e = 4, 8, \text{ and } 12 \text{ eV}$, respectively. It is observed that σ_{1r} , σ_{1i} , σ_{2r} , and $|\sigma_{2i}|$ all decrease monotonically with B_0 and that $\sigma_{1i} \gg \sigma_{1r}$ and $\sigma_{2r} \gg \sigma_{2i}$.

The variation of σ_{1r} , σ_{1i} , σ_{2r} and σ_{2i} with B_0 for the lower range of $8 < B_0 < 13 \text{ G}$ are illustrated in Figures 4.4a,b,c and d, respectively. It is of interest to observe that the algebraic sign of the σ_{1i} and σ_{2r} components change from negative to positive at $B_0 = B_{01}$ and $B_0 = B_{02}$, respectively, where B_{01} is the value of B_0 for which $b_0 = \sqrt{a_0^2 + 1}$ and B_{02} is that for which $b_0 = \sqrt{a_0^2 - 1}$.

Figure 4.4b shows that the plot of σ_{1i} vs B_0 has double peaks; a negative peak in the range $B_0 < B_{01}$ and a positive peak in the range $B_0 > B_{01}$. These peaks are located in the vicinity of $B_0 = B_{01}$, and the values of B_{01} depend

upon $(\omega\tau)$ and μ . The magnitude of these peaks decreases with the electron thermal energy KT_e . Similarly, Figure 4.4c shows that the plot of σ_{2r} vs B_0 has double peaks near $B_0 = B_{02}$. The behavior of σ_{2r} is quite similar to that of σ_{1i} . It is particularly interesting to observe that the plot of σ_{1r} vs B_0 , shown in Figure 4.4a has a positive peak at $B_0 = B_{0r}$ while the plot of σ_{2i} vs B_0 , shown in Figure 4.4d has a negative peak at $B_0 = B_{0r}$. Here B_{0r} denotes the value of B_0 for which $b_0 = a_0$, i.e., $\mu_0 B_0 = \omega\tau$, or $\omega_c = \omega$, which is the cyclotron resonant condition, here $\omega_c = \left(\frac{eB_0}{m}\right)$ denotes the electron cyclotron frequency in radians per second, the value of B_{0r} is equal to $B_{0r} = \left(\frac{m}{e} 2\pi f\right) = 9.65 \text{ G}$ for $f = 27 \text{ MHz}$. The rf power measurement was made at $B_0 = 19 \text{ G}$ which is not near the resonance.

It is well known that at the electron cyclotron resonance the coupling between the rf electromagnetic field and the electron gyrating about the static magnetic field B_0 is strongest. The energy supplied by rf field is absorbed by the gyrating electron.

The peak values of σ_{1r} and σ_{1i} decrease with KT_e and the bandwidth is broader as KT_e increases which is to be expected since KT_e increases with the collision frequency ν (see Figure 4.1).

It should be noted that when $a_0 = b_0$, Equation 3.63

becomes

$$\sigma_{1r} = \frac{2\sigma_0 a_0^2}{(1+4a_0^2)} = -\sigma_{2i}$$

and

$$\sigma_{1i} = \frac{-\sigma_0 a_0}{(1+4a_0^2)} = -\sigma_{2r} \quad (5.1)$$

for the case under consideration, $a_0^2 \gg 1$, so that $\sigma_{1r} \approx \frac{1}{2} \sigma_0 = \frac{1}{2} (e\mu n_e)$, which suggests that the peak value of σ_{1r} decreases with KT_e , since μ decreases with KT_e . On the other hand, Equations 3.60b and 3.61b becomes

$$S_r = \frac{1}{(4\pi)^2} \left\{ \frac{1}{2\sigma_0} (M_x^2 + M_y^2) + \frac{1}{\sigma_0} M_z^2 \right\}$$

and

$$S_i = \frac{1}{(4\pi)^2} \left\{ -\frac{4a_0}{\sigma_0} (M_x^2 + M_y^2) - \frac{a_0}{\sigma_0} M_z^2 \right\} \quad (5.2)$$

Since

$$1/\sigma_0 = \left(\frac{mv}{\mu e^2} \right) \quad \text{and} \quad \frac{a_0}{\sigma_0} = \frac{m\omega}{\mu e^2}$$

Equation 5.2 suggests that S_r is proportional to v and S_i is independent of v , which also implies that the power density absorbed by the plasma is proportional to v . The power thus absorbed may contribute significantly to the heating of plasma.

The possibility of plasma heating by an rf field has attracted a great deal of interest in recent years. For example, the problem of energy transfer to plasma by

magnetic pumping has been considered by Kofoid (91). The magnetic pumping, also called gyrorelaxation, is a collisional process in which a plasma may be heated by a periodic magnetic field superimposed parallel to a steady magnetic field. The addition of a static magnetic field B_0 , for whatever intent, may aid, hinder, or make impossible the coupling of appreciable power into a low pressure plasma, depending upon the relative B_r and B_0 magnitudes. A steady field has been added by many experimenters to limit the radial plasma diffusion. Others have added it with the objective of increasing the depth of field penetration in an attempt to increase the transfer of power.

VI. CONCLUDING REMARKS

In the present study a Langmuir probe suitable for measuring the electron density and temperature of an argon plasma, used in the sputtering system for the purpose of thin-film deposition, has been designed, constructed and tested. It was found that the plasma under consideration is a very weakly ionized gas which has an electron density of about $6.5 \times 10^9 \text{ cm}^{-3}$ and a temperature of about $8.5 \times 10^4 \text{ }^\circ\text{K}$.

Using the measurement data of n_e and T_e , the time averaged power density was estimated as illustrated in Section IV.

To analyze the behavior of the argon plasma under the influence of a static magnetic field B_0 , provided by the Helmholtz coils, the static electric field E_0 , provided by the biased voltage applied to the center-rod cathode, and the time-varying electromagnetic fields excited by 27 MHz rf current flows in the rf loop, the concept of the conductivity tensor for the magneto-plasma was introduced.

The attention has been focused upon the effect of B_0 on the conductivity tensor $\vec{\sigma}(B_0, E_0, f, n_e T_e)$, although the effect of E_0 is also important. The effect of B_0 on the components of the conductivity tensor, σ_{nr} , and σ_{ni} , with $n = 1, 2, \text{ or } 3$ have been examined in detail. The study

shows, for example, that when $\mu B_0 = \omega \tau$ (i.e., at cyclotron resonance), $\sigma_{2r} = -\sigma_{1i}$, $\sigma_{2i} = -\sigma_{1r}$, and σ_{1r} has peak values which suggest that large amounts of power might be absorbed by the plasma. Thus the static magnetic field B_0 can be beneficially utilized in the control of the plasma.

However, it should be pointed out that a rigorous study of the effect of E_0 on $\vec{\sigma}$ requires the solution of Poisson's equation with a proper boundary condition imposed, as outlined in Section III.C6 for the sputtering condition where E_0 is produced by the biased voltage externally applied to the cathode. With a peculiar electrode configuration being considered, this field is highly nonuniform. It will certainly affect the electron velocity as seen in Equation 3.33. This will in turn affect the conductivity tensor. To determine E_0 and the electron number density n_e theoretically it is necessary to solve Poisson's equation numerically, which has not been done in the present study.

A method of analysis was developed; analyze the rf power supplied to the sputtering unit containing the rf excitation loop antenna in the plasma environment; the sputtering unit was represented by an electrical load $\hat{z}_L = R_r + j(\omega L + X_A)$. As has been pointed out previously, in order to evaluate R_r , given by Equation 3.67, and X_A , given by

Equation 3.69, the physical condition of the plasma via the conductivity tensor, as well as the boundary configuration, have to be specified; perhaps one of the weakest points in the simplified theory developed here is Assumption 3 of Section III, in which it is assumed that the excitation fields produced by the rf current on the loop are predominant, so that the boundary effect could be neglected. The reasonableness of this particular assumption can be tested only after the boundary values problem has been solved and studied numerically, which has not been done in this study.

The boundary effect has been neglected for the sake of obtaining mathematical simplicity while retaining the basic physical nature of the system.

It is not difficult to see, however, that the change in B_0 and E_0 will cause \hat{z}_L to change. Once \hat{z}_L is known, the rf power supply to z_L can be determined in principle. Since the most meaningful requirement for the optimum operation of the rf excited dc sputtering system under consideration is the ability to match the output of the rf supply to the load properties of the plasma, knowledge of z_L is essential. It will provide the basis for the design of some form of "matching transformer" to optimize the system.

In view of the fact that many sources of interference for the system occur at the connecting line and around the

sputtering unit, the techniques developed in the present study, illustrated in Section III and Section IV, should provide a convenient and effective way of measuring the electric current flow in the rf loop and the rf power flow. The method of analysis and the techniques of measurement developed in the present study can be beneficially used by those who are working on thin-film deposition by the sputtering technique under consideration.

A. Suggestions for Future Studies

There are several parts of this investigation that have not been adequately completed:

- (1) Evaluation of R_r and X_A by carrying out the spatial integration of S_r and S_i over the plasma volume τ_0 , which involves the proper specification of the limits of the integral expressed in Equation 3.67 and Equation 3.69.
- (2) Solution of Poisson's equation with the proper boundary values assigned to the complicated boundary configuration of the system to determine the E_0 -field and the electron density n_e distribution numerically and therefore to study the effect of E_0 on $\vec{\sigma}$.
- (3) Determination of the boundary effect on the time-varying electromagnetic fields inside the

sputtering chamber.

- (4) Determination of the effect of the center-rod cathode which is made of iron and therefore causes distortion of the magnetic field B_0 , provided by the Helmholtz coils, in the vicinity of the rod and is therefore likely to have an effect on $\vec{\sigma}$.

These questions have not been examined further because a considerable amount of time is required for the solution of these problems on a computer.

VII. REFERENCES

1. Faraday, M. Research in Electricity. London: 1844. Printed by R. and J. E. Taylor, 1949.
2. Plücker, J. "Vefer die Einwirkung des Magneten auf die elektrischen Entladungen in Verdünnten Gasen." Poggend. Ann 103 (1858): 88.
3. Crookes, W. "The Induction Current Through Rarefied Gases Dark Space Round the Negative Pole." Philosophical Transactions of the Royal Society of London 1 (1879): 135.
4. Langmuir, I. "Electric Discharge in Gases at Low Pressures." Zeitschrift fur Physik 46, 3-4 (1927): 271-99.
5. Holt, E. H. and Haskel, R. E. Foundation of Plasma Dynamics, New York: Macmillan Co., 1965, p. 249.
6. Langmuir, I., and Mott-Smith, H. "Studies of Electric Discharge in Gases at Low Pressures." General Electric Review 27 (1924): 449, 538, 616, 762, 811.
7. Langmuir, I., and Mott-Smith, H. M. "Theory of Collection in Gaseous Discharges." Physical Review 28 (1926): 729.
8. Tonks, L., and Langmuir, I. "Oscillation in Ionized Gases." Physical Review 33 (1929): 195.
9. Langmuir, I., and Compton, K. T. "Electrical Discharges in Gases Part II." Review of Modern Physics 3 (1931): 191.
10. Grove, W. R. "On the Electrochemical Polarity of Gases." Philosophical Transactions of the Royal Society of London 142 (1852): 87.
11. Kohlschutter, Von V., and Müller, R. "Über Kathodische Versaubung Vonmetallen in Verdunnten Gases." Zeitschrift Fur Elektrochemie 12 (1906): 365-377.
12. Guntherschulze, A. "Kathode Scattering. I. Electrochemical Scattering." Zeitschrift fur Physik 36 (1926): 566.

13. Millman, J. S., and Seely, S. Electronics. New York: McGraw-Hill Book Co., Inc., 1951. p. 280.
14. Ingersoll, L. S., and de Viney, S. "Non-Magnetic Sputtering Films of Nickel." Physical Review 26 (1925): 86-91.
15. Fruth, H. "Metallized Microphoneic Electrode Members (Metal Such as AU or PT is deposited by Cathodic Sputtering upon Articles such as Acoustic Diaphragms)." American Chemical Society, June 24, 1930.
16. McLean, D. A. "Microminiaturization with Refractory Metals." 1959 WESCON Convention Record, p. 87.
17. Berry, R. W., and Schwartz, N. "Thin Film Components Based on Tantalum." 4th National Convention on Military Electronics, Washington, D.C., June, 1960.
18. Arnold, H. H. "Reliability; A Benefit of Automation." Western Electric Engineer (1962): 4.
19. Balde, J. W., Charschan, S. S., and Dineen, J. J. "Desposition of Tantalum with an Open-ended Vacuum System." Bell System Technical Journal 43 (1964): 127.
20. Wehner, G. K. Advances in Electronics and Electron Physics. New York: Academic Press, 1965.
21. Maissel, L. J. "The Deposition of Thin Films by Cathode Sputtering." In Physics of Thin Films, Bd 3 Herausg, Hass U. Thun. New York: Academic Press, 1966. p. 61.
22. Moore, W. J. "The Ionic Bombardment of Solid Surfaces." American Scientist 48 (1960): 109-33.
23. Froeml, J. "Symposium on Deposition of Thin Films by Sputtering," Rochester, New York, 1966.
24. Lakshmanan, P. K., and Mitchell, J. M. "Some Properties of Sputtered Sulphide Films." Trans. 10th National Vacuum Symposium of the American Vacuum Society, p. 325. (New York: Macmillan, 1963.)

25. Lepselter, M. P. "Beam-lead Technology." Bell System Technical Journal XIV 14 (1966): 233.
26. Anderson, G. S., Mayer, W. N., and Wehner, G. K. "Sputtering of Dielectrics by High-Frequency Fields." Journal of Applied Physics 33, (1962): 2991.
27. Vratny, F. "Deposition of Tantalum and Tantalum Oxide by Superimposed r.f. and d.c. Sputtering." Journal of Electrochemical Society 114 (1967): 505.
28. Vratny, F., and Harrington, D. J. "Tantalum Films Deposited by Asymmetric a.c. Sputtering." Journal of Electrochemical Society 112 (1965): 484.
29. Maissel, L. I., and Schaible, P. N. "Thin Films Deposited by Bias Sputtering." Journal of Applied Physics 36 (1965): 237.
30. Banerji, D., and Grangoli, R. "On Distribution of Space-Potential in High-frequency Glow Discharge." Philosophical Magazine 11 (1931): 410-422.
31. Holland, L. "A Review of Some Vacuum Studies." Vacuum 20 (1970): 175-192.
32. Theurer, H. C., and Hauser, J. J. "Getter Sputtering for the Preparation of Thin Films of Superconducting Elements and Compounds." Journal of Applied Physics 35 (1964): 554.
33. Loeb, L. B. Fundamental Processes of Electrical Discharges in Gases. New York: John Wiley and Sons, Inc., 1939.
34. Loeb, L. B. Basic Processes of Gaseous Electronics. Berkeley, Calif.: University of California Press, 1961.
35. Keywell, F. "Measurement and Collision-radiation Damage Theory of High-vacuum Sputtering." Physical Review 97 (1955): 16.
36. Bradley, R. C. "Sputtering of Alkali Atoms by Inert Gas Ions of Low Energy." Physical Review 93 (1954): 719.

37. Rol, P. K., Fluit, J. M., and Kistemaker, J. "Theoretical Aspects of Cathode Sputtering in Energy Range 5-25 keV." Physica (Netherland) 26 (1960): 1009-11.
38. Wehner, G. K. "Sputtering Yields for Normally Incident Hg⁺-ion Bombardment at Low Ion Energy." Physical Review 108 (1957): 35-45.
39. Moore, W. J. "The Ionic Bombardment of Solid Surfaces." American Scientist 48 (1960): 109-133.
40. Yon, E. T. "Survey of Sputtering Method-advantages and Disadvantages." In First Conference and School of the Elements of Sputtering, p. 6. Orangeburg, New York: Material Research Corporation, 1968.
41. Penning, F. M., and Moubis, J. H. A. The Normal Cathode in Neon, Physica (Netherlands), 15, (1949), 721.
42. Maissel, L. I., and Glang, R. eds. Handbook of Thin Film Technology." New York: McGraw-Hill Book Co. Inc., 1970.
43. Doctor, S. R., Covault, M. L., and Comstock, C. S. "The Sputtering of Amorphous GD-FE and GD-CO Metallic Films for Bubble Memories." Ames, Iowa: Iowa State University, Engineering Research Institute Technical Report, Dec. 1973.
44. Hurwitt, S. "Instrumentation for Sputtering." In First Conference and School on the Elements of Sputtering, p. 82, Orangeburg, New York: Material Research Corporation, 1968.
45. Chaudhari, P., Chomo, J. J. and Gambino, R. J. "Amorphous Metallic Films for Bubble Domain Application." IBM Journal of Research and Development 17, 1973.
46. Chen, F. F. Plasma Diagnostics Techniques. Edited by R. H. Huddleston and S. L. Leonard. New York: Academic Press, 1965. p. 113.
47. Verma, J. S., and Polishuk, P. "Comparison of Electron Density Measurements in A Glow Discharges Using a Langmuir Probe and a Microwave Interferometer." Paper presented at the Meeting of the American Physical Society, Austin, Texas, February 23-25, 1967.

48. Podgorn, I. M. Topics in Plasma Diagnostics. New York: Plenum Press, 1971. p. 10.
49. Golant, V. E. "Microwave Plasma Diagnostic Techniques." Soviet Physics-Technical Physics 5 (1956): 1197.
50. Heald, M. A., and Wharton, C. B. Plasma Diagnostic with Microwaves. New York: John Wiley and Sons, Inc., 1965.
51. Langmuir, I. "Positive Ion Currents in the Positive Column of the Mercury Arc." General Electric Review 26 (1923): 731.
52. Bohm, D., Burhop, E. H. S., and Massey, H. S. W. The Characteristics of Electrical Discharges in Strong Magnetic Fields. Edited by A. Guthrie and R. K. Wakerling. New York: McGraw-Hill Book Co., Inc., 1949. p. 13.
53. Wenzel, F. "Zur Theorie Elektrischer Sonden in Gasentladungen." Zeitschrift fur Angewandte Physik 2 (1950): 59.
54. Medicus, G. "Spherical Probe with Pre-Sheath." In Report on the Twenty-First Conference of Physical Electronics, Cambridge, Mass.: M.I.T., 1962.
55. Allen, J. E., Boyd, R. L. F., and Reynolds, P. "The Collection of Positive Ions by a Probe Immersed in a Plasma." Proceedings of the Physical Society, London 1370 (1957): 297.
56. Glauber, R. J. Time-Dependent Displacement Correlations and Inelastic Scattering by Crystals, Physical Review 98, (1955): 1692.
57. Divydvov, B., and Manoujkaja, L. Z. "Zur Theorie der Elektrischen Sonden in Gasentladunasröhen." Technical Physics of the USSR 3 (1936): 715-728.
58. Bernstein, I. B., Rabinowitz, I. N. "Theory of Electrostatic Probes in a Low-Density Plasma." Physics of Fluids 2 (1959): 112.
59. Ball, D. J. "Plasma Diagnostics and Energy Transport of a d.c. Discharge used for Sputtering." Applied Physics 43, (1972): 3049.

60. Druyvesten, M. J. "Low-voltage ARC." Zeitschrift fur Physik 64 (1930): 781-798.
61. Glasstone, S., and Lovberg, R. H. Controlled Thermo-nuclear Reactions. Princeton, New Jersey: D. Van Nostrand Co., Inc., 1960. p. 197.
62. Cambel, A. B. Plasma Physics and Magnetofluid-Mechanics. New York: McGraw-Hill Book Co., 1963. p. 124.
63. Olsen, H. N. "Partition Function Cut-off and Lowering of the Ionization Potential in Argon Plasma." Physical Review 124 (1961): 1703.
64. Klimontovitch, Y. L. The Statistical Theory of Non-equilibrium Processes in a Plasma. Oxford: Pergamon Press, 1967. p. 70.
65. Holt, E. H., and Haskell, R. E. Foundations of Plasma Dynamics, Chapter 5. New York: Macmillan Co., 1965.
66. Shakarofsky, I. P., Johnston, T. W., and Bachynski, M. P. The Particle Kinetics of Plasmas. Reading, Mass.: Addison-Wesley Publishing Co., 1966. p. 17.
67. Drummond, J. E. Plasma Physics. New York: McGraw-Hill Book Co., Inc., 1961. p. 10.
68. Delcroix, J. L. Plasma Physics. Vol. 2: Weekly Ionized Gases, Chapter 3. New York: John Wiley and Sons Ltd., 1968.
69. Vlasov, A. A. "On the Kinetic Theory of an Assembly of Particles with Collective Interaction." Journal of Physics (Moscow) 9 (1945): 25-40.
70. Gilardini, A. Low Energy Electron Collisions in Gases. New York: John Wiley and Sons, Inc., 1972. p. 48.
71. Rao, K. V. N., Verdegen, J. T., and Goldstein, L. "Interaction of Microwaves in Gaseous Plasmas Immersed in Magnetic Fields." Proceedings of the IRE (1961): 1877-89.
72. Allis, W. R. "Motions of Ions and Electrons." In Handbuch der Physik Vol. 21. Ed. J. Flugge. (Berlin: Springer-Verlag, 1957.

73. Molmud, P. "Langevin Equation and the ac Conductivity of Non-Maxwellian Plasmas." Physical Review 114 (April 1959): 29-32.
74. Shkarofsky, I. R. "Values of Transport Coefficients in a Plasma for any Degree of Ionization on a Maxwellian Distribution." RCA Research Laboratory Report, No. 7-801. Montreal, Canada, 1960.
75. Holt, E. H., and Haskell, R. E. Foundations of Plasma Dynamics. New York: The Macmillan Co., 1965. p. 191.
76. Kraus, J. D. Antennas, Chapter 3.8. New York: McGraw-Hill Book Co., 1950.
77. Hayt, W. H. Engineering Electromagnetics. New York: McGraw-Hill Book Co., 1974. p. 232.
78. Nasser, E. Fundamentals of Gaseous Ionizations and Plasma Electronics. New York: Wiley-Interscience, 1971. p. 65.
79. Golden, D. E., and Bandel, H. W. "Low-Energy e-Ar Total Scattering Cross-Sections; the Ramsauer Townsend Effect." Physical Review 149 (1966): 58.
80. Aberth, W., Sunshine, G., and Berderson, B. "Absolute Measurement of Total Cross-Sections for the Scattering of Low-Energy Electrons by Argon, Nitrogen and Oxygen." In Atomic Collision Processes, p. 53. Edited by M. McDowell. New York: John Wiley and Sons, Inc., 1964, p. 53.
81. Harrington, R. F. Time-Harmonic Electromagnetic Fields. New York: McGraw-Hill Book Co., 1961. pp. 19-23.
82. Kraus, J. D. Antennas. New York: McGraw-Hill Book Co. Inc., 1950. p. 42.
83. Ramo, S., and Whinnery, J. R. Fields and Waves in Modern Radio. New York: John Wiley and Sons, Inc., 1953. p. 32.
84. Lepage, W. R. Analysis of Alternating Current Circuits. New York: McGraw-Hill Book Co., Inc., 1952, p. 252.
85. Ramo, S., and Whinnery, J. R. Fields and Waves in Modern Radio. New York: John Wiley and Sons, Inc., 1953. p. 31.

86. Boyd, R. L. F. The Mechanism of Positive Ion Collection by a Spherical Probe in a Dense Gas. Proceedings of the Physical Society, London, 1951. p. 492.
87. Cohen, I. M. Asymptotic Theory of Spherical Electrostatic Probes in a Slightly Ionized, Collision Dominated Gas. Physics of Fluids 6 (1963): 1492.
88. Waymouth, J. F. Perturbation of a Plasma by a Probe. Physics of Fluids 7 (1964): 1843.
89. Su, C. H., and Lam, S. H. Continuum Theory of Spherical Electrostatic Probes. Physics of Fluids 6 (1963): 1479.
90. Little, R. G., and Waymouth, J. F. "Experimentally Determined Plasma Perturbation by a Probe." Physics of Fluids 9 (1966): 801.
91. Kofoid, M. J. "Plasma Heating with Combined Radio Frequency and Steady Magnetic Fields." Physics of Fluids 13 (1970): 2817.
92. Dwight, H. B. Tables of Integrals and Other Mathematical Data. New York: The Macmillan Co., 1947. p. 45.
93. Dwight, H. B. Tables of Integrals and Other Mathematical Data. New York: The Macmillan Co., 1947. p. 46, 52.

VIII. ACKNOWLEDGMENTS

The author is most grateful to his major professor, Professor H. C. Hsieh, for providing the opportunity for this study and for his technical assistance, helpful discussions, continuous encouragement and guidance.

The author wishes to give special thanks to Professor C. Comstock for the use of the vacuum deposition laboratory and for the assistance rendered by him, Messrs. C. A. Scammon and Mike Covault in operating the equipment. He also expresses appreciation to Messrs. John T. McConnell and Dean Flack of the Electrical Machine Shop, Messrs. Leon Girard and Edwin Mooney of the Mechanical Machine Shop, Messrs. Harold Hall and E. J. Moore of the Glassblowing Shop, and Mr. D. O. Whitmer of the Engineering Research Institute Electronic Shop for their valuable assistance.

The author wishes to give special thanks to Professor D. T. Stephenson for his many discussions and for the suggestions he offered with regards to the laboratory work, and Professor J. L. Knighten for his initial contribution to the computer programming work. Special thanks are also due Messrs. Frank M. Goetz and C. T. Morris of the Bell Telephone Laboratory for their invaluable aid during the course of this work.

The author also wishes to give thanks to three special

professors: S. Doctor, G. Koeber, and R. E. Post for the initial ground work on this study, and for exciting and stimulating conversations, and for their assistance on technical matters. He wishes to further extend his appreciation to Professor Post for serving as a temporary advisor in the absence of Professor Hsieh.

He also expresses appreciation and gives special thanks to Dean D. J. Zaffarano of the Graduate College; Deans D. R. Boylan and P. E. Morgan of the College of Engineering; and Chairman J. O. Kopplin of the Department of Electrical Engineering for their understanding and continuous financial support.

IX. APPENDIX A: DERIVATION OF EQUATION 3.39, THE EXPRESSION
FOR THE TIME-VARYING MAGNETIC FIELD INTENSITY PRODUCED BY
THE CURRENT IN AN rf LOOP

Suppose that the filamentary current sources are distributed, as shown in Figure A.1, in the cartesian coordinate system. Denoting the observation point by $P(x,y,z)$ and the source point by $Q(x',y',z')$ with the aid of the Biot-Savart law, the magnetic field intensity at P due to the u-shaped filamentary current source can be expressed as:

$$\vec{H}(P) = \int_{c_1} \frac{\vec{dl}_1 \times \vec{a}_{R_1}}{4\pi R_1^2} + \int_{c_2} \frac{\vec{dl}_2 \times \vec{a}_{R_2}}{4\pi R_2^2} + \int_{c_3} \frac{\vec{dl}_3 \times \vec{a}_{R_3}}{4\pi R_3^2} \quad (A.1)$$

where the straight paths of integration c_1 and c_3 correspond to the left and right vertical arms of the loop while path c_2 corresponds to the horizontal arm of the loop

$$\vec{dl}_1 = -\vec{a}_z dz', \quad \vec{dl}_2 = \vec{a}_y dy', \quad \vec{dl}_3 = \vec{a}_z dz',$$

$$\vec{a}_{R_1} = \frac{\vec{R}_1}{R_1}, \quad \vec{a}_{R_2} = \frac{\vec{R}_2}{R_2}, \quad \vec{a}_{R_3} = \frac{\vec{R}_3}{R_3}$$

$$\vec{R}_1 = \vec{a}_x x + \vec{a}_y (y+a) + \vec{a}_z (z-z')$$

$$R_1 = |\vec{R}_1| = [x^2 + (y+a)^2 + (z-z')^2]^{1/2}$$

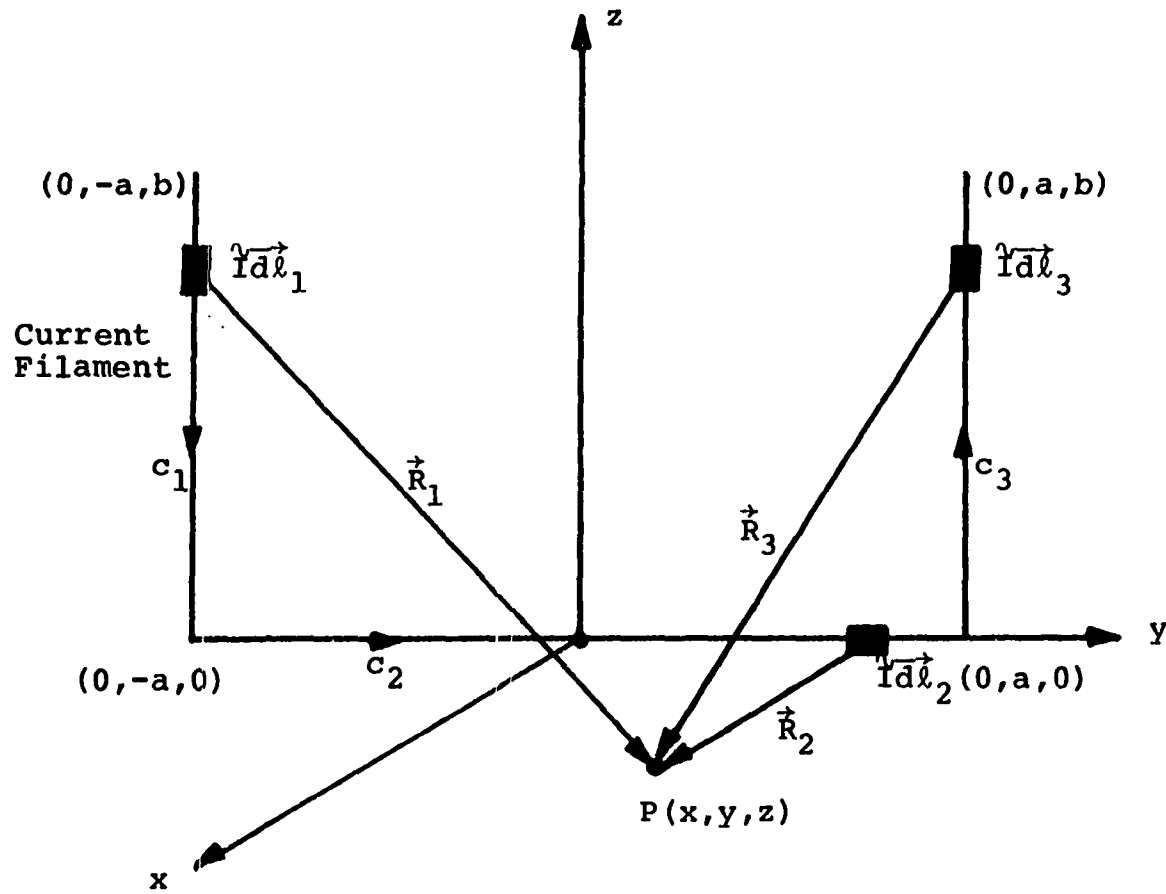


Figure A.1. The coordinate system and the configuration of u-shaped current filament

$$\begin{aligned}\vec{R}_2 &= \vec{a}_x x + \vec{a}_y (y-y') + \vec{a}_z z \\ R_2 &= |\vec{R}_2| = [x^2 + (y-y')^2 + z^2]^{1/2} \\ \vec{R}_3 &= \vec{a}_x x + \vec{a}_y (y-a) + \vec{a}_z (z-z') \\ R_3 &= |\vec{R}_3| = [x^2 + (y-a)^2 + (z-z')^2]^{1/2}\end{aligned}\quad (\text{A.2})$$

in which $(\vec{a}_x, \vec{a}_y, \vec{a}_z)$ are the base unit vectors in the cartesian coordinate system.

Substituting Equation A.2 into Equation A.1 leads to

$$\vec{H}(P) = \vec{H}_1(P) + \vec{H}_2(P) + \vec{H}_3(P) \quad (\text{A.3})$$

where

$$\begin{aligned}H_1(P) &= \frac{I}{4\pi} \int_0^b \frac{\vec{a}_x (y+a) - \vec{a}_y x}{[x^2 + (y+a)^2 + (z-z')^2]^{3/2}} dz' \\ H_2(P) &= \frac{I}{4\pi} \int_{-a}^a \frac{\vec{a}_x z - \vec{a}_z x}{[x^2 + (y-y')^2 + z^2]^{3/2}} dy' \\ H_3(P) &= \frac{I}{4\pi} \int_0^b \frac{\vec{a}_x (a-y) + \vec{a}_y x}{[x^2 + (y-a)^2 + (z-z')^2]^{3/2}} dz'\end{aligned}$$

The integrals in Equation A.3 can be evaluated with the aid of a mathematical integral table (92) to give

$$\vec{H}_1(P) = \frac{I}{4\pi} \left[\frac{\{\vec{a}_x (y+a) - \vec{a}_y x\} (z' - z)}{\{x^2 + (y+a)^2\} \{x^2 + (y+z)^2 + (z' - z)^2\}^{1/2}} \right] \Bigg|_{z'=0}^{z'=b}$$

$$\vec{H}_2(P) = \frac{I}{4\pi} \left[\frac{(\vec{a}_x z - \vec{a}_x) (y' - y)}{(x^2 + z^2)^2 \{x^2 + (y' - y)^2 + z^2\}^{1/2}} \right] \Big|_{y'=-a}^{y'=a}$$

$$\vec{H}_3(P) = \frac{I}{4\pi} \left[\frac{\{\vec{a}_x (a - y) + \vec{a}_y x\} (z' - z)}{\{x^2 + (y - a)^2\} \{x^2 + (y - a)^2 + (z' - z)^2\}^{1/2}} \right] \Big|_{z'=0}^{z'=b}$$

Evaluating the upper and lower limits in the above integrals, substituting them into Equation A.3, and collecting the like components together yields the following expressions for the H_x -, H_y -, and H_z - components;

$$H_x = \frac{I}{4\pi} \left[\left\{ \frac{(y-a)}{P} - \frac{(y+a)}{N} \right\} (z-b) + \left(\frac{1}{M} + \frac{1}{F} \right) (y+a) z - \left(\frac{1}{K} + \frac{1}{V} \right) (y-a) z \right] \quad (A.4)$$

$$H_y = \frac{I}{4\pi} \left[\left(\frac{1}{N} - \frac{1}{P} \right) x(z-b) + \left(\frac{1}{K} - \frac{1}{M} \right) xz \right] \quad (A.5)$$

$$H_z = \frac{I}{4\pi} \left[\frac{(y-a)}{V} - \frac{(y+a)}{F} \right] x \quad (A.6)$$

where

$$N(z, y, z) = \{x^2 + (y+z)^2\} [x^2 + (y+a)^2 + (z-b)^2]^{1/2}$$

$$M(x, y, z) = \{x^2 + (y+a)^2\} [x^2 + (y+a)^2 + z^2]^{1/2}$$

$$P(x, y, z) = \{x^2 + (y-a)^2\} [x^2 + (y-a)^2 + (z-b)^2]^{1/2}$$

$$K(x, y, z) = \{x^2 + (y-a)^2\} [x^2 + (y-a)^2 + z^2]^{1/2}$$

$$V(x, y, z) = (x^2 + z^2) [x^2 + (y-a)^2 + z^2]^{1/2}$$

$$F(x,y,z) = (x^2+z^2)[x^2+(y+a)^2+z^2]^{1/2} \quad (\text{A.7})$$

which is that given in Equation 3.39.

X. APPENDIX B: DERIVATION OF EQUATION 3.73, EXPRESSION FOR THE SELF-INDUCTION OF rf EXCITATION LOOP

The magnetic flux linking the rf loop can be expressed by

$$\phi = \iint_A \vec{B} \cdot d\vec{S} = \int_0^b \int_a^c B_x(0, y, z) dy dz \quad (B.1)$$

where

$$B_x = \mu_0 H_x = \frac{\mu_0 I}{4\pi} h_x(0, y, z) \quad (B.2)$$

The function $h_x(0, y, z)$ is given by Equation 3.40, and

$\mu_0 = \frac{1}{4\pi} \times 10^{-7}$ H/m, is the permeability of free space.

It should be noted that the factor $h_x(0, y, z)$ has the singularities at the points; $x=0$, $z=0$, and $y=\pm a$. In order to avoid the difficulty of integration, the limits of integration are properly modified:

$$\phi = \frac{\mu_0 I}{4\pi} \int_{\delta}^b \int_{-c}^c h_x(0, y, z) dy dz \quad (B.3)$$

where $c = (a - \delta)$, with the distance δ being a small quantity such that $\delta^2 \ll a^2$, and $\delta^2 \ll b^2$.

The self-inductance of the rf excitation loop, L , is expressible as

$$L = \frac{\phi}{I} = \frac{\mu_0}{4\pi} \int_{\delta}^b \int_{-c}^c h_x(0, y, z) dy dz \quad (B.4)$$

The function $h_x(0, y, z)$, given by Equation 3.40 is of the

form

$$h_x(y, z) = \sum_{n=1}^6 h_n(y, z) \quad (\text{B.5})$$

and Equation B.4 can be written as

$$L = \sum_{n=1}^6 L_n \quad (\text{B.6})$$

with

$$L_n = \frac{\mu_0}{4\pi} \int_{\delta}^b \int_{-c}^c h_n(y, z) dy dz \quad (\text{B.7})$$

where

$$L_1 = \frac{\mu_0}{4\pi} \int_{\delta}^b \int_{-c}^c \frac{(z-b)}{(y-a) \sqrt{(y-a)^2 + (z-b)^2}} dy dz$$

$$L_2 = - \frac{\mu_0}{4\pi} \int_{\delta}^b \int_{-c}^c \frac{(z-b)}{(y+a) \sqrt{(y+a)^2 + (z-b)^2}} dy dz$$

$$L_3 = \frac{\mu_0}{4\pi} \int_{\delta}^b \int_{-c}^c \frac{z}{(y+a) \sqrt{(y+a)^2 + z^2}} dy dz$$

$$L_4 = \frac{\mu_0}{4\pi} \int_{\delta}^b \int_{-c}^c \frac{(y+a)}{z \sqrt{(y+a)^2 + z^2}} dy dz$$

$$L_5 = - \frac{\mu_0}{4\pi} \int_{\delta}^b \int_{-c}^c \frac{z}{(y-a) \sqrt{(y-a)^2 + z^2}} dy dz$$

$$L_6 = -\frac{\mu_0}{4\pi} \int_{\delta}^b \int_{-c}^c \frac{(y-a)}{z \sqrt{(y-a)^2 + z^2}} dy dz \quad (\text{B.8})$$

It should be noted that

$$L_2(a, b) = -L_1(-a, b)$$

$$L_5(a, b) = -L_3(-a, b)$$

and

$$L_6(a, b) = -L_4(-a, b) \quad (\text{B.9})$$

moreover, L_1 , L_2 , L_3 , and L_5 are the same type, of the form

$$\Psi(\zeta_1, \zeta_2, \eta_1, \eta_2) \equiv \int_{\eta_1}^{\eta_2} \int_{\zeta_1}^{\zeta_2} \frac{\zeta}{\eta \sqrt{\eta^2 + \zeta^2}} d\zeta d\eta \quad (\text{B.10})$$

and L_4 and L_6 are the same type, of the form

$$\psi(\eta_1, \eta_2, \zeta_1, \zeta_2) \equiv \int_{\zeta_1}^{\zeta_2} \int_{\eta_1}^{\eta_2} \frac{\eta}{\zeta \sqrt{\zeta^2 + \eta^2}} d\eta d\zeta \quad (\text{B.11})$$

The integrals of Equations B.10 and B.11 can be evaluated with the aid of a mathematical integral table

(93) to give

$$\begin{aligned} \Psi(\zeta_1, \zeta_2, \eta_1, \eta_2) = & \left\{ \sqrt{\eta^2 + \zeta_2^2} - \zeta_2 \log \left| \frac{\zeta_2 + \sqrt{\eta^2 + \zeta_2^2}}{\eta} \right| \right. \\ & \left. - \sqrt{\eta^2 + \zeta_1^2} + \zeta_1 \log \left| \frac{\zeta_1 + \sqrt{\eta^2 + \zeta_1^2}}{\eta} \right| \right\} \Bigg|_{\eta = \eta_1}^{\eta = \eta_2} \end{aligned}$$

(B.12)

$$\psi(\eta_1, \eta_2, \zeta_1, \zeta_2) = \left\{ \sqrt{\eta_2^2 + \zeta_2^2} - \eta_2 \log \left| \frac{\eta_2 + \sqrt{\eta_2^2 + \zeta_2^2}}{\zeta_2} \right| \right. \\ \left. - \sqrt{\eta_1^2 + \zeta_1^2} + \eta_1 \log \left| \eta_1 + \sqrt{\eta_1^2 + \zeta_1^2} \right| \right\} \Bigg|_{\zeta_2 = \zeta_1}^{\zeta_2 = \zeta_2}$$

(B.13)

Using the property of Equation B.9, it is necessary only to evaluate L_1 , L_3 , and L_4 . For example, to evaluate L_1 , one sets $\zeta_1 = (\delta - b)$, $\zeta_2 = 0$, $\eta_1 = -(c + a)$, and $\eta_2 = (c - a)$ in Equation B.12, so that

$$\frac{4\pi}{\mu_0} L_1 = \psi[\zeta_1 = (\delta - b), \zeta_2 = 0, \eta_1 = -(c + a), \eta_2 = (c - a)]$$

(B.14)

In a similar manner:

$$\frac{4\pi}{\mu_0} L_3 = \psi[\zeta_1 = \delta, \zeta_2 = b, \eta_1 = (a - c), \eta_2 = (c - a)]$$

(B.15)

and

$$\frac{4\pi}{\mu_0} L_4 = \psi[\eta_1 = (a - c), \eta_2 = (a + c), \zeta_1 = \delta, \zeta_2 = b]$$

After evaluating the factors given by Equations B.14, B.15 and B.16 and performing some algebraic manipulation, the desired inductance L can be expressed in the following form:

$$\begin{aligned}
\frac{4\pi}{\mu_0} L &= 6\sqrt{4a^2+b^2} - 12a - 6b - 2\delta \log(\sqrt{2} + 1) \\
&+ \delta \log \left\{ \frac{\sqrt{2-1}}{\sqrt{2+1}} \right\} \\
&+ 2a \log \left| \left(\frac{16a^2}{\delta^2} \right) \left\{ \frac{\sqrt{4a^2+b^2}-2a}{\sqrt{4a^2+b^2}+2a} \right\} \right|
\end{aligned} \tag{B.17}$$

given in Equation 3.73.

XI. APPENDIX C: DERIVATION OF EQUATIONS 3.60, 3.61,
3.62 AND 3.63, THE EXPRESSIONS FOR THE REAL
AND IMAGINARY PARTS OF THE COMPLEX POWER DENSITY

The substitution of Equation 3.54 into Equation
3.59a,b yields

$$p_r = \frac{|I|^2}{(4\pi)^2} [\sigma_{1r}(|e_x|^2 + |e_y|^2) + 2\sigma_{2i} \text{Im} \cdot (e_x^* e_y) + \sigma_{3r} |e_z|^2] \quad (\text{C.1})$$

and

$$p_i = \frac{|I|^2}{(4\pi)^2} [\sigma_{1i}(|e_x|^2 + |e_y|^2) - 2\sigma_{2r} \text{Im} \cdot (e_x^* e_y) + \sigma_{3i} |e_z|^2] \quad (\text{C.2})$$

since Equation 3.55 can be written as

$$\begin{aligned} e_x &= \frac{\sigma_1}{\Delta} M_x + \frac{\sigma_2}{\Delta} M_y \\ e_y &= -\frac{\sigma_2}{\Delta} M_x + \frac{\sigma_1}{\Delta} M_y \\ e_z &= \frac{1}{\sigma_3} M_z \end{aligned} \quad (\text{C.3})$$

where

$$\Delta \equiv (\alpha_1^2 + \sigma_2^2)$$

and

$$2j\text{Im}\cdot(e_x^*e_y) = (e_x^*e_y - e_x e_y^*) = \frac{(\sigma_1\sigma_2^* - \sigma_1^*\sigma_2)}{|\Delta|^2} (M_x^2 + M_y^2) \quad (\text{C.4})$$

$$|e_x|^2 + |e_y|^2 = (e_x e_x^* + e_y e_y^*) = \frac{(|\sigma_1|^2 + |\sigma_2|^2)}{|\Delta|^2} (M_x^2 + M_y^2) \quad (\text{C.5})$$

The substitution of Equations C.4, C.5 into Equation C.1 and Equation C.2 yields

$$P_r = \frac{1}{2} \frac{|I|^2}{(4\pi)^2} \left[\left\{ \frac{\sigma_{1r}(|\sigma_1|^2 + |\sigma_2|^2) + 2\sigma_{2i}\text{Im}\cdot(\sigma_1\sigma_2^*)}{|\Delta|^2} \right\} (M_x^2 + M_y^2) + \frac{\sigma_{3r}}{|\sigma_3|^2} M_z^2 \right] \quad (\text{C.6})$$

$$P_i = \frac{1}{2} \frac{|I|^2}{(4\pi)^2} \left[\left\{ \frac{\sigma_{1i}(|\sigma_1|^2 + |\sigma_2|^2) - 2\sigma_{2r}\text{Im}\cdot(\sigma_1\sigma_2^*)}{|\Delta|^2} \right\} (M_x^2 + M_y^2) + \frac{\sigma_{3i}}{|\sigma_3|^2} M_z^2 \right] \quad (\text{C.7})$$

$$\text{since } \sigma_1\sigma_2^* = (\sigma_{1r} + j\sigma_{1i})(\sigma_{2r} - j\sigma_{2i})$$

$$\text{Im}\cdot(\sigma_1\sigma_2^*) = (\sigma_{1i}\sigma_{2r} - \sigma_{1r}\sigma_{2i}) \quad (\text{C.8})$$

$$|\sigma_1|^2 = (\sigma_{1r}^2 + \sigma_{1i}^2)$$

$$\begin{aligned}
|\sigma_2|^2 &= (\sigma_{2r}^2 + \sigma_{2i}^2) \\
|\Delta|^2 &= |\sigma_1^2 + \sigma_2^2|^2 = \{(\sigma_{1r}^2 + \sigma_{2r}^2) - (\sigma_{1i}^2 + \sigma_{2i}^2)\}^2 \\
&\quad + 4(\sigma_{1r}\sigma_{1i} + \sigma_{2r}\sigma_{2i})^2 \tag{C.9}
\end{aligned}$$

By defining the factors q_r and q_i as

$$q_r = \sigma_{1r}(|\sigma_1|^2 + |\sigma_2|^2) + 2\sigma_{2i}\text{Im}(\sigma_1\sigma_2^*) \tag{C.10}$$

$$q_i = \sigma_{1i}(|\sigma_1|^2 + |\sigma_2|^2) - 2\sigma_{2r}\text{Im}(\sigma_1\sigma_2^*) \tag{C.11}$$

Equations C.6 and C.7 can be expressed in the forms of Equations 3.60 and 3.61.

The complex component of the conductivity tensor, $\tilde{\sigma}_1$, $\tilde{\sigma}_2$, and $\tilde{\sigma}_3$ given by Equation 3.36 can be written in rectangular form as

$$\tilde{\sigma}_1 = \sigma_{1r} + j\sigma_{1i}, \quad \tilde{\sigma}_2 = \sigma_{2r} + j\sigma_{2i}, \quad \tilde{\sigma}_3 = \sigma_{3r} + j\sigma_{3i}, \tag{C.12}$$

Letting $a_0 = (\omega\tau)$, and $b_0 = (\mu B_0)$, Equation 3.36 can be rearranged as:

$$\tilde{\sigma}_1 = \frac{\sigma_0(1 + ja_0)}{(b_0^2 - a_0^2 + 1) + j2a_0}$$

$$\tilde{\sigma}_2 = \frac{\sigma_0 b_0}{(b_0^2 - a_0^2) + j2a_0}$$

$$\sigma_3^2 = \frac{\sigma_0}{(1+ja_0)} \quad (C.13)$$

which can be written as

$$\sigma_1^2 = \frac{\sigma_0 [(b_0^2 + a_0^2 + 1) + ja_0 (b_0^2 - a_0^2 - 1)]}{(b_0^2 - a_0^2 + 1)^2 + 4a_0^2}$$

$$\sigma_2^2 = \frac{\sigma_0 b_0 [(b_0^2 - a_0^2 + 1) - j2a_0]}{(b_0^2 - a_0^2 + 1)^2 + 4a_0^2}$$

$$\sigma_3^2 = \frac{\sigma_0 (1 - ja_0)}{(1 + a_0^2)} \quad (C.14)$$

The comparison of Equation C.12 with Equation C.14 yields Equation 3.63.